THE UNIVERSITY OF MANITOBA

# SPIN CORRELATION PARAMETER AND ANALYZING POWER IN n-p ELASTIC SCATTERING AT INTERMEDIATE ENERGIES.

by

© DINABANDHU BANDYOPADHYAY

A THESIS

SUBMITTED TO THE FACULTY OF GRADUATE STUDIES AND RESEARCH IN PARTIAL FULFILLMENT OF THE REQUIREMENTS FOR THE DEGREE OF DOCTOR OF PHILOSOPHY

IN

NUCLEAR PHYSICS

DEPARTMENT OF PHYSICS

WINNIPEG, MANITOBA

FALL, 1988

ISBN 0-315-48025-4

# SPIN CORRELATION PARAMETER AND ANALYZING POWER IN n-p ELASTIC SCATTERING AT INTERMEDIATE ENERGIES

BY

DINABANDHU BANDYOPADHYAY

A thesis submitted to the Faculty of Graduate Studies of the University of Manitoba in partial fulfillment of the requirements of the degree of

DOCTOR OF PHILOSOPHY

## Dedication

To my parents who always encouraged me even without knowing what I was doing.

THE UNIVERSITY OF MANITOBA

RELEASE FORM

NAME OF AUTHOR: Dinabandhu Bandyopadhyay

TITLE OF THESIS: Spin Correlation Parameter and Analyzing Power in n-p Elastic Scattering at Intermediate Energies.

DEGREE: DOCTOR OF PHILOSOPHY

YEAR THIS DEGREE GRANTED: 1988



(Signed) .....

PERMANENT ADDRESS:

DATED: .....

## Abstract

In order to remove the existing ambiguities in the I=0 phases, as well as to reduce the $\chi^2$ per datum for some single energy phase shift solutions, the spin correlation parameter, $A_{yy}$, and the analyzing power, $A_y$, have been measured over an angular range of $50^0 - 150^0 (c.m.)$ at three energies, 220, 325 and 425 MeV to an absolute accuracy of $\pm 0.03$. Polarized neutrons produced in a liquid deuterium target were scattered from a frozen spin type polarized proton target. Scattered neutrons and recoil protons were detected in two sets of symmetrically placed detector systems. The data have a profound effect on different phase parameters particularly the $^1P_1$, $^3D_2$ and $\epsilon_1$ phases which in some cases change by almost a degree. The data also help to discriminate between two nucleon- nucleon potential models, the Paris and Bonn potentials.

## Acknowledgements

I am particularly grateful to my supervisor Prof. W. T. H. van Oers for the guidance and support that he extended to me throughout my career as a graduate student. His knowledge on the subjects and thoroughness in experimental details helped me learning a lot during my student years. Special thanks to Dr. Charles A. Davis who organized running this complex experiment and helped me with the brief but precise answers to all my silly questions. I thank Dr. L. G. Greeniaus of the University of Alberta for his valuable suggestions and expertise on the analysis and also for reading the manuscript. During the past years, my association with humorous Des Ramsay, witty and funny Shelley Page, systematic error boss Jim Birchall and Norman, the mountaineer, Davison was extremely educational and entertaining. On those Fridays, at the Weak Flavor lunch meeting, despite the risk of getting broke financially, I enjoyed the casual atmosphere, friendly attitude and wide range of discussions which made valuable contributions to my present understanding of nuclear physics.

I also thank my college teacher Dr. K. C. Das who first brought me into physics and taught me the basic principles with great care and affection. His contribution in my upbringing as a physicist is enormous.

I am deeply indebted to my fiancee, Lopamudra Dutta, for her love, continous support and encouragement which helped me spending these years away from her. Thanks also go to the fellow graduate students, Kostas, Chris, Anurag, John, Karo, Dave and others who not only helped me adjusting the 'culture shock' after my first arrival in Canada but also taught me the first basic principles of almost everything, from cars to bars.

# Contents

# List of Tables

# List of Figures

# Chapter 1

# An Overview

In 1932, three months after the publication of Chadwick's paper on the discovery of the neutron, Heisenberg proposed that the neutron and proton, because of their various similarities, could be considered as two different states of the same particle - the nucleon. In doing this he extended the idea of Pauli's spin matrices to label the two states of the nucleon. In 1937, Wigner gave the name isotopic spin or simply the isospin to this new quantum number which distinguishes a neutron from a proton. Around 1935, first Guggenheim and later Young suggested that the n-n, p-p and n-p forces are all alike. Gradually it became clear that the nucleon-nucleon (NN) interaction had to be studied extensively in order to unfold the mysteries of nuclear forces and the binding mechanism of nuclei. The basic knowledge of the nucleon-nucleon force was obtained through studying the binding energy of nuclei. The rapid rise of the binding energy per nucleon with the atomic number for nuclei with few nucleons implies that the nucleon-nucleon (NN) force is short range. For very large values of A, the binding energy per nucleon becomes constant indicating that the nucleon-nucleon force is saturated and is consistent with the repulsive nature of the short range part

of the interaction.

The first step in understanding the nuclear force was taken by Yukawa when in 1935 he proposed a one meson exchange theory according to which the nucleons interact with each other by exchanging virtual mesons ($\pi$). This early theory was quite successful in explaining the long range part of the NN-interaction. With the advent of particle accelerators many new mesons were discovered and were readily incorporated into the theory making it both more successful and more complicated at the same time. The theory at present is able to give quite a satisfactory account of the NN-interaction at distances where the exchange of one or two pions is possible, i.e. for $r \geq 0.8\, fm$. Because of the repulsive nature of the nucleon-nucleon interaction due to the exchange of $\rho$ and $\omega$ mesons the nucleons most probably do not come closer than distances of this order. The conventional meson theory fails for $r \leq 0.8\, fm$. At these distances the quark models become very important [1,2].

In the quark picture the nucleons are perceived as composed of three fractionally charged 'quarks', e.g.,the protons are made up of two up (u) and one down (d) quarks whereas the neutrons are formed by one up and two down quarks. Short range repulsion of the NN-interaction is a direct consequence of quark confinement in the nucleons. However, the long range part is still dominated by $\pi$ and $2\pi$ exchanges. One interesting approach is to combine the meson theory and quark model together, i.e. for $r \leq 0.8\, fm$ one uses a quark picture and for $r > 0.8\, fm$ the meson exchange theory.

In the 1970s when the various meson factories (LAMPF, SIN, TRIUMF) came into operation a copious amount of experimental data became available on two nucleon scattering observables such as cross-sections, polarizations, analyzing powers. Since then a great deal of effort has been spent on phase

shift parametrizations and the development of phenomenological potentials to fit the measured data. Besides the pion-nucleon coupling constants, $g_\pi$ and the $\pi - \pi$ isospin 0 S-wave scattering length $a_s^0$, the essential ingredients for different phenomenological potentials are a certain number of free parameters. It has now become apparent that in order to unravel the spin dependence of the NN-interaction various spin observables must be measured to a very high degree of accuracy.

The experiment described in this thesis was the measurement of the spin correlation parameter, $A_{yy}$, in n-p elastic scattering over an angular range of $50^0 - 150^0$ (c.m.) at three energies, 220 MeV, 325 MeV and 425 MeV. In addition, the analyzing powers were obtained over the same angle and energy range.

In section 1.2 of this chapter a consistent NN scattering formalism will be developed. Phase shift parametrizations of the NN scattering matrix will be reviewed in section 1.3. The last section (1.4) will deal with a short discussion of two phenomenological potentials (PARIS and BONN).

## 1.1 Motivation

The discussion in this and subsequent sections will mainly focus on n-p scattering. It is also assumed that isospin is a good quantum number, and thus the I=1 part of the n-p scattering can be supplemented by the p-p scattering data. As mentioned in the introduction, phase shift analyses (PSA) have become a very successful tool for the determination of the nucleon-nucleon amplitudes in the low and intermediate energy regions. The p-p phase shifts are very well known up to $\sim 1$ GeV, however, the same cannot be said for the isospin zero part of the n-p phases. Phase shifts cannot

Table 1.1: Summary of Phase Shift Analyses

| Energy interval MeV | p-p | | | n-p | | | Ref |
|---|---|---|---|---|---|---|---|
| | No. of points | $\chi^2$ | $\chi^2$/point | No. of points | $\chi^2$ | $\chi^2$/point | |
| 10-220 | 1164 | 1440 | 1.30 | 2312 | 3691 | 1.65 | |
| 130-460 | 1751 | 2203 | 1.31 | 2163 | 3253 | 1.56 | Saclay |
| 380-610 (pp) | 2393 | 2895 | 1.25 | | | | Geneva |
| 360-610 (np) | | | | 1877 | 2660 | 1.46 | [3] |
| 530-830 (pp) | 3901 | 4641 | 1.22 | | | | |
| 520-800 (np) | | | | 2235 | 3126 | 1.43 | |
| 179-225 | 81 | 82 | 0.99 | 276 | 495 | 1.79 | |
| 285-350 | 409 | 452 | 1.11 | 510 | 697 | 1.37 | |
| 375-425 | 342 | 363 | 1.06 | 413 | 706 | 1.71 | |
| 425-475 | 326 | 398 | 1.22 | 338 | 446 | 1.32 | Arndt |
| 450-550 | 978 | 1354 | 1.38 | 618 | 831 | 1.35 | [4] |
| 510-590 | 877 | 1137 | 1.30 | 425 | 471 | 1.11 | |
| 550-650 | 1161 | 1439 | 1.24 | 638 | 790 | 1.24 | |
| 600-700 | 794 | 1024 | 1.30 | 644 | 810 | 1.26 | |
| 665-735 | 518 | 602 | 1.16 | 349 | 386 | 1.11 | |
| 705-795 | 575 | 805 | 1.40 | 380 | 573 | 1.51 | |
| 765-835 | 938 | 1670 | 1.78 | 444 | 826 | 1.86 | |

be uniquely defined with an incomplete data set or with data having large systematic errors. The fact that the n-p data base still has some problems, either in the form of large systematic errors or because of grossly underestimated errors, is reflected in Table -1.1 where the $\chi^2$ per data point for some single energy solutions from the two most recent phase shift analyses [3,4] are summarized. Note that for most energy regions, the n-p $\chi^2$ per data point is significantly larger than the corresponding value for the p-p data. These two analyses, one by the Saclay-Geneva group [3] and the second one by Arndt et al. [4], show striking disagreement in their predictions for the I=0 phases. This disagreement is evident from fig 1.1 and is mainly because of different normalizations and specific selection of data sets. The

large discontinuities in overlapping energy regions of the Saclay phase shift solutions indicate that there are not enough spin dependent data available for a smooth energy behaviour of the fixed energy solutions. At present the amount of data is too sparse to construct the complete n-p scattering amplitudes. Note that 80% of the total available n-p data are spin independent data, 14% are polarizations and analyzing powers and only 6% are two or three index parameter data [5] e.g. $A_{yy}$, $D_t$ etc. The general feeling is that more spin dependent n-p scattering data are needed.

The difficulty in obtaining a consistent phase shift analysis is not always due to the scarcity of data. Often the inconsistencies among different data sets of the same measured quantity pose a much greater problem. As an example, fig 1.2 shows the 425 MeV analyzing powers measured at LAMPF [6] and by the BASQUE group at TRIUMF [7]. Both measurements are in reasonable agreement at backward and forward angles. However, in the intermediate angular range, they not only differ in magnitude (at some points by $\sim 30$ %) , but the shapes are also different. This difference in shape cannot be removed by normalization, so there must be something wrong with either one or both of the above measurements. In the present experiment the analyzing powers at 220, 325 and 425 MeV are also extracted and thus help resolve the above problem.

It has long been known that the tensor component of the NN force plays an important role in explaining the binding energy of the three nucleon system [8] and the saturation of nuclear matter [9]. A direct manifestation of a tensor force is the existence of the deuteron quadrupole moment. The ${}^3D_1 - {}^3S_1$ mixing parameter, $\epsilon_1$, is a measure of the tensor force. For example, in the effective range approximation the mixing parameter at low incident

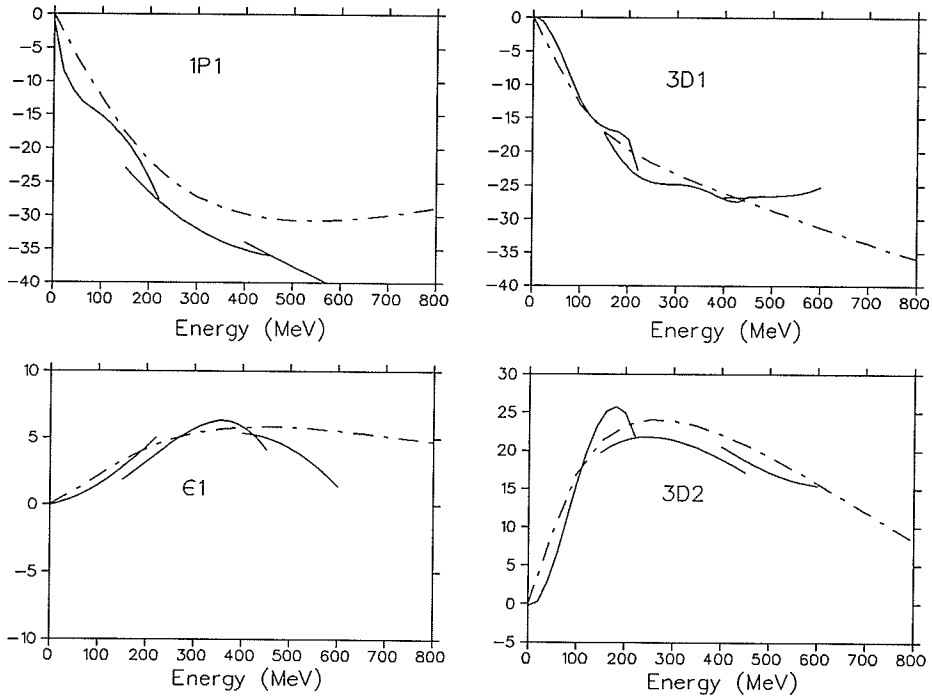


Figure 1.1: Predicted values of phases. Dash-dot curve corresponds to Arndt's solution [4] and solid lines are the Saclay-Geneva solutions [3].

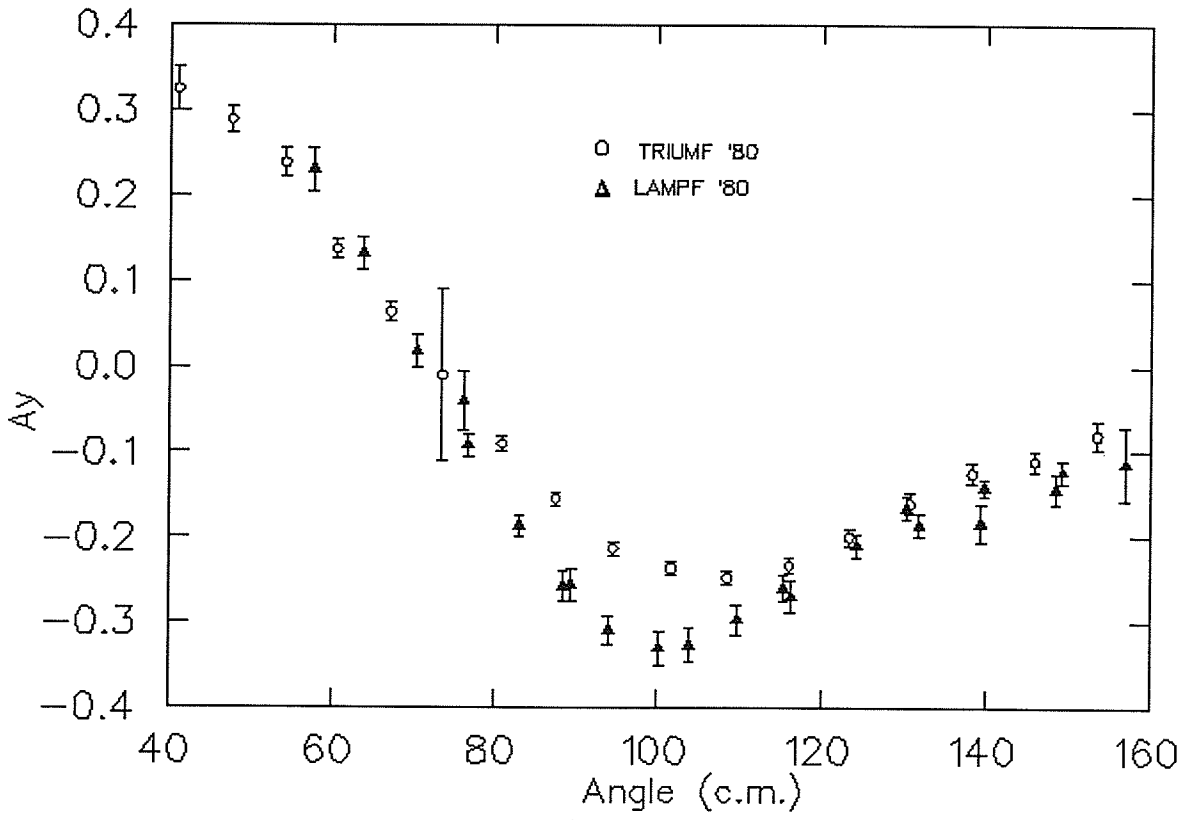


Figure 1.2: Measured values of 425 MeV $A_y$. The soild triangles are the LAMPF data [6] and the open squares are the BASQUE data measured at TRIUMF [7].

momentum ($k \rightarrow 0$) can be written as [10]

$$\epsilon_1 \simeq \sqrt{2} Q_d k^2, \tag{1.1}$$

where $Q_d$ is the quadrupole moment of the deuteron. In 1974, Binstock and Bryan [11] carried out an analysis of the sensitivity of various n-p observables to the phase parameters at around 50 MeV. They showed that the $\epsilon_1$ mixing parameter is sensitive to the normal to normal spin transfer coefficient, $D_t$, and the spin correlation parameter $A_{yy}$. Recently, Chulick et al. [12] carried out a similar analysis at 325 MeV. They studied the sensitivity of $D_t$, $R_t$ (the sideways to sideways spin transfer coefficient), and $A_{yy}$ to variations in the partial waves $\epsilon_1$,$^1P_1$ and $^3D_2$ respectively. For this they used Arndt's phase shift analysis program, SAID[13], and kept all other phases constant. Their finding about the sensitivity of $A_{yy}$ is summarized in fig 1.3. In fig 1.3(a) $A_{yy}$ seems to be sensitive to $\epsilon_1$ over the entire angle range. However, the sensitivity is not very large. The dependence of $A_{yy}$ on $^1P_1$ and $^3D_2$ is much more dramatic. In refs [14,15] it has also been pointed out that the most worthwhile measurement in n-p scattering is the spin correlation parameter, $A_{yy}$.

We also have investigated the effect on different n-p phase errors of adding an additional set of $A_{yy}$ data. The spring 1986 version of SAID was used and fifteen fake $A_{yy}$ data points with an anticipated error of $\pm 0.03$ over the angular range of $40^0 - 150^0(c.m.)$ at 220 MeV were added. Fig 1.4 shows the estimated uncertainties in various phases with and without the additional data points. Almost all the phases are affected, a maximum reduction by 35% is achieved for the $^3D_2$ phase error, confirming the assertion of ref. [12]. In order not to have bad data affecting several phases at the same time, it is necessary to have very weak correlations among phases. This additional set of fake $A_{yy}$ data also helps to reduce different correlation coefficients [Table

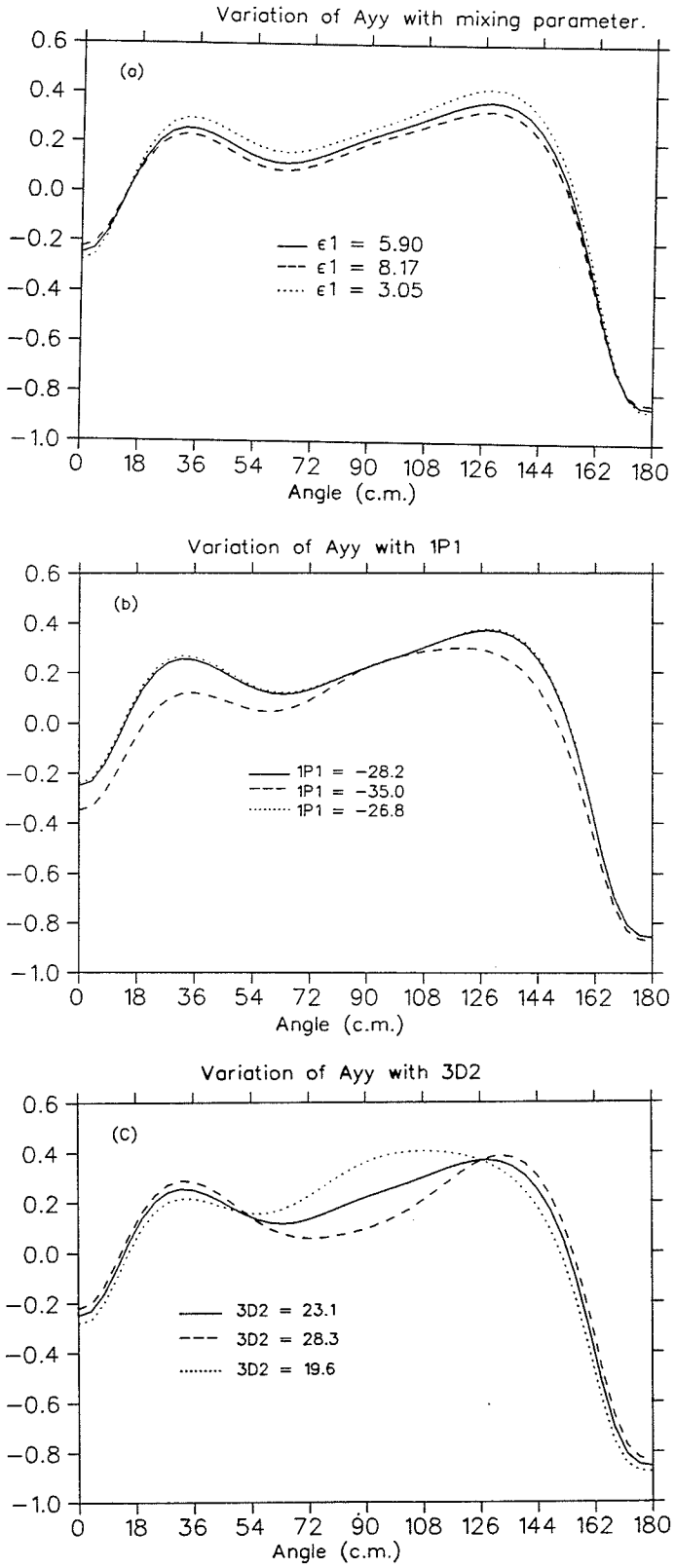


Figure 1.3: Sensitivity of 325 MeV $A_{yy}$ to different phase shifts.

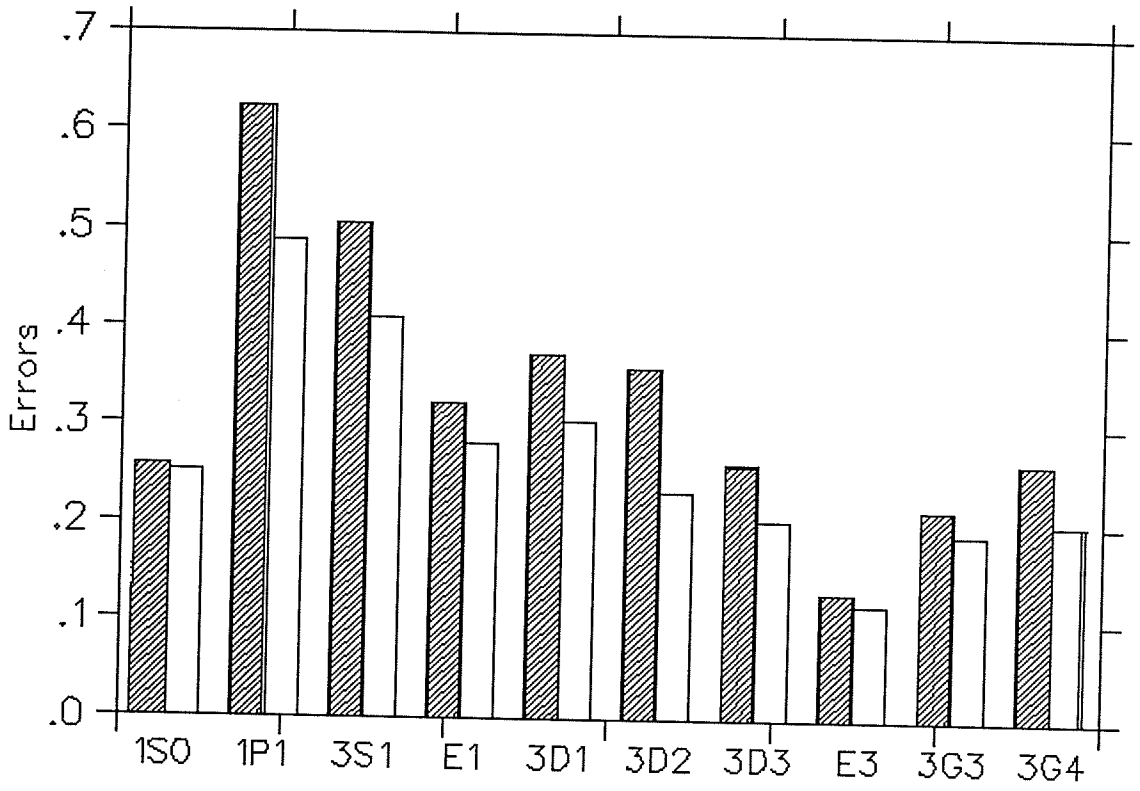


Figure 1.4: 220 MeV phase errors without (hatched area) and with (non-hatched area) fake $A_{yy}$ data

Table 1.2: Correlation Coefficients without and with $A_{yy}$ data at 220 MeV

| Correlation coefficients | Present values | With $A_{yy}$ | Reduction factor |
|---|---|---|---|
| ${}^3S_1 \times {}^3D_1$ | -0.600 | -0.403 | 1.48 |
| ${}^3S_1 \times {}^3D_2$ | -0.668 | -0.579 | 1.15 |
| ${}^3D_1 \times {}^3D_3$ | 0.698 | 0.672 | 1.04 |
| ${}^3D_2 \times {}^3D_3$ | 0.250 | 0.185 | 1.35 |

Table 1.3: World data base of the spin correlation parameter, $A_{yy}$

| Energy MeV | Angular range | No. of points | Year | Ref |
|---|---|---|---|---|
| 14.0 | 90 | 1 | 1984 | [16] |
| 23.1 | 130-174 | 4 | 1966 | [17] |
| 25.0 | 90-125 | 3 | 1986 | [18] |
| 50.0 | 109-174 | 4 | 1977 | [19] |
| 50.0 | 108-174 | 4 | 1980 | [20] |
| 15-50 | 90-120 | 29 | 1986 | [21] |
| 19-50 | 30-60 | 45 | 1988 | [22] |
| 181.0 | 57-126 | 10 | 1987 | [23] |
| 395.0 | 72-166 | 15 | 1983 | [24] |
| 465.0 | 71-166 | 15 | 1983 | [24] |
| 565.0 | 71-166 | 15 | 1983 | [24] |
| 665.0 | 72-166 | 15 | 1983 | [24] |

1.2]. At other energies the situation is similar. For example, at 325 MeV the ${}^3S_1$,${}^3D_1$ and ${}^3D_3$ phase errors are reduced by a factor of 1.5 to 1.8; and at 425 MeV the ${}^3S_1$ and ${}^3D_2$ phase errors are reduced by a factor of 1.3 by the addition of fifteen data points as described above for 220 MeV.

Not only will the phase shift analyses benefit from the present measurement, the data will also have a profound effect on the different potential model calculations. Fig 1.5 illustrates the predictions of $A_{yy}$ made by vari-

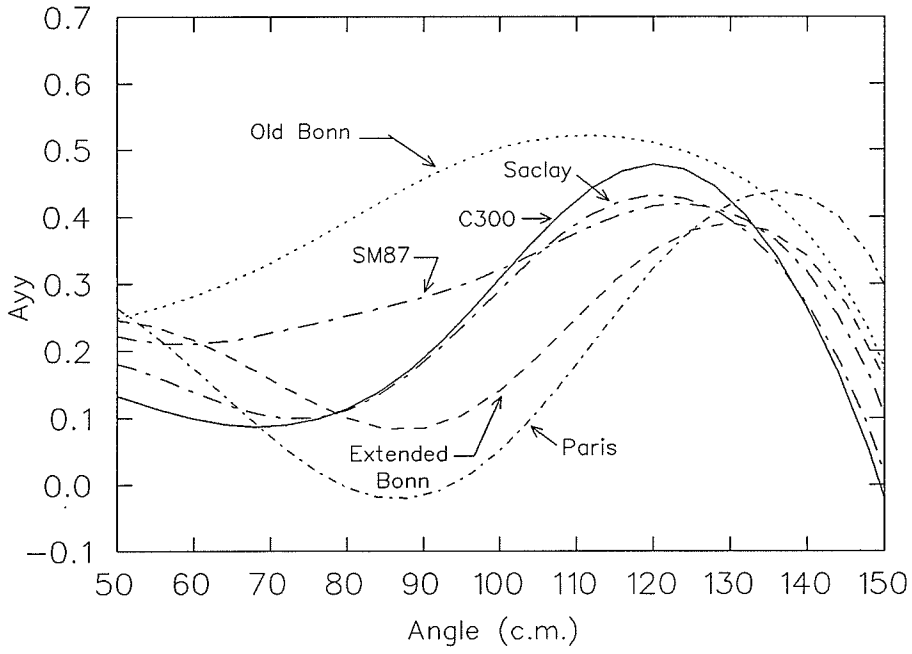


Figure 1.5: Predicted values of $A_{yy}$ at 325 MeV. Old Bonn solution is from ref. [38] and extended Bonn solution is from ref. [47]

ous phase shift analyses and the potential models at 325 MeV. As is evident, the potential models disagree with each other almost over the entire angle range. The story is similar at the other two energies of our measurements. This wide range of predictions has existed for quite some time and is due to the scarcity of accurate spin correlation data in the energy range 1-1000 MeV. Table 1.3 summarizes the world measurements of $A_{yy}$ in this energy range.

Apart from the most recent IUCF $A_{yy}$ data at 181 MeV [23], there hasn't been any measurement made between 100 and 395 MeV. There are $A_{yy}$ data available from LAMPF at 395, 465, 565 and 665 MeV [24]. Fig 1.6 shows these data together with phase shift predictions. Typical errors in the LAMPF data are $\pm 0.06$ to $\pm 0.15$, and no simultaneous measurement of left-right scattering was made. Thus the possibility of remaining systematic errors in this experiment cannot be ruled out. Also because of the continuous energy neutron beam, very wide energy bins were used. Aside from being reported in a conference proceedings these data have never been published. Bystricky et al. in their most recent phase shift analysis [3] have omitted the LAMPF 665 MeV $A_{yy}$ data; the inclusion of these data makes the $\chi^2$ of fit significantly worse.

## 1.2 n-p Scattering Formalism :

The discussion of this section is based on two articles, one by La France and Winternitz [25] and the other one by Bystricky, Lehar and Winternitz (referred to as BLW) [26]. Both articles were published in J. Physique (Paris) two years apart. The interaction between two spin-$\frac{1}{2}$ particles is most conveniently described in the M-matrix formalism. The scattering matrix M is an

operator which connects the final ($f$) and initial ($i$) spin states of two spinor particles through the relation :

$$\chi_f = M\chi_i \tag{1.2}$$

The most general form of the scattering matrix which is invariant under spatial rotation, parity inversion, time reversal and isospin can be written as :

$$\begin{aligned} M(\mathbf{k_f}, \mathbf{k_i}) &= \frac{1}{2}[(a+b) + (a-b)(\sigma_1.\mathbf{n})(\sigma_2.\mathbf{n}) + (c+d)(\sigma_1.\mathbf{m})(\sigma_2.\mathbf{m}) + \\ &\quad +(c-d)(\sigma_1.\mathbf{l})(\sigma_2.\mathbf{l}) + e(\sigma_1+\sigma_2).\mathbf{n}] \end{aligned}$$

where the amplitudes $a, b, c, d$, and $e$ are complex functions of energy and scattering angle. $\mathbf{l}, \mathbf{m}$ and $\mathbf{n}$ are the basis vectors for an orthogonal right handed coordinate system and are defined as :

$$\mathbf{l} = \frac{\mathbf{k_f} + \mathbf{k_i}}{|\mathbf{k_f} + \mathbf{k_i}|}, \ \mathbf{m} = \frac{\mathbf{k_f} - \mathbf{k_i}}{|\mathbf{k_f} - \mathbf{k_i}|}, \ \mathbf{n} = \frac{\mathbf{k_i} \times \mathbf{k_f}}{|\mathbf{k_i} \times \mathbf{k_f}|} \tag{1.3}$$

where $\mathbf{k_i}$ and $\mathbf{k_f}$ are unit vectors along the incident and the scattered particle center of mass momenta (see figure 1.7); $\sigma_1$ and $\sigma_2$ are the Pauli matrices for the first and second nucleons. In the laboratory system (l.s) and in the non relativistic limit $\mathbf{l}$ represents the direction of motion of the scattered nucleon, $\mathbf{n}$ is perpendicular to the scattering plane and $-\mathbf{m}$ is the direction of motion of the recoil particle. From the above figure it is seen that the cartesian coordinates $\hat{x}, \hat{y}$ and $\hat{z}$ are given by :

$$\hat{x} = \hat{\mathbf{n}} \times \hat{\mathbf{k_i}}, \ \hat{y} = \hat{\mathbf{n}}, \ \hat{z} = \hat{\mathbf{k_i}} \tag{1.4}$$

The Pauli principle implies that for the I=0 part of the n-p system the above five amplitudes obey the following symmetry conditions :

$$a(\theta) = a(\pi - \theta)$$

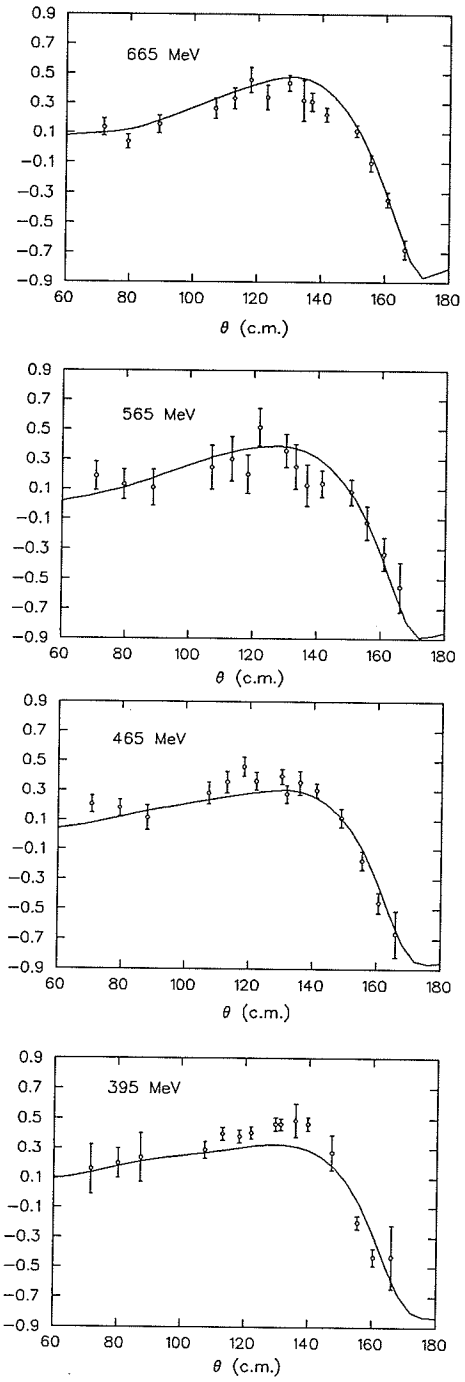


Figure 1.6: LAMPF data of $A_{yy}$ [21]. The solid curves are predictions from the Arndt et al. phase shift analysis (SP88) which includes the LAMPF data.

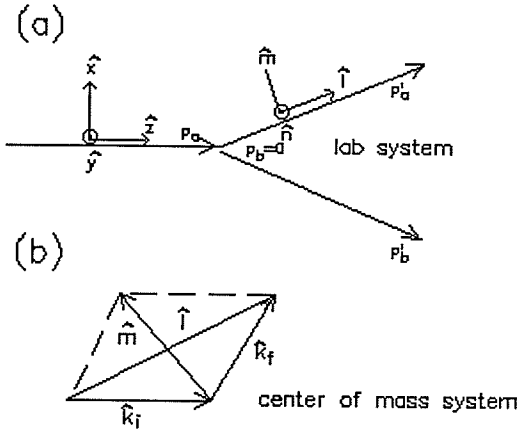


Figure 1.7: (a) Laboratory system : $p_a, p_b$ are the initial nucleon momenta; $p_a^{'}, p_b^{'}$ are the final momenta. (b) Center of mass system : $k_i, k_f$ initial and final momenta. Note that for $m_a = m_b$ in the lab system $\hat{l} = \hat{p_a}^{'}, \hat{m} = -\hat{p_b}^{'}$

$$
\begin{aligned}
b(\theta) &= c(\pi - \theta) \\
c(\theta) &= b(\pi - \theta) \\
d(\theta) &= -d(\pi - \theta) \\
e(\theta) &= -e(\pi - \theta)
\end{aligned}
$$

Since the above amplitudes are complex numbers, a total of 10 parameters are to be determined. The overall phase is not needed, so at least 9 experiments must be done for the I=0 and I=1 states of the nucleon-nucleon system to completely determine the magnitudes and relative phases of five complex amplitudes. However, as pointed out in ref. [27], to determine the amplitudes uniquely one needs to do more than nine experiments. This is because the amplitudes are bilinear in 9 unknowns so ambiguities may result in the construction of M from 9 experiments at a given angle. Below inelastic threshold ($\leq 280MeV$) the number of independent experiments needed for each isospin state is reduced to 5 because of the unitarity relations which relate the imaginary parts of the amplitudes at one angle to integrals of their products over all angles [28].

BLW use the notation $\alpha_{pqik}$ to describe the various spin observables. The subscript $pqik$ stands for the polarization of scattered, recoil, beam and target particles respectively. If any of the polarizations is zero (in the initial state) or not measured (in the final state), a '0' is used in the subscript. For example if the polarization of the recoil and scattered particles are not measured then $A_{00i0}$ is the analyzing power for polarized beam and unpolarized target. For polarized target and unpolarized beam the same is written as $A_{000k}$. Whereas for polarized beam and polarized target the initial state spin correlation parameter is $A_{00ik}$.

If the beam is polarized but the target is not and if the polarization

of the scattered particle is measured, then the depolarization tensor or the polarization transfer from beam to scattered particle is $D_{p0i0}$. The same transfer coefficient for the recoil particle is written as $K_{0qi0}$. If we have unpolarized beam and unpolarized target and the polarization of scattered or recoil particle is measured then the polarization of scattered particle is $P_{p000}$ and for recoil particle it is $P_{0q00}$. The final state spin correlation parameter is $C_{pq00}$.

Since the experiments are done in the lab it will be better if all the spin observables are defined in the laboratory system. One such system has already been described in fig 1.7. However, for the present purpose the system adopted by BLW where they define $\hat{k}, \hat{k}'$ and $\hat{k}''$ as the unit vectors in the direction of the initial, scattered and recoil particle momenta will be used. Three transverse vectors are defined as:

$$\hat{s} = \hat{n} \times \hat{k},\ \hat{s}' = \hat{n} \times \hat{k}',\ \hat{s}'' = \hat{n} \times \hat{k}''$$

where $\hat{n}$ is the unit vector perpendicular to the scattering plane. Some of the spin observables in the laboratory system are listed in table 1.4.

Besides the BLW formalism there are many ways of describing the NN interaction. Only two of them will be mentioned here. First, the helicity formalism by Jacob and Wick [29] as adapted by Spinka [30] who defines amplitudes as :

$$\phi_s = (\phi_1 - \phi_2)/2 \tag{1.5}$$

$$\phi_t = (\phi_1 + \phi_2)/2 \tag{1.6}$$

$$\phi_T = (\phi_3 - \phi_4)/2 \tag{1.7}$$

$$\phi_\tau = (\phi_3 + \phi_4)/2 \tag{1.8}$$

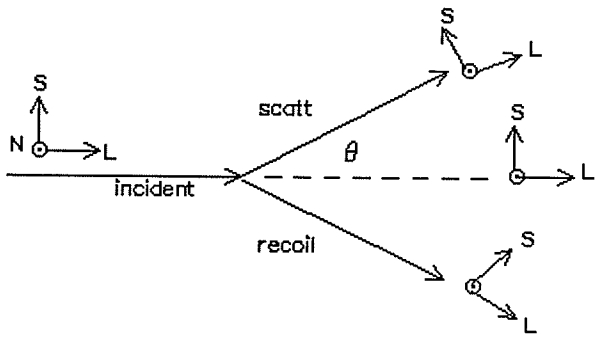


Figure 1.8: Ann Arbor convention.

$$\phi_5 \;=\; \phi_5 \tag{1.9}$$

The amplitude $\phi_s$ arises from the spin-singlet transition, $\phi_T$ and $\phi_\tau$ contain triplet contributions whereas, $\phi_t$ and $\phi_5$ contain coupled triplet terms. The helicity amplitudes $\phi_{1,\ldots,5}$ are defined in table 1.5 in terms of BLW amplitudes. In the same table we also have expressed the different spin observables in terms of the Spinka amplitudes.

The second convention mentioned is the 'Ann Arbor' convention adopted in the 1977 Ann Arbor conference on Higher Energy Polarized Proton Beams [31]. An orthogonal coordinate system **N,L,S** is defined in all but the target particles' rest frame (fig 1.8). **L** is along the direction of motion of the particle (incident, recoil or scattered), **N** is perpendicular to the scattering plane, and **S** is along $\mathbf{N} \times \mathbf{L}$. Like BLW it uses D and K to specify whether the polarization of the scattered or recoil particle is measured. According to this convention any spin observable is written as $\alpha_{beam,target;scattered,recoil}$ where beam etc. in the subscript refer to the direction of polarization. The

correspondence among three different conventions is summarized in Table 1.6. The convention in the first column is that of Hoshizaki [32] and Wolfenstein [33], throughout the present text we will use this convention. Fig 1.9 shows schematic pictures in the lab system of some spin observables. Note that the scattered particle is on the left of the incident beam and the recoil is on the right.

## 1.3 Phase Shift Analysis

As is mentioned in the previous section, at least 5 experiments are to be done at each angle and energy for a complete reconstruction of the scattering matrix. For n-p scattering the experiments must be carried out over the entire angle range of $0 \rightarrow \pi$. In reality this is hardly achieved; instead, one relies on the phase shift parametrization of the scattering matrix which utilizes data taken over certain angles and energies and compensates for the lack of data at some other points. The idea behind the phase shift analysis is to decompose the initial and final wave functions into a series of partial waves, each characterized by a definite value of angular momentum. Because of the interaction, the phases of the scattered waves are shifted by an amount $\delta_{LJ}$. The greater the interaction the larger the shift. The strength of the interaction depends on the values of angular momentum, L, and in consequence on the impact parameter, b, which is related to L by the semiclassical expression : $p_i b = (L + 1/2)\hbar$, $p_i$ being the initial momentum.

How many partial waves or in other words, how many different angular momentum states are involved, depends on the incident energy. Because of the short range nature of the nuclear force, the number of partial waves is generally restricted to 8-10 at intermediate energies (100-1000 MeV). In the

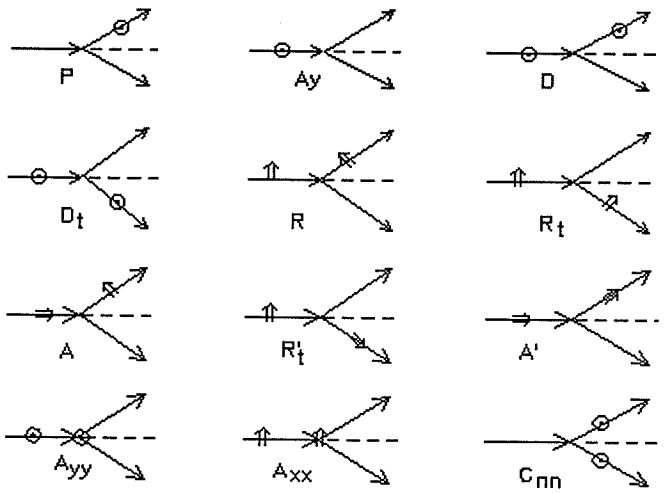


Figure 1.9: Spin observables in the laboratory frame. P is the polarization parameter, $A_y$ is the analyzing power. $D, D_t, R, R_t, A, A_t, R'_t$, and $A'$ are the polarization transfer coefficients. $A_{yy}$ etc. are the spin correlation parameters.

two nucleon interaction, the total angular momentum J, total spin S and parity $\Pi = (-1)^L$ are conserved quantities and hence a useful representation will be one where these conserved quantities are diagonal. The angular momentum states that are available for the I=0 or I=1 parts of the n-p scattering matrix are determined by the antisymmetry condition :

$$(-1)^{S+I+L} = -1 \tag{1.10}$$

where I is the isospin. Table 1.7 summarizes some of the allowed states for n-p scattering. It is convenient to describe the method of phase shift analysis in four steps.

In the first step, the scattering matrix, $S$, is expressed in terms of the phase shifts by:

$$S = e^{2i\delta_{LJ}} \tag{1.11}$$

The relation between the matrices $M$ and $S$ in the singlet-triplet representation [34] is given by :

$$< sm_s|M|s'm'_s >= \frac{2\pi}{ik} < \theta_f\phi_f; sm_s|S-1|s'm'_s; \theta_i\phi_i > \tag{1.12}$$

where k is the wave number of the relative motion and $\theta$, $\phi$ are the c.m. scattering angles. Below the pion production threshold ($\leq$ 280 MeV), S is unitary, which means the interaction process is completely elastic; the incoming flux is equal to the outgoing flux.

Table 1.4: Spin observables in terms of scattering amplitudes in the laboratory system

$$
\begin{aligned}
\sigma \equiv I_{0000} &= \sigma C_{nnnn} = \tfrac{1}{2}(|a|^2+|b|^2+|c|^2+|d|^2+|e|^2) \\
\sigma C_{nn00} &= \sigma A_{00nn} = \tfrac{1}{2}(|a|^2-|b|^2-|c|^2+|d|^2+|e|^2) \\
\sigma D_{n0n0} &= \sigma D_{0n0n} = \tfrac{1}{2}(|a|^2+|b|^2-|c|^2-|d|^2+|e|^2) \\
\sigma K_{0nn0} &= \sigma K_{n00n} = \tfrac{1}{2}(|a|^2-|b|^2+|c|^2-|d|^2+|e|^2) \\
\sigma C_{llll} &= \sigma C_{mmmm} = \tfrac{1}{2}(|a|^2+|b|^2+|c|^2+|d|^2-|e|^2) \\
\sigma P \equiv \sigma P_{n000} &= \sigma P_{0n00} = \sigma A_{000n} = \Re\, a^* e \\
\sigma A_{00ss} &= \Re(a^*d)\cos\theta + Re(b^*c) - \Im(d^*e)\sin\theta \\
\sigma A_{00sk} &= \sigma A_{00ks} = -\Re(a^*d)\sin\theta - \Im(d^*e)\cos\theta \\
\sigma A_{00kk} &= -\Re(a^*d)\cos\theta + \Re(b^*c) + \Im(d^*e)\sin\theta \\
\sigma D_{s'0s0} &= \Re(a^*b)\cos(\alpha+\tfrac{\theta}{2}) + \Re(c^*d)\cos(\alpha-\tfrac{\theta}{2}) - \Im(b^*e)\sin(\alpha+\tfrac{\theta}{2}) \\
\sigma D_{s'0k0} &= -\Re(a^*b)\sin(\alpha+\tfrac{\theta}{2}) + \Re(c^*d)\sin(\alpha-\tfrac{\theta}{2}) - \Im(b^*e)\cos(\alpha+\tfrac{\theta}{2}) \\
\sigma D_{k'0s0} &= \Re(a^*b)\sin(\alpha+\tfrac{\theta}{2}) + \Re(c^*d)\sin(\alpha-\tfrac{\theta}{2}) + \Im(b^*e)\cos(\alpha+\tfrac{\theta}{2}) \\
\sigma D_{k'0k0} &= \Re(a^*b)\cos(\alpha+\tfrac{\theta}{2}) - \Re(c^*d)\cos(\alpha-\tfrac{\theta}{2}) - \Im(b^*e)\sin(\alpha+\tfrac{\theta}{2}) \\
\sigma K_{0s''s0} &= -\Re(a^*c)\cos(\beta+\tfrac{\theta}{2}) - \Re(b^*d)\cos(\beta-\tfrac{\theta}{2}) + \Im(c^*e)\sin(\beta+\tfrac{\theta}{2}) \\
\sigma K_{0s''k0} &= \Re(a^*c)\sin(\beta+\tfrac{\theta}{2}) - \Re(b^*d)\sin(\beta-\tfrac{\theta}{2}) + \Im(c^*e)\cos(\beta+\tfrac{\theta}{2}) \\
\sigma K_{0k''s0} &= -\Re(a^*c)\sin(\beta+\tfrac{\theta}{2}) - \Re(b^*d)\sin(\beta-\tfrac{\theta}{2}) - \Im(c^*e)\cos(\beta+\tfrac{\theta}{2}) \\
\sigma K_{0k''k0} &= -\Re(a^*c)\cos(\beta+\tfrac{\theta}{2}) + \Re(b^*d)\cos(\beta-\tfrac{\theta}{2}) + \Im(c^*e)\sin(\beta+\tfrac{\theta}{2}) \\
\sigma K_{s'00k} &= -\Re(a^*c)\sin(\alpha+\tfrac{\theta}{2}) + \Re(b^*d)\sin(\alpha-\tfrac{\theta}{2}) - \Im(c^*e)\cos(\alpha+\tfrac{\theta}{2})
\end{aligned}
$$

Here $\alpha = \theta/2 - \theta_1, \beta = \theta/2 + \theta_2$, $\theta$ is the c.m. scattering angle, $\theta_1$ and $\theta_2$ are lab angles for scattered and recoil particles.

Table 1.5: Relation between BLW and helicity amplitudes

$$
\begin{aligned}
\phi_1 &\equiv <++|M|++> &&= \tfrac{1}{2}(a\cos\theta + b - c + d + ie\sin\theta) \\
\phi_2 &\equiv <++|M|--> &&= \tfrac{1}{2}(a\cos\theta - b + c + d + ie\sin\theta) \\
\phi_3 &\equiv <+-|M|+-> &&= \tfrac{1}{2}(a\cos\theta + b + c - d + ie\sin\theta) \\
\phi_4 &\equiv <+-|M|-+> &&= \tfrac{1}{2}(-a\cos\theta + b + c + d - ie\sin\theta) \\
\phi_5 &\equiv <++|M|-+> &&= \tfrac{1}{2}(-a\sin\theta + ie\cos\theta)
\end{aligned}
$$

where + or - indicates the nucleon helicity.

Spin observables and helicity amplitudes

$$
\begin{aligned}
\sigma &= (|\phi_s|^2 + |\phi_t|^2 + |\phi_T|^2 + |\phi_\tau|^2 + 2|\phi_5|^2) \\
\sigma P &= 2\Im(\phi_t^*\phi_5 - \phi_T\phi_5^*) \\
\sigma D_{n0n0} &= 2\Re(\phi_s^*\phi_\tau + \phi_t^*\phi_T + |\phi_5|^2) \\
\sigma K_{0nn0} &= -2\Re(\phi_s^*\phi_\tau - \phi_t^*\phi_T + |\phi_5|^2) \\
\sigma A_{00nn} &= \sigma C_{nn00} = -|\phi_s|^2 + |\phi_t|^2 + |\phi_T|^2 - |\phi_\tau|^2 + 2|\phi_5|^2 \\
\sigma A_{00ss} &= -|\phi_s|^2 + |\phi_t|^2 - |\phi_T|^2 + |\phi_\tau|^2 \\
\sigma A_{00sk} &= \sigma A_{00ks} = 2\Re(\phi_5^*(\phi_t - \phi_T)) \\
\sigma A_{00kk} &= -|\phi_s|^2 - |\phi_t|^2 + |\phi_T|^2 + |\phi_\tau|^2 \\
\sigma D_{s'0s0} &= -2\Re(\phi_5^*(\phi_s + \phi_\tau))\sin\theta_1 + 2\Re(\phi_s^*\phi_T + \phi_t^*\phi_\tau)\cos\theta_1 \\
\sigma D_{k'0k0} &= -2\Re(\phi_5^*(\phi_s + \phi_\tau))\sin\theta_1 + (\phi_s^*\phi_t + \phi_T\phi_\tau)\cos\theta_1 \\
\sigma K_{0s''s0} &= -2\Re(\phi_5^*(\phi_\tau - \phi_s))\sin\theta_2 - 2\Re(\phi_t^*\phi_\tau - \phi_s^*\phi_T)\cos\theta_2 \\
\sigma K_{0k''k0} &= -2\Re(\phi_5^*(\phi_\tau - \phi_s))\sin\theta_2 - (\phi_T\phi_\tau - \phi_s\phi_t)\cos\theta_2
\end{aligned}
$$

Unitarity breaks down as the inelastic channels open up. In that case the matrix S is redefined as :

$$S = \eta e^{2i\delta_{LJ}} \tag{1.13}$$

where $\eta$ is the elasticity parameter with values varying between 0 - 1. Another way of handling the inelasticity is to make the phase shifts complex,thereby allowing the absorption and production of extra particles. Note that the states with L=J$\pm$1 have the same J and parity and thus are free to mix. The S matrix can still be diagonalized by writing it in the following form first prescribed by Stapp,Ypsilantis and Metropolis [35].

$$S = \begin{bmatrix} e^{i\bar{\delta}_{J-1,J}} & 0 \\ 0 & e^{i\bar{\delta}_{J+1,J}} \end{bmatrix} \begin{bmatrix} cos2\bar{\epsilon_J} & isin2\bar{\epsilon_J} \\ isin2\bar{\epsilon_J} & cos2\bar{\epsilon_J} \end{bmatrix} \begin{bmatrix} e^{i\bar{\delta}_{J-1,J}} & 0 \\ 0 & e^{i\bar{\delta}_{J+1,J}} \end{bmatrix}$$

where $\bar{\delta}_{LJ}$ are the nuclear bar phase shifts and $\bar{\epsilon_J}$ is the bar mixing parameter. The phase shifts defined in eqn. (1.13) for the states not involving mixing are the same as the bar phase shifts. Note that the mixing parameter gives the proportions into which an incoming beam in one angular momentum state divides between the two outgoing states with the same J values.

The second step involves writing the five scattering amplitudes $(a \ldots e)$ in terms of singlet-triplet matrix elements which are conventionally written as :

$$M_{ss} = < 00|M|00 >, \quad M_{m_s m'_s} = < lm_s|M|lm'_s > \tag{1.14}$$

The amplitudes in this representation are :

$$\begin{aligned} a &= \frac{1}{2}(M_{11} + M_{00} - M_{1-1}) \\ b &= \frac{1}{2}(M_{11} + M_{ss} + M_{1-1}) \end{aligned}$$

Table 1.6: Correspondence among different conventions

| Hoshizaki | BLW | Ann Arbor | Definitions |
|---|---|---|---|
| $P^1$ | $P_{n000}$ | $P_{0,0;N,0}$ | Polarization of scattered particle. |
| $P^2$ | $P_{0n00}$ | $P_{0,0;0,N}$ | Polarization of recoil particle. |
| $A_y$ | $A_{00n0}$ | $A_{N,0;0,0}$ | Analyzing power for polarized beam. |
| $A_y$ | $A_{000n}$ | $A_{0,N;0,0}$ | Analyzing power for polarized target. |
| $R$ | $D_{s'0s0}$ | $D_{S,0;S,0}$ | Sideways to sideways spin transfer between incident beam and scattered particle |
| $R_t$ | $K_{0s''s0}$ | $K_{S,0;0,S}$ | Same for recoil particle |
| $R'$ | $D_{k'0s0}$ | $D_{S,0;L,0}$ | Sideways to longitudinal spin transfer between incident beam and scattered particle |
| $R'_t$ | $K_{0k''s0}$ | $K_{S,0;0,L}$ | Same for recoil particle |
| $D$ | $D_{n0n0}$ | $D_{N,0;N,0}$ | Normal to normal spin transfer between incident beam and scattered particle |
| $D_t$ | $K_{0nn0}$ | $K_{N,0;0,N}$ | Same for recoil particle |
| $A'$ | $D_{k'0k0}$ | $D_{L,0;L,0}$ | Longitudinal to longitudinal spin transfer between beam and scattered particle |
| $A'_t$ | $K_{0k''k0}$ | $K_{L,0;0,L}$ | Same for recoil particle |
| $A$ | $D_{s'0k0}$ | $D_{L,0;S,0}$ | Longitudinal to sideways spin transfer between beam and scattered particle |
| $A_t$ | $K_{0s''k0}$ | $K_{L,0;0,S}$ | Same for recoil particle |
| $A_{yy}$ | $A_{00nn}$ | $A_{N,N;0,0}$ | Initial state spin correlation parameter with beam and target both polarized in normal (N) direction. |
| $A_{xx}$ | $A_{00ss}$ | $A_{S,S;0,0}$ | Same with beam and target polarizations along sideways (S) |
| $A_{zz}$ | $A_{00kk}$ | $A_{L,L;0,0}$ | Same with longitudinally polarized beam and target |

Table 1.7: The allowed partial waves for NN scattering

| J | I = 0 | I = 1 |
|---|---|---|
| 0 | - | ${}^1S_0, {}^3P_0$ |
| 1 | ${}^1P_1, {}^3S_1, \epsilon_1, {}^3D_1$ | ${}^3P_1$ |
| 2 | ${}^3D_2$ | ${}^1D_2, {}^3P_2, \epsilon_2, {}^3F_2$ |
| 3 | ${}^1F_3, {}^3D_3, \epsilon_3, {}^3G_3$ | ${}^3F_3$ |
| 4 | ${}^3G_4$ | ${}^1G_4, {}^3F_4, \epsilon_4, {}^3H_4$ |

$$
\begin{aligned}
c &= \frac{1}{2}(M_{11} - M_{ss} + M_{1-1}) \\
d &= \frac{1}{\sqrt{2}\sin\theta}(M_{10} + M_{01}) \\
e &= \frac{1}{\sqrt{2}}(M_{10} - M_{01})
\end{aligned}
$$

The singlet-triplet matrix elements, $M_{ss}$ and $M_{m_s m_s'}$ are expressed in terms of Legendre polynomial series and partial wave amplitudes $\alpha_{LJ}$. According to ref. [35] the parametrized form of $\alpha_{LJ}$ in terms of nuclear bar phase shifts $\bar{\delta}_{LJ}$ and mixing parameter $\epsilon_J$ can be written as :

$$
\begin{aligned}
\alpha_J &= \exp(2i\bar{\delta}_J) - 1 \\
\alpha_{J,J} &= \exp(2i\bar{\delta}_{J,J}) - 1 \\
\alpha_{J\pm1,J} &= \cos 2\epsilon_J \exp(2i\bar{\delta}_{J\pm1,J}) - 1 \\
\alpha^J &= i \sin 2\epsilon_J \exp(i(\bar{\delta}_{J+1,J} + \bar{\delta}_{J-1,J}))
\end{aligned}
$$

For p-p scattering, $\bar{\delta}_J$ also contains the contribution from the Coulomb interaction.

In the next step, the contribution due to the exchange of one pion is explicitly included in the scattering amplitude. Since the long range part of the interaction is very well described by the exchange of a single pion, the higher order partial waves are replaced by the Born approximation of

one pion exchange contribution. The pion-nucleon coupling constant, $g_\pi$, is introduced in the analysis as a parameter.

In the final step, the spin observables are calculated from an initial set of phase shifts. It is not trivial to calculate the phases from the known values of the observables. So the reverse course is almost always taken. An initial set of phase shifts is guessed at the beginning, the calculated observables from this trial set are compared with the experimental values, the fit is then improved by stepwise iteration of the phase shifts. The goodness of fit is determined by defining a $\chi^2$ such as [36] :

$$\chi^2 = \sum_{n=1}^{N_{exp}} \left[ \sum_i \left( \frac{(X_n \theta_i(p) - \theta_i)^2}{\sigma_i^2} + \frac{(X_n - 1)^2}{\Delta X_n^2} \right) \right] \tag{1.15}$$

where $N_{exp}$ = number of experiments , $\theta_i(p)$ = observable predicted by parameter p, $\theta_i$ = observable as measured, $\sigma_i$ = error in the i'th data point, $X_n$ = normalization parameter on n'th experiment, and $\Delta X_n$ = normalization error on the n'th experiment. The phase shifts are varied to minimize this $\chi^2$. At the point of a solution the above can be approximated by :

$$\chi^2 \simeq \chi_0^2 + \frac{1}{2} \Delta\tilde{p} A \Delta p \tag{1.16}$$

where $\chi_0^2 = \chi^2$ at the minimum$(p = p_0)$ , $\Delta p = p - p_0, \Delta\tilde{p}$ = transpose of vector $\Delta p$ and $A$ = second derivative matrix defined by

$$A_{jk} = \frac{\partial^2 \chi^2}{\partial p_j \partial p_k} \tag{1.17}$$

For a good fit $\chi^2$ should be equal to $N_{exp} - m$ , m being the number of phase shifts. Note that the $\chi^2$ defined in this way takes care of the normalization uncertainty in the data set.

The phase shift analyses are carried out either in an energy-dependent way or an energy independent way. In the former case, an energy interval

is chosen and the phase shifts are given an appropriate energy dependence over the entire energy range. This energy interval can be anywhere between 0 and 1000 MeV. For example, the Saclay-Geneva analysis [3] is performed in the four overlapping intervals; 10-220 MeV, 130-450 MeV, 380-610 MeV, and 520-800 MeV. In each of these energy intervals the phase shifts are given an energy dependence of the form :

$$\sum_{n=0}^{3} \frac{a_{LJn}}{n!}(T - T_0)^n \tag{1.18}$$

where $T_0$ is the central energy of the interval and $a_{LJn}$ are variable parameters. On the other hand, Arndt et al. [4] have performed the energy dependent analysis over a much larger energy interval, 0-1000 MeV. The energy dependence is expressed in a parametric form :

$$\sum_i \alpha_{li} f_{li}$$

where the $f_{li}$ are the energy dependent expansion bases [37], $\alpha_{li}$ are the adjustable parameters.

In the energy independent analysis a particular energy (or a very narrow band of energies) is chosen and the phase shifts are determined at that energy only. Arndt et al. [4] have done 18 such single energy analyses between 0-1000 MeV. Some of the single energy intervals are summarized in table 1.1. The two methods are now complementary to each other. For example, over the narrow energy range bands where the energy independent analyses are carried out, instead of shifting the data so that they all fall on the same energy the phase shifts are given an energy dependence whose form is basically derived from the energy dependent analysis.

In table 1.8 some of the 325 MeV phase shift values obtained from the different analyses are summarized. The difference among the various predictions can be attributed to the specific selection of data sets and the different

Table 1.8: 1987 I = 0 phase shifts (in degrees) at 325 MeV

| State | Arndt | Basque | Saclay | Paris | Bonn* |
|---|---|---|---|---|---|
| $^1P_1$ | -28.16 | -35.05 | -32.93 | -26.83 | -30.84 |
| $^3S_1$ | 2.25 | 0.93 | 2.04 | 0.68 | 4.54 |
| $^3D_1$ | -24.16 | -25.38 | -24.96 | -25.20 | -23.86 |
| $\epsilon_1$ | 5.90 | 6.23 | 6.10 | 5.19 | 3.05 |
| $^3D_2$ | 23.06 | 23.30 | 20.95 | 28.32 | 19.60 |
| $^1F_3$ | -5.79 | -5.63 | -4.58 | -5.71 | -5.50 |
| $^3D_3$ | 3.54 | 2.69 | 3.44 | 4.74 | 3.71 |

* Old Bonn potential [38]

ways the higher partial waves, inelasticity and energy dependence are handled.

## 1.4 Phenomenological Potentials :

NN scattering has been extensively studied using phenomenological [1] potentials, especially below the pion production threshold ($\leq 280\ MeV$). The models differ in their handling of the short ($r \leq 0.8\ fm$) and medium range parts of the interaction, but the long range part in every model is always explained in terms of one pion exchange (OPE). A potential is said to be phenomenological when it is derived from purely phenomenological parameters adjusted to fit the data or a part of it may be based on some form of theory. Recently attempts have been made to explain the short range (SR) part in terms of quarks and gluons. However, that has not been very successful in explaining all the details of the interaction. In the present section we shall limit ourselves to discussing only two of many phenomenological

[1] We are not making any distinction between phenomenological and semi-phenomenological form of the potentials

potentials, namely the PARIS and BONN potentials.

### 1.4.1 Paris Potential :

There are two forms of this potential. The first form [39] is of mixed origin; the long and medium range (LR+MR) parts of the potential are derived on the basis of dispersion theory whereas the short range part is purely phenomenological. In the LR+MR part the contributions from one pion exchange, correlated and uncorrelated two pion exchange and $\omega$-exchange $(\pi - 2\pi - \omega)$ are taken into account. The $J > 2$ phase shifts are very well reproduced on the basis of these contributions [40]. The LR+MR part is sharply cutoff at $r \simeq 0.8\ fm$ and the SR part is described by a constant soft core. The general form of the potential is :

$$V(r,E) = V_{theor}(r,E)f(r) + V_{phen}(r,E)[1 - f(r)] \tag{1.19}$$

where $E$ is the c.m. energy and

$$f(r) = \frac{(pr)^{\alpha}}{1 + (pr)^{\alpha}} \tag{1.20}$$

where $p = 1.25\ fm^{-1}$ and $\alpha = 10$. The function, $f(r)$, introduces the sharp cutoff mentioned above. In this way the effect of the phenomenological part , $(V_{phen})$, for $r > 1\ fm$ is reduced significantly. Both $V_{theor}$ and $V_{phen}$ contain all five components of the potential, viz. : central (C), spin orbit(SO), spin-spin (SS), tensor (T) and quadratic spin orbit (SO2). The only free parameter in the theoretical part is the coupling constant $g_{\omega}(= 9.5)$. The central component of the theoretical part has been found to have weak but significant energy dependence, all other terms being taken as energy independent. Below the pion production threshold, this dependence is almost linear in energy. The phenomenological part of the interaction is determined by

fitting phase shifts below J=6 for energies up to 330 MeV. Like the LR+MR part, the SR part is also assigned a linear energy dependence. For convenience, $V_{phen}$ is taken to be independent of r and is therefore only a function of energy. The energy dependent form of the full potential is :

$$V(r,E) = U(r) + EW(r) \tag{1.21}$$

with

$$\begin{aligned} U(r) &= U_{theor}(r)f(r) + C[1-f(r)] \\ W(r) &= W_{theor}f(r) + C'[1-f(r)] \end{aligned}$$

where, $C'$ is zero for all but the central part. The total number of free parameters for the phenomenological part is 12 (6 for each isospin state), ten of them are for five components of the potential and two are the slopes of the energy dependence ($C'$).

In the second form of the potential the Paris group has parametrized their original NN potential in a simple analytic form [41] which is better suited for many-body calculations. This form of the potential is quite useful, valid for all r, and there is no distinction between theoretical and phenomenological parts. The total number of free parameters in this form is about 20 [42]. Because of its pure phenomenological nature most of the parameters have no physical meaning. The parameters are determined by fitting the shapes of the potentials to the experimental data. Instead of an energy dependence the central component of the potential has been given a $p^2$ dependence. The disagreement between this form and the original form of the potential is up to a few percent beyond 1 fm or so.

A reasonably good fit with $\chi^2 = 1.99$ for p-p scattering and 2.17 for n-p scattering has been achieved with this potential on the basis of a 1980 data

base. In terms of $\chi^2$ it is a much better potential than the Hamada-Johnston and Reid soft-core potentials.

### 1.4.2 Bonn Potential

The Bonn potential [43] [38] is based on a field theoretical meson-exchange model treating the nucleons, mesons and isobars on equal footing. The interaction Hamiltonian, H, is developed in relativistic time-ordered perturbation theory and contains the vertices from $NN$ and $N\Delta$ (fig1.10).The starting Hamiltonian for the model is:

$$H = H_0 + W \tag{1.22}$$

where the free Hamiltonian $H_0$ is expressed as :

$$H_0 = h_0 + t = \sum_{\beta} E_\beta b_\beta^\dagger b_\beta + \sum_{\alpha} \omega_\alpha a_\alpha^\dagger a_\alpha \tag{1.23}$$

The first term ($h_0$) in the above equation is the kinetic energy operator for baryons (nucleons) and the second term ($t$) is that for the mesons. $a_\alpha^\dagger, a_\alpha$ and $b_\beta^\dagger, b_\beta$ are the creation, annihilation operators for mesons and baryons with $\omega_\alpha$ and $E_\beta$ as the renormalized energies for them. The meson-baryon interaction term, W is taken as :

$$W = \sum_{\beta'\beta\alpha} W_{\beta'\beta\alpha} b_{\beta'}^\dagger b_\beta \alpha + hermitian\ conjugate. \tag{1.24}$$

The matrix elements $W_{\beta'\beta\alpha}$ are derived from the field integral :

$$W = -\int d^3x [\mathcal{L}_I(x) - \frac{\partial \mathcal{L}_I}{\partial \dot{\phi}_\alpha^{(\mu)}} \dot{\phi}_\alpha^{(\mu)}] \tag{1.25}$$

where $\dot{\phi}_\alpha^{(\mu)}$ is the time derivative of the field operator. The Lagrangian densities ($\mathcal{L}_I$) for pseudoscalar ($\pi, \eta$), scalar ($\delta$) and vector mesons ($\rho, \omega$) in terms

of coupling constants and gamma matrices are written as:

$$\begin{aligned}
\mathcal{L}_{NNps} &= \frac{f_{ps}}{m_{ps}}\bar{\psi}\gamma^5\psi\partial_\mu\phi_{ps} \quad (\pi,\eta) \\
\mathcal{L}_{NNs} &= g_s\bar{\psi}\psi\phi_s \quad (\delta) \\
\mathcal{L}_{NNv} &= g_v\bar{\psi}\gamma_\mu\psi\phi_v^\mu + \frac{f_v}{4m}\bar{\psi}\sigma_{\mu\nu}\psi(\partial^\mu\phi_v^\mu - \partial^\nu\phi_v^\mu) \quad (\rho,\omega)
\end{aligned}$$

where $m$ is the nucleon mass, $m_\alpha$ is the meson mass, $\psi, \phi_\alpha$ are the nucleon and meson field operators respectively. Similarly we can write the Lagrangian densities for the meson-nucleon-isobar vertices as:

$$\begin{aligned}
\mathcal{L}_{N\Delta\pi} &= \frac{f_{N\Delta\pi}}{m_\pi}\bar{\psi}\vec{T}\psi_\mu\partial^\mu\phi_\pi + h.c. \\
\mathcal{L}_{N\Delta\rho} &= i\frac{f_{N\Delta\rho}}{m_\rho}\bar{\psi}\gamma^5\gamma_\mu\vec{T}\psi_\nu(\partial^\mu\phi_\rho^\nu - \partial^\nu\phi_\rho^\mu)
\end{aligned}$$

where $\psi_\mu$ is the field operator for the $\Delta$ isobar and $\vec{T}$ is the isospin transition operator. In order to guarantee convergence at $r = 0$, i.e. to suppress the higher angular momentum contribution, a parametrized form factor $F_\alpha$, is introduced, where

$$F_\alpha = \frac{\Lambda_\alpha^2 - m_\alpha^2}{\Lambda_\alpha^2 + \vec{k}^2} \tag{1.26}$$

$\vec{k}$ being the momentum transfer and $\Lambda_\alpha$ is the cutoff mass which is fitted to data and is found to be in the range 1.3 to 1.5 GeV.

The long range force and the short range repulsion are quite well explained by the exchange of a single $\pi$ and $\omega$. A scalar, isovector $\delta$ meson is introduced to give a consistent description for S wave phase shifts. However, the situation with regard to $\delta$ is still not very satisfactory and thus this can be treated as another phenomenological parameter. The inclusion of a $2\pi$ exchange contribution explains quite satisfactorily the long and intermediate range of the interaction. The predicted phase shifts for $J = 4-6$

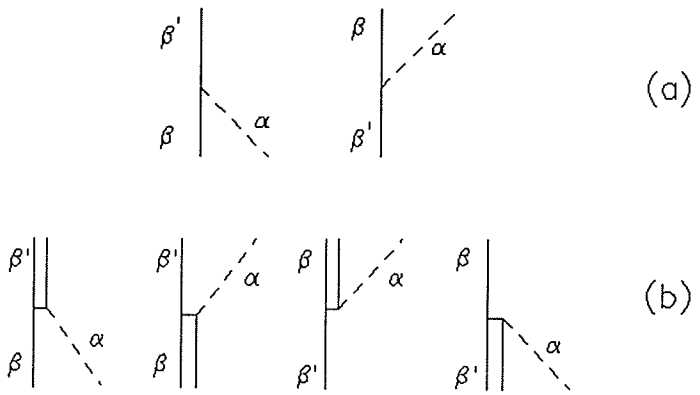


Figure 1.10: Meson-nucleon-nucleon(a) and meson-nucleon-isobar(b) vertices. The solid line is for a nucleon, the double line a $\Delta$ isobar and the dashed line a meson

agree very well with the values obtained from the phase shift analyses. In order to reduce the over-attraction from $2\pi$ exchange, the $\pi\rho$ contributions are introduced in the model. This improves the predictions of lower partial waves considerably. For example, $^3D_2$ and $^3D_3$ phase shifts obtained from other phenomenological potentials are too large at higher energies compared to the phase shift analysis values. The inclusion of $\pi\rho$ diagrams in the calculation makes them reasonable. The coupling parameter, $\epsilon_1$, predicted in this model is too high at low energies and too low at high energies. This is because of the fact that $\epsilon_1$ is not only related to the tensor force it is also correlated stongly with $^3D_1$ and $^3S_1$. For example, an increase in the $^3S_1$ lowers the value of $\epsilon_1$. Note that $^3S_1$ obtained from this potential model is somewhat larger than the values predicted in other potentials and phase shift analyses. Some of the coupling constants obtained are also larger than the others [44]. Because of the use of the narrow $\Delta$ approximation a direct comparison of the model with high energy experiments is very difficult.

Recently the Bonn group has extended their potential above the pion production threshold [45,46,47] by explicitly including the nucleon and delta-isobar self energy diagrams which in turn guarantees the unitarity above threshold. Except for the $^1P_1$ phase shift in the I=0 channel, the present model can describe the phases fairly well. Below the threshold, their new calculation, by a slight readjustment of the meson parameters, reproduces part of the nucleon-nucleon data well.

# Chapter 2

# The Experiment

The goal of the present TRIUMF experiment was to measure the spin correlation parameter, $A_{yy}$, in n-p elastic scattering at intermediate energies over a wide angle range of $50^0 - 150^0$ in the center of mass with an absolute accuracy of $\pm 0.03$.

The experiment involved scattering vertically (normal to the scattering plane) polarized neutrons from vertically polarized protons and then measuring the left-right yields for all four combinations of beam (neutrons) and target (protons) polarization states. The layout of the experiment is shown in fig 2.1. The details of the beam transport system can be found in refs [48][49]. The polarizations and energies of the vertically polarized primary protons coming out of the cyclotron were measured in the proton beam polarimeters and beam energy monitor (sec. 2.1). Neutrons were produced in the liquid deuterium ($LD_2$) target via the $^2H(\vec{p},\vec{n})2p$ reaction. The transverse polarization transfer coefficient $(r_t)$[1] attains a maximum at $9^0$(lab), which is the

[1]The transfer coefficient for free n-p scattering is denoted as $R_t$. However, for the reaction $^2H(\vec{p},\vec{n})2p$ the same transfer coefficient is denoted as $r_t$. The difference between the two is a small correction factor of the order of 0.04 at intermediate energies.

extraction port for neutrons in beam line 4A/2 at TRIUMF [50]. In order to take advantage of this large value of $r_t$, the polarization direction of the primary proton beam was rotated clockwise in the horizontal plane by the spin precession solenoid 'JANIS'(L) with longitudinal magnetic field. After passing through the $LD_2$ target the primary proton beam was transported to a beam dump using a dipole magnet (4AB2) with a $35^0$ bend angle. The polarized neutron beam was defined by a 3.37 m long collimator with steel inserts in a steel box filled with lead. The beam then passed through two spin precession dipole magnets, 'CLYDE'(V) with magnetic field pointing up and 'BONNIE'(H) with field pointing left when viewed along the beam direction (sec. 2.2). The dipole magnet, 'CLYDE', along with the effect of 4AB2 rotated the neutron spins to lie along the beam direction and then the dipole magnet, 'BONNIE', rotated the spins by $90^0$ into the vertical plane. Note that these two dipoles also helped to remove charged particles from the neutron beam. Neutrons then impinged on a frozen spin type polarized proton target (sec 2.3). Recoil protons were detected in two symmetrically placed multi wire proportional chamber (MWPC) systems with delay line readouts and proton time-of-flight assemblies (sec. 2.5). Scattered neutrons were detected in coincidence in two 1.05 m x 1.05 m x 0.30 m scintillator arrays giving information on neutron angle and time-of-flight (sec. 2.6). The position of the neutron beam centroid on the target was continually monitored by the neutron beam profile monitor (sec. 2.4) placed 4 m downstream of the target.

In order to know the target polarization to an absolute accuracy of $\pm 2\%$ an independent calibration of the target polarization was made at the beginning and end of each of two data taking runs. For this, 469 MeV unpolarized ($\vec{P}_n = 0$) protons were scattered off the frozen spin target at the angle where

the p-p analyzing power is very precisely known (Appendix A). The measured asymmetry allowed an extraction of the target polarization to the accuracy mentioned above and to determine a value of $r_t$ by comparison of analyzing powers obtained from the beam and target polarizations.

## 2.1 Proton Polarimeter and Beam Energy Monitor

During the course of the experiment the polarizations of the primary protons were continually monitored in two polarimeters. The first polarimeter (referred to as the In Beam Polarimeter or IBP) is a four branch polarimeter capable of measuring both transverse components (horizontal and vertical) of polarization of the proton beam. This polarimeter has large acceptance (2.8 msr) and contains a hydrogenous target foil located 7.21 m upstream of the $LD_2$ target. The second polarimeter (hereafter referred to as the CSB polarimeter) has a much smaller acceptance (0.16 msr) and is a two branch polarimeter measuring only the vertical component of the polarization. This polarimeter is also equipped with a beam energy monitor (BEM) assembly consisting of scintillator stacks and copper plates to measure the relative energy of the incident beam. The principle of operation was the same for both polarimeters. The proton beam polarizations were measured by scattering the beam off a Kapton foil ($CH_2$ foil in the IBP) and then measuring the left-right (and also up-down in case of the IBP) scattering asymmetry at $17^0$ on both sides of the incident proton beam. Only the second (CSB) polarimeter will be described here. Design details for the IBP polarimeter can be found in ref.[51].

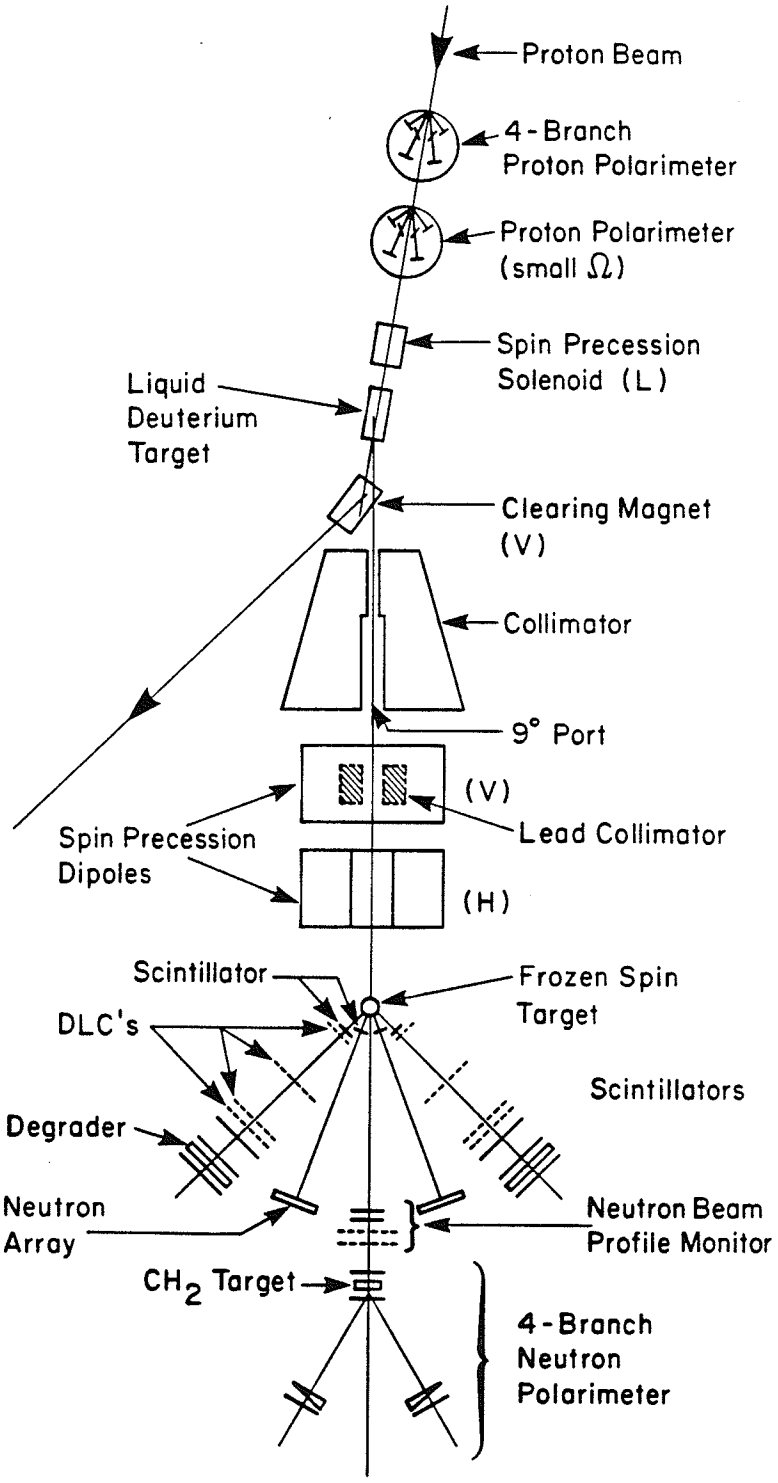


Figure 2.1: Experimental lay out

Table 2.1: CSB Proton polarimeter specifications

| | |
|---|---|
| **Solid Angle Defining Counter** | |
| Vertical dimension | 1.0 cm |
| Horizontal dimension | 2.5 cm |
| Distance to target | 77.47 cm |
| Solid angle | 0.16 msr |
| Polar angle range | $\pm 0.37^0$ |
| Azimuthal angle range | $\pm 1.26^0$ |
| Central angle | $17^0$ |
| Rotation angle | $68^0$ |
| | |
| **Recoil Counter** | |
| Vertical dimension | 2.0 cm |
| Horizontal dimension | 1.0 cm |
| Distance to target | 20.32 cm |
| Solid angle | 4.84 msr |
| Polar angle range | $\pm 1.41^0$ |
| Azimuthal angle range | $\pm 3.0^0$ |
| Central angle | $68.9^0$ |

The CSB polarimeter is placed in a 1.5 m diameter scattering chamber (SFU chamber) located 5.8 m upstream of the $LD_2$ target. The layout of the polarimeter and beam energy monitor is shown in fig 2.2 and the detailed design criteria are summarized in table 2.1 [52]. The polarimeter consists of two sets of detector assemblies placed symmetrically around the incident beam. The forward arm ($\pm 17^0$) consists of two scintillators followed by a large Cu degrader and a stack of six 10 mm thick scintillators with 1 mm Cu sheets sandwiched in between. In order to reduce backgrounds from various sources the recoil protons are detected in coincidence in two additional scintillators (one in each branch) placed at $\pm 68.9^0$ (lab). The polarimeter is made insensitive to beam movement by rotating the solid angle defining counter ($A_2$ in fig. 2.3) by $68^0$ with respect to the scattered beam direction [52]. For each angle setting of the neutron array, the Kapton foil in the polarimeter was replaced by $CH_2$ and graphite foils, each for at least one complete spin cycle (i.e. for about 7-8 minutes). This was done in order to monitor continuous hydrogen loss in the Kapton foil, for quasi-free $(p, 2p)$ background from the carbon in the Kapton foil. The target foils are mounted on a remotely controlled target ladder. Note that this polarimeter was initially designed for the 500 MeV charge symmetry breaking experiment[53]. In order to use the polarimeter at other energies the target foil has to be given appropriate displacements from its nominal 500 MeV position to compensate for the change in coincident p-p kinematics with energy. In table 2.2, all the offsets used in the experiment are summarized.

Fig 2.3 shows the beam energy monitor assembly in greater detail. The degrader thickness was changed with primary beam energy. Column 3 in table 2.2 gives the degrader thicknesses that were used during the experiment. For 235 MeV incident proton beam energy the Cu spacers between

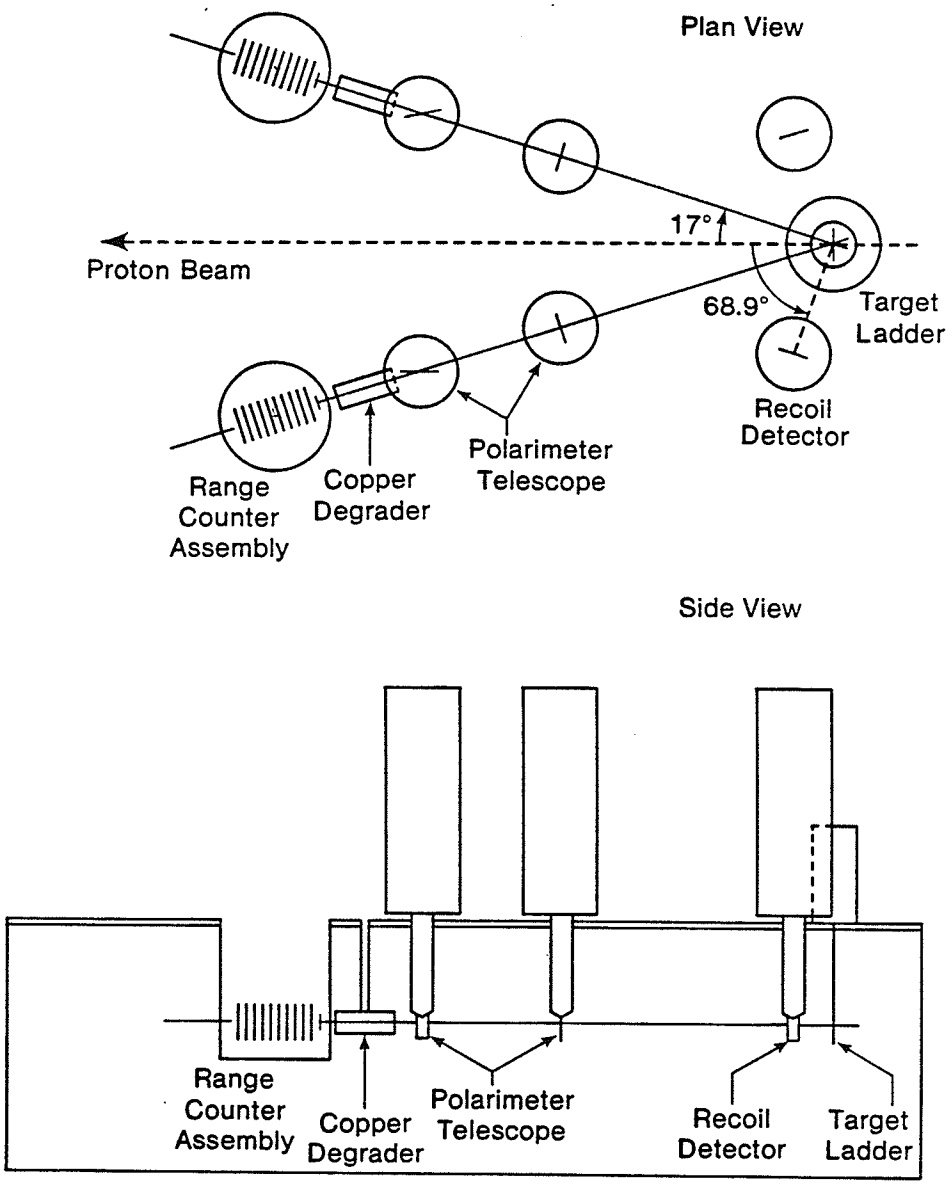


Figure 2.2: Schematic diagram of proton polarimeter

Table 2.2: Polarimeter target offsets and degrader thickness

| Incident Energy (MeV) | Offsets (cm) | Degrader thickness (cm) |
|---|---|---|
| 445 | 0.9 | 11.86 |
| 343 | 1.2 | 7.37 |
| 235 | 1.5 | 3.74 |

the scintillators were removed. The average energy of the incident proton beam was measured by knowing the number of stopping protons in each of the six scintillators.

## 2.2 Neutron Beam Production and Transport

Polarized neutrons were produced in the $LD_2$ target via the quasi-elastic reaction $D(\vec{p},\vec{n})2p$. The $LD_2$ target is 197 mm long and 51 mm in diameter. Target walls were made of 0.25 mm thick stainless steel with 0.051 mm thick stainless steel end windows. The target was designed to operate with either liquid deuterium or liquid hydrogen. The target cell was remotely moved into and out of the beam and could be replaced by a geometrically and materially equivalent dummy target. The experiment was done at three incident proton beam energies, 235, 343, and 445 MeV. Allowing for energy loss in the $LD_2$ target, one gets the proton energies at the center of the target as, 227.8, 337.2 and 440.0 MeV respectively. After correcting for the binding energy of deuteron and the energy carried away by the recoil proton, the mean energies of neutrons scattered at $9^0$ (lab) are, $219.6 \pm 2.0$, $324.8 \pm 2.0$ $424.7 \pm 2.0$ MeV. The neutron spectrum at 425 MeV as calculated by Bugg and Wilkin [54,55] is shown in fig 2.4. The absolute energy spread varies from 11 MeV

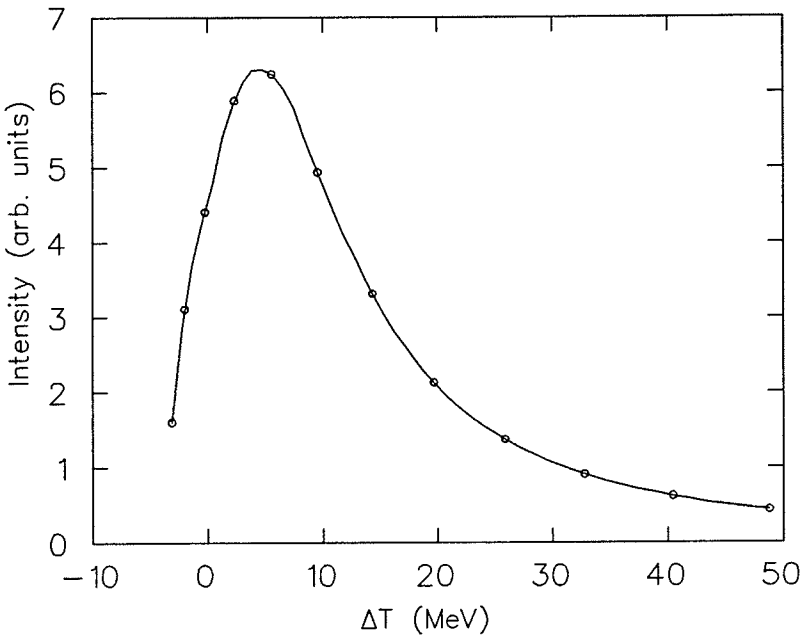


Figure 2.3: Energy spectrum of 425 MeV neutrons scattered at $9^0$ as calculated by Bugg and Wilkin [54]. Note that $\Delta T$ is the difference in neutron energy between reactions on hydrogen and deuterium targets.

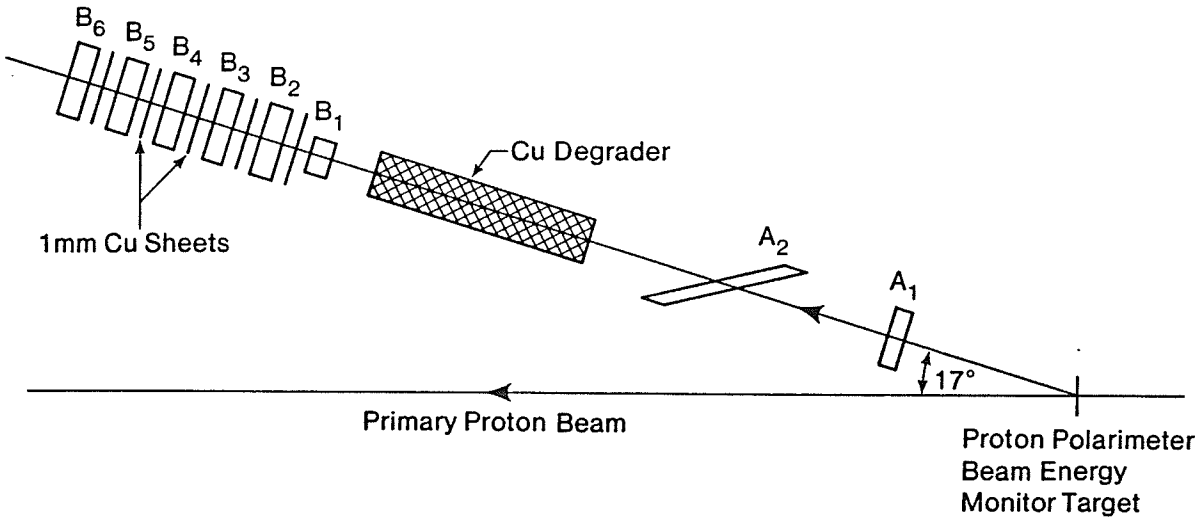


Figure 2.4: One of the two arms of the beam energy monitor assembly.

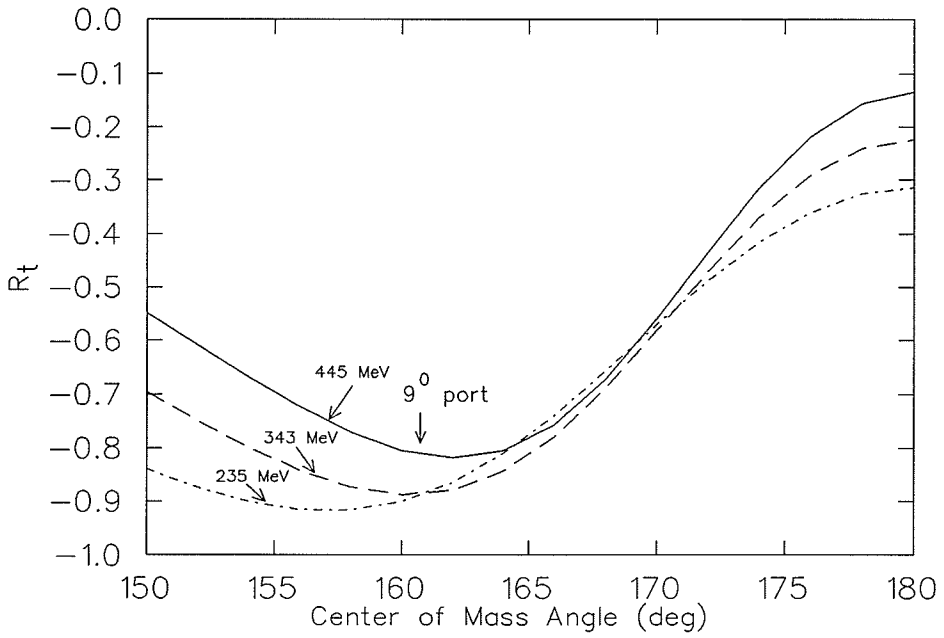


Figure 2.5: Variation of $R_t$ with angle and energy

at 220 MeV to 15 MeV at 425 MeV. The uncertainty in the neutron beam energy ($\pm$2.0 MeV) is the expected maximum uncertainty as measured in another experiment [56].

The sideways to sideways spin transfer coefficient, $r_t$, is used to obtain the maximum neutron polarization. This is because the parameter, $r_t$ has a large negative value around $9^0$ ($\sim 162^0$ in c.m.) over the TRIUMF energy range. Fig 2.5 shows the angular distribution [13] of the same transfer coefficient for free n-p scattering ($R_t$) at three incident energies. Note that since the neutron production is a quasi-elastic process but not a free charge exchange reaction the polarization transfer coefficient $R_t$ is to be corrected for final state interactions [54].

The primary protons were vertically polarized whereas the parameter $r_t$ involves polarization transfer in the horizontal plane. This required the

Table 2.3: Janis solenoid current

| Incident Energy (MeV) | $\int Bdl$ (T.m) | Solenoid current (A) |
|---|---|---|
| 445 | 1.907 | -76.7 |
| 343 | 1.637 | -65.8 |
| 235 | 1.328 | -53.4 |

proton polarization to be rotated by $90^0$ into the horizontal plane before the beam hit the $LD_2$ target. This is done by a spin precession solenoid 'JANIS' placed 1.8 m upstream of the $LD_2$ target. The $\int Bdl$ required to rotate the proton spin by $90^0$ depends on the beam energy and is determined from :

$$\int Bdl = \frac{\pi \hbar c(pc)}{2mc^2 g \mu_p} \tag{2.1}$$

where $g = 2, \mu_p = 2.793\ nm = 8.8 \times 10^{-14}\ MeV/Tesla,\ \hbar c = 197.3 \times 10^{-15}\ MeVm,\ mc^2 = 938.3\ MeV$ . This gives :

$$\int Bdl = 1.877 \times 10^{-3}(pc)\ \ Tesla\ m \tag{2.2}$$

Currents required to produce the necessary $\int Bdl$ for the three incident beam energies are tabulated in the table 2.3. The solenoid gives the polarization a clockwise rotation into the horizontal plane. The neutrons produced in the $LD_2$ target attain a net polarization ($P_n$) in the horizontal plane given by :

$$P_n = \sqrt{r_t^2 + r_t'^2}\ \ P_p \tag{2.3}$$

where $P_p$ is the proton polarization as measured by the proton polarimeter and $r_t'$ is defined in the previous chapter as the sideways to longitudinal spin transfer coefficient. The parameter $r_t$ is negative, so the polarization direction of the neutrons is opposite to that of the protons. Because of

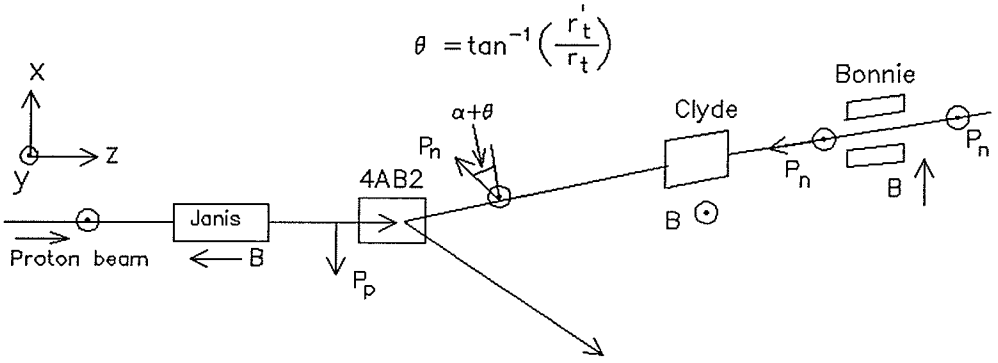


Figure 2.6: Neutron polarization transfer and precession through various magnets.

the non-zero value of $r'_t$ the polarization direction of the neutrons was not exactly transverse to the beam direction, instead it made a small but finite angle $\theta = tan^{-1}r'_t/r_t$ (fig 2.6). The fringe field of the bending magnet that swept the primary proton beam away from the neutron beam also rotated the neutron spin by an extra angle $\alpha$. The neutrons produced at $9^0$ were brought down through a 3.37 m long collimator consisting of steel pipes welded to a steel, lead filled, frame with steel inserts. The pipes were built in two sections, the downstream section was 1.5 m long and 128 mm in diameter while the upstream section was 1.87 m long and 102 mm in diameter. Eleven steel inserts filling the $9^0$ port had rectangular apertures varying in size from 39.1 mm horizontal by 18.6 mm vertical upstream to 46.1 mm horizontal by 32.3 mm vertical downstream respectively. The front face of the collimator is 2.87 m downstream of the center of the $LD_2$ target.

As is evident from fig 2.5, on exit from the collimator the neutron's spin is lying in the horizontal plane (also the scattering plane) with the spin direction making an angle $\theta + \alpha$ with the transverse direction. The measurement of $A_{yy}$ requires that the neutron spin direction be oriented normal to the scattering plane. This requires two dipole magnets or a dipole magnet and a superconducting solenoid. In the present set up the combination of two dipole magnets was chosen. The first dipole called 'CLYDE', has field pointing up (vertical). The $\int Bdl$ required to precess the neutron spin by an angle,$\theta_n$, is :

$$\int Bdl = \frac{p_n(MeV/c)\,\theta_n(deg)}{32.856\,\gamma} \quad kG.cm \tag{2.4}$$

where $\gamma = (1 - v^2/c^2)^{-1/2}$. A longitudinally polarized neutron beam with its polarization direction pointing backwards (forwards) is obtained with the primary proton spin pointing 'up' ('down'), solenoid polarity 'negative' (i.e. field along negative z, opposite to the direction of motion of the incident beam) and the field in 'CLYDE' vertical (along y). Since the neutron polarization is already rotated by the angle $\theta + \alpha$ the net precession required to put the polarization direction along the beam direction is $(90^0 - \theta - \alpha)$. The magnet currents required are obtained from the measured excitation curves of the magnets. The dipole magnet 'CLYDE' has a second collimator between the pole faces. The collimator, which is 0.61 m long and 51.3 mm by 50.8 mm in aperture, is made up of stacked lead bricks. This helps to reduce the neutron flux scattered from the walls of the first collimator. This magnet also removes the charged particles from the neutron beam.

The second dipole magnet , 'BONNIE', has horizontal field pointing left (when viewed along the beam direction). This magnet rotates the longitudinal neutron spin by $90^0$ and thus brings it perpendicular to the scattering plane. Note that the neutrons produced in the $LD_2$ target acquire a small

Table 2.4: Dipole currents

| Primary proton energy (MeV) | Neutron energy (MeV) | CLYDE | | BONNIE | |
|---|---|---|---|---|---|
| | | B (T) | Current (A) | B (T) | current (A) |
| 445 | 424.7±2.0 | 0.981 | 1103 | 1.542 | 793 |
| 343 | 324.8±2.0 | 0.947 | 1067 | 1.394 | 668 |
| 235 | 219.6±2.0 | 8.35 | 0.936 | 1.202 | 543 |

but finite vertical spin component because of the polarization, P ($\simeq$ 0.06). This normal component of the spin is rotated into the longitudinal direction by the second magnet, 'BONNIE'. Since in the experiment the target polarization was vertical this longitudinal component of the neutron spin does not contribute to the left-right asymmetry due to parity conservation.

The magnetic field in 'CLYDE' was calibrated by finding the zero crossing of the up-down vertical asymmetries in the neutron polarimeter. For calibrating 'BONNIE', the superconducting solenoid 'JANIS' was turned off so that the neutron polarization after the $LD_2$ target was vertical (because of the transfer coefficient $D_t$) and the dipole magnet 'CLYDE' was set at the nominal value. The correct field setting was found by looking at the zero crossing of left-right asymmetries in the same polarimeter. The details of the technique can be found in ref. [48]. The currents for these two dipole magnets for the three energies are summarized in table 2.4. During the experiment both magnet fields were continually monitored using NMR probes.

Table 2.5: Frozen Spin Target Specifications

| | |
|---|---|
| Maximum Polarization | up: 0.81 |
| | down: 0.84 |
| Relaxation time | $\geq$ 500 hours |
| Magnetic holding field | 0.26 T |
| Holding field reproducibility | $\pm 0.1\%$ |
| Holding field Stability | $\pm 0.1\%$ at target center |
| Target volume | 35 $cm^3$ 5 cm high,2 cm thick, 3.5 cm wide |
| Opening angle | Horizontal $\pm 93^0$ |
| | Vertical $\pm 11^0$ |

## 2.3 Frozen Spin Polarized Proton Target

A frozen spin polarized proton target [57] , placed 12.9 m downstream of the $LD_2$ target, was used in this experiment. Table 2.5 summarizes the target specifications. This type of target needs a lower magnetic holding field to maintain the polarization compared to other types of targets. The target material was 1.5 mm diameter butanol ($C_4H_{10}O$) beads immersed in a bath of 94% $^4He$ and 6% $^3He$. Details of the target design and principle of operation can be found in ref [58]. Polarization of the target took place in a 2.57 T magnetic field of a superconducting solenoid. Once the desired polarization was obtained the target temperature was lowered to about 40 mK to "freeze" the polarization. The solenoid was lowered and a conventional magnet above the target cell was energized to supply together with the superconducting solenoid the 0.26 T holding field. The whole operation took about 6-7 hours.

The polarization of the target material is based on the principle of dynamic nuclear polarization (DNP)[59]. The target material, which is usually an organic substance, is doped with a small concentration of electron donor

material of complex molecules containing the chromium atom. In this way the density of free electrons in the target material is increased. In the presence of an external magnetic field (2.5 T) and at low enough temperature (1 K) the electron spins are aligned antiparallel to the magnetic field. The proton spins, because of their very small magnetic moment (600 times smaller than that of an electron), remain unaffected. The transition between the electron-proton states is induced by irradiating the target material with microwaves. The frequency of microwaves is chosen in such a way that an electron and a proton flip their spins at the same time. The electron being strongly coupled to the lattice flips back to its thermal equilibrium value very quickly. But the proton relaxation time is very large and thus the proton stays in the polarized state for a much longer time. The mechanism can be better understood if one draws the appropriate energy levels. In the magnetic field the four fold degeneracy of the electron-proton states $|e,p>$ is removed (fig 2.7). Because of the dipole-dipole interaction the four states are not pure but contain an admixture of other states. For convenience it is assumed that the states are pure. The states $|c>$ and $|d>$ are almost equally populated while the states $|a>$ and $|b>$ are almost empty. The transition between different states can be forced to occur by applying radiation of the appropriate frequency. For example, if one applies an energy of the order of $\hbar(\omega_e+\omega_n)$, transition between states $|d>$ and $|a>$ is possible, and the electron and proton spins flip simultaneously in the same direction ('flip-flip') , from a 'down' state to an 'up' state. The probability of spontaneous transition between states$|a>$ and $|c>$ or between states $|b>$ and $|d>$ is very large compared to that between states $|a>$ and $|d>$ or between states $|b>$ and $|c>$. Because of the spin-phonon interactions a quick transition takes place between states $|a>$ and $|c>$. The rate for this process is about

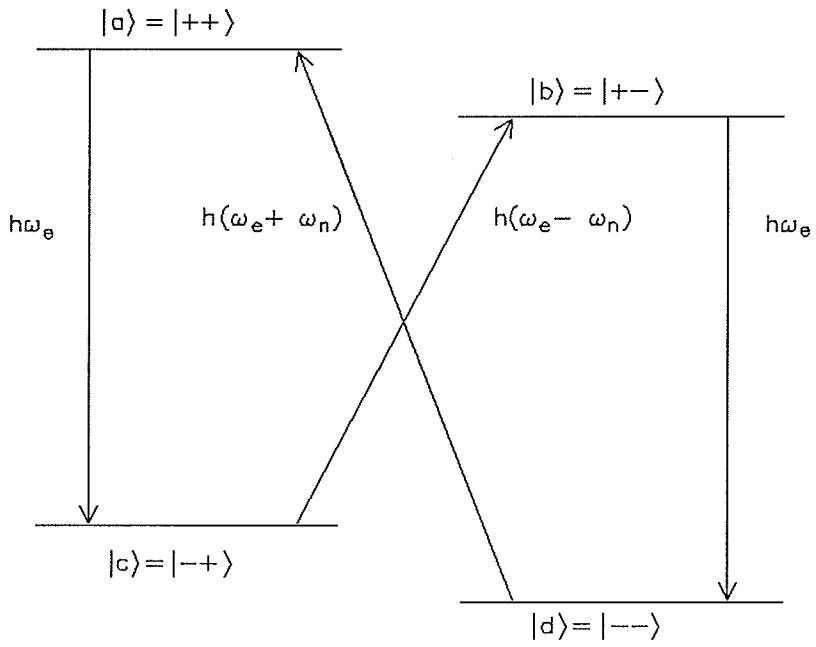


Figure 2.7: Energy levels for electron-proton system in presence of a magnetic field.

$10^3\ s^{-1}$, whereas the rate for transition from state $|a>$ to state $|d>$ is very small, of the order of $10^{-3}\ s^{-1}$. After a certain time, the electron frees itself from the state $|c>$ leaving the proton in a spin state opposite to that in which it started. This free electron then couples with another proton and induces a further transition. Now if one wants to have the target polarized in the 'down' state all one has to do is to apply microwaves with frequency equal to the transition frequency $(\omega_e - \omega_n)$ between states $|c>$ and $|b>$. As is evident from the figure, in this transition, the electron and proton spins reverse simultaneously in the opposite direction ('flip-flop'). The polarization decay time is related to the temperature and holding field through the following empirical expression [57].

$$\tau = \eta\ H^2 T^{-4} \tag{2.5}$$

The constant $\eta$ is inversely proportional to the doping concentration of free electrons. Thus to increase this decay time a compromise must be made between the strength of the holding field (H) and the target temperature (T).

Fig 2.8 shows a schematic diagram of the frozen spin target (FST) used in the experiment. The maximum target polarization obtained during the experiment was 84% with a typical decay time of 600 hours. The target holding field was measured in the beam plane, and in planes 5 cm above and 3 cm below the beam plane. Fig 2.9 shows a plot of the target holding field in the beam plane. The field at the center of the target is 0.257 T but it drops off very rapidly to almost zero. The target cell was rectangular in shape, 2 cm thick, 3.5 cm wide and 5 cm high. The position of the target cell and the volume occupied by the butanol beads in the cell were determined from X-ray radiographs taken at the beginning and end of the two data taking runs. During the experiment we had two orientations of the target cell. In

phase-1 of the experiment which was carried out at the forward proton angles ($20^0 - 45^0$ in lab) the target cell was oriented with its 2 cm side along the beam. For the phase-2 of the experiment, at the backward proton angles, the target cell was rotated by $90^0$ so that the 3.5 cm side was parallel to the beam. This was done to reduce the multiple scattering of the recoil protons.

The polarization of the target was measured by the usual NMR technique. Polarizations were calibrated against the thermal equilibrium values in the polarizing field at 1 K. Polarization measurements were made once in every twenty four hours. For each angle setting and for each energy there were two orientations of the target spin, 'up' (+y) and 'down' (-y). The average polarization for each spin state of the target is determined, assuming an exponential decay of the polarization as,

$$\bar{P}_{NMR} = \frac{P_i - P_f}{ln(P_i/P_f)}$$

where $P_i$ and $P_f$ are intial and final polarizations at the beginning and end of each angle run. The average polarizations of the target as measured by the NMR are summarized in table-2.6. The NMR values of polarization were accurate to within 4% [60]. In order to know the absolute target polarizations to better than 4% separate calibration data were taken with 497 and 512 MeV primary protons. The details of the calibration part are described in the Appendix-A.

## 2.4 Neutron Beam Profile Monitor and Polarimeter

During the course of the experiment the position of the neutron beam on the frozen spin target was continuously monitored. The proton beam posi-

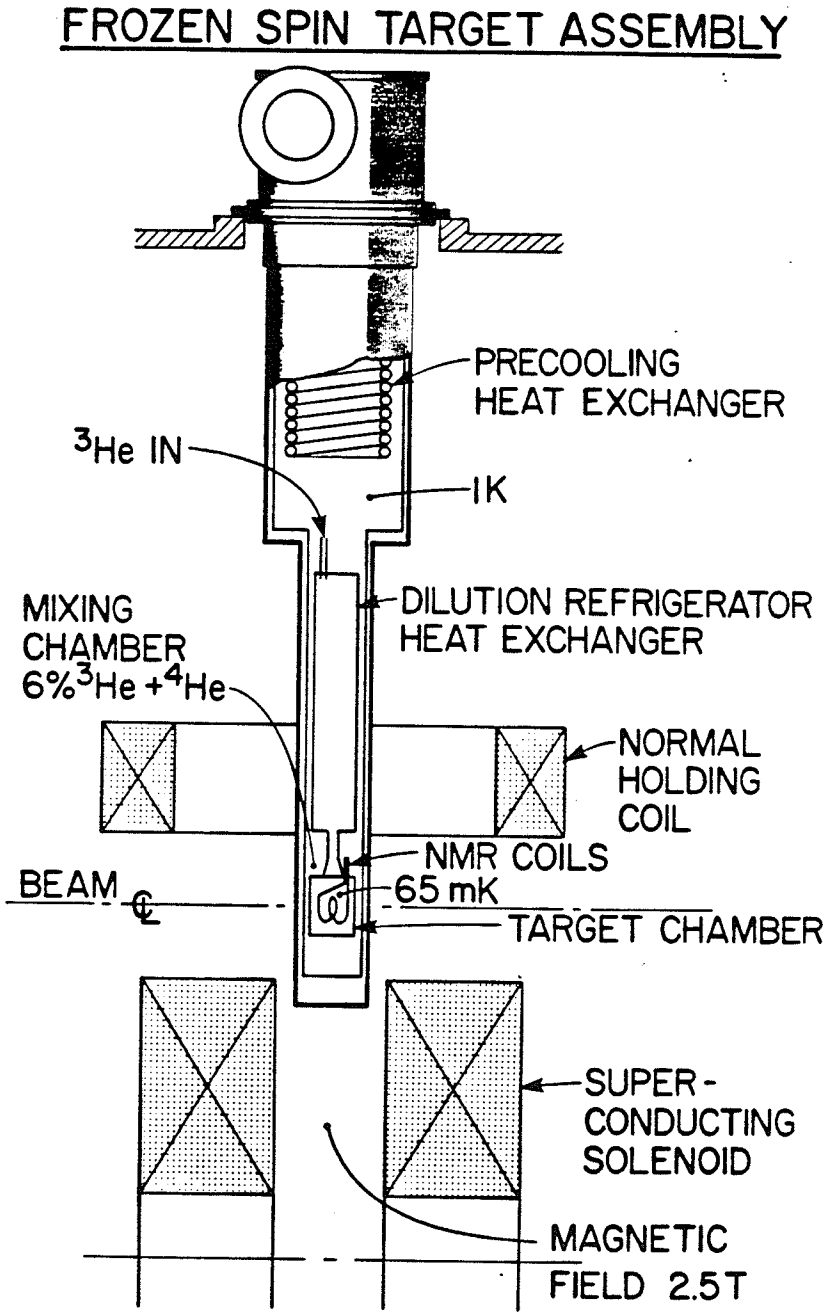


Figure 2.8: Schematic diagram of frozen spin target

Table 2.6: NMR values of magnitude of target polarization

| Neutron beam energy (MeV) | Neutron array angle (deg) | Target Polarization | | |
|---|---|---|---|---|
| | | spin up | spin down | average values |
| 424.7±2.0 | 67.0 | 0.735 | 0.719 | 0.727 |
| | 61.0 | 0.743 | 0.735 | 0.739 |
| | 57.0 | 0.761 | 0.712 | 0.737 |
| | 52.0 | 0.774 | 0.701 | 0.737 |
| | 47.0* | 0.791 | 0.684 | 0.738 |
| | 47.0# | 0.775 | 0.809 | 0.792 |
| | 37.0 | 0.778 | 0.794 | 0.786 |
| | 27.0 | 0.789 | 0.787 | 0.788 |
| 324.8±2.0 | 67.0 | 0.721 | 0.756 | 0.740 |
| | 61.0 | 0.716 | 0.759 | 0.737 |
| | 57.0 | 0.707 | 0.768 | 0.738 |
| | 52.0 | 0.694 | 0.780 | 0.737 |
| | 47.0 | 0.682 | 0.787 | 0.734 |
| | 42.0 | 0.803 | 0.773 | 0.788 |
| | 37.0 | 0.812 | 0.745 | 0.779 |
| | 32.0 | 0.820 | 0.712 | 0.766 |
| 219.6±2.0 | 67.0 | 0.748 | 0.736 | 0.742 |
| | 61.0 | 0.741 | 0.728 | 0.734 |
| | 57.0 | 0.763 | 0.710 | 0.737 |
| | 52.0 | 0.775 | 0.696 | 0.736 |
| | 47.0 | 0.784 | 0.773 | 0.778 |
| | 37.0 | 0.764 | 0.757 | 0.761 |

* March '87 run, # June '87 run

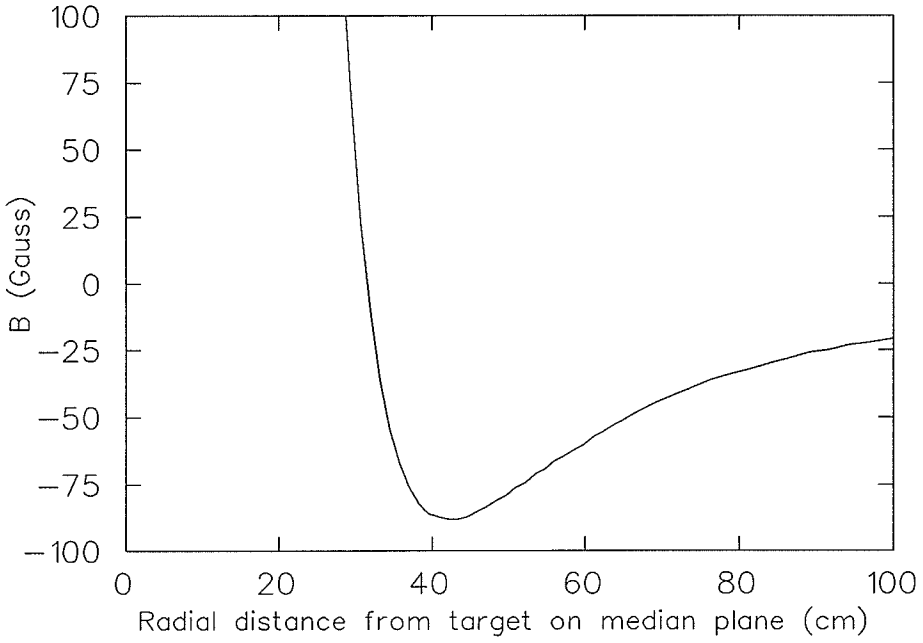


Figure 2.9: Radial component of the holding field of frozen spin target

tion just upstream of the $LD_2$ target was determined from in-beam monitors during beam tuning. However, because of the large distances (12.9 m) involved, precise positioning of the neutron beam on the target couldn't be determined solely from the primary proton beam position. One also wants to make sure that the neutron beam centroid does not change position correlated with the target spin reversal. The neutron beam profile monitor is stationed 4 m downstream from the target (FST). A schematic diagram of the profile monitor and the polarimeter is shown in fig 2.10. In the figure the neutron beam is coming from the right, charged particles in the beam are removed by the veto counter (VC). The converter scintillator (C), 21.0 cm by 21.0 cm by 3.2 mm in size, is used to produce charged particles through n-p elastic scattering. These charged particles are traced back to the converter scintillator by two 20.3 cm by 20.3 cm delay line wire chambers (DLCs)

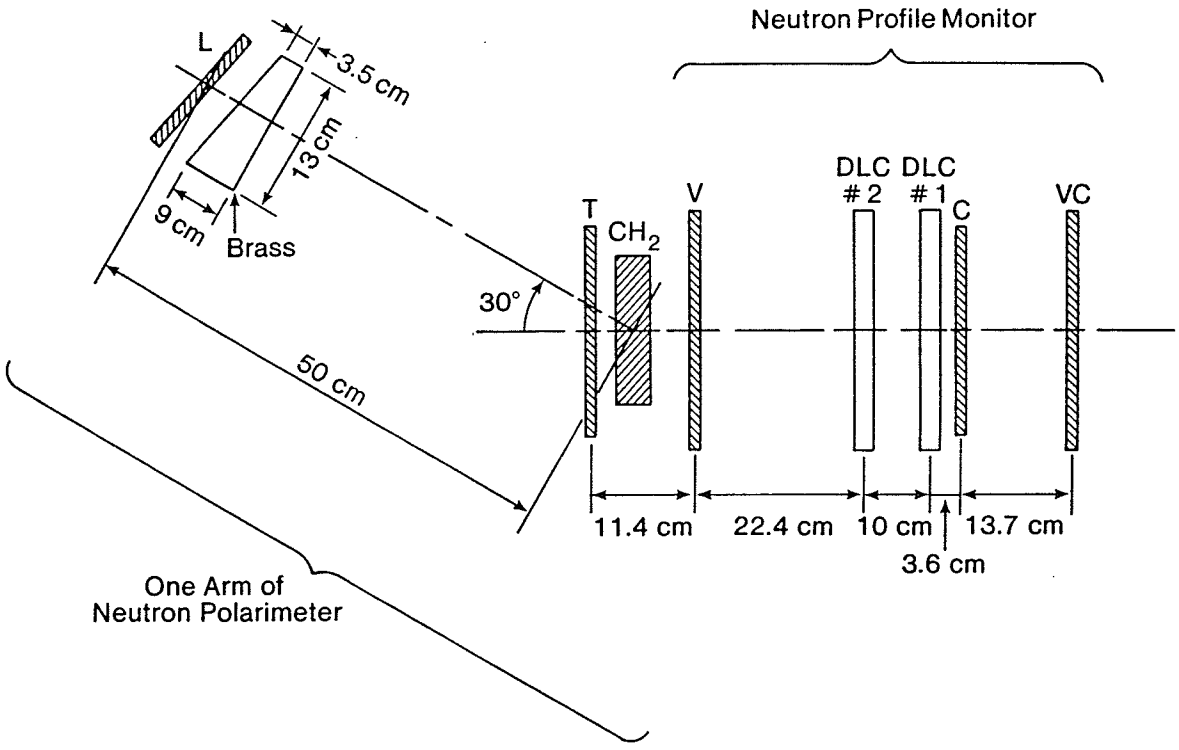


Figure 2.10: Neutron beam profile monitor and polarimeter assembly

giving the vertical and horizontal beam profiles.

The neutron polarimeter is mainly used to measure the horizontal and vertical asymmetries which are then compared with the values obtained from the proton polarimeters. Since the effective analyzing powers for this polarimeter are not well known, a direct determination of the neutron beam polarization is not possible. The polarimeter is located just downstream of the profile monitor (fig 2.9) and consists of a 5 cm thick polyethylene ($CH_2$) target with a 3.2 mm thick veto scintillator in front of the target. Following the target is a 3.2 mm thick scintillator (T). Protons from n-p reactions in the $CH_2$ target and the scintillator T are detected in the four identical 6.4 mm thick scintillators forming two pairs of branches, left-right and up-down. Each scintillator is 10 cm by 10 cm in size and is at 50 cm from the $CH_2$ target and covers a solid angle of 0.040 sr. Wedge shaped brass absorbers are placed in front of each of four scintillators to remove the energy dispersion in the scattered protons and to remove lower energy charged particles.

## 2.5 Proton Detection System

As mentioned before, recoil protons were detected in two detector assemblies mounted on booms symmetrically placed around the incident neutron beam direction. The layout of the detection apparatus is shown in fig 2.11. Each boom supported a time-of-flight system for energy determination and a set of four delay line chambers (DLC) for track reconstruction and hence measurement of the scattering angle.

The proton time-of-flight system consisted of a 0.8 mm thick start scintillator (PTOF) and a 6.4 mm thick stop scintillator called the E-counter. The start scintillator was placed 40 cm away from the frozen spin target

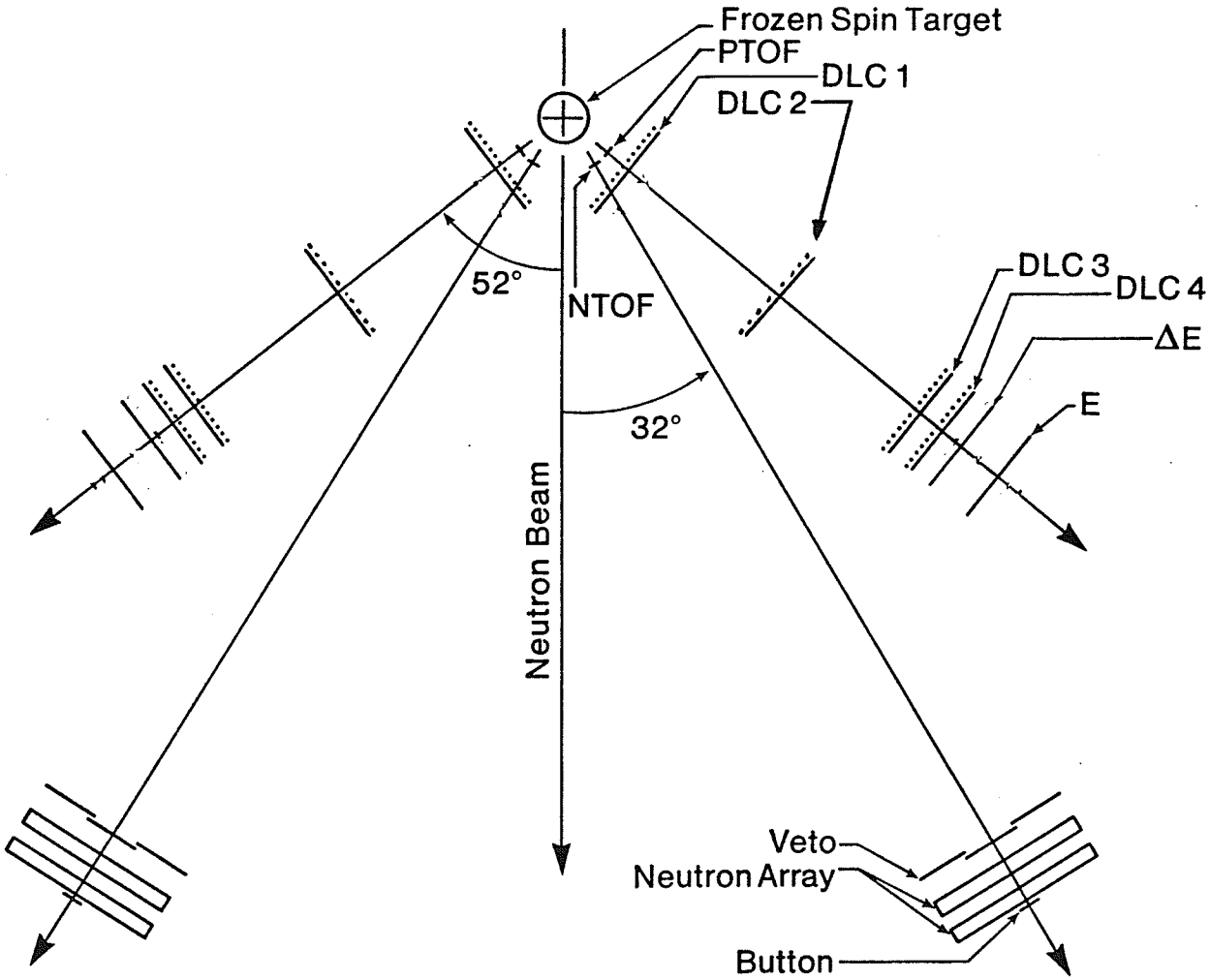


Figure 2.11: Schematic diagram for proton and neutron detection assemblies

Table 2.7: Distances of proton boom elements

| Device | Left (mm)[a] | Right (mm)[a] | Thickness (mm) | Dimensions (cm) | |
|---|---|---|---|---|---|
| | | | | Horizontal | Vertical |
| PTOF | 400 | 395 | 0.8 | 17.5 | 17.5 |
| DLC1 | 609.4 | 618.4 | [b] | 30.0 | 30.0 |
| DLC2 | 1671.3 | 1669.3 | [b] | 58.0 | 58.0 |
| DLC3 | 2828.1 | 2831.9 | [b] | 58.0 | 58.0 |
| DLC4 | 2992.7 | 2999.5 | [b] | 58.0 | 58.0 |
| $\Delta E$ | 3137 | 3139 | 6.4 | 67.0 | 67.0 |
| E | 3444 | 3444 | 6.4 | 67.0 | 67.0 |

(a) Left and right are with respect to the incident neutron beam. (b) Thickness is $\sim 25\ mg/cm^2\ Al$ equivalent

(FST) center and was viewed by phototubes at opposite ends; the timing signal for each tube as well as their hardware mean time were available . The E-counter was a 67 cm by 67 cm scintillator located 3.4 m away from the target. There were four phototubes attached to this scintillator, two on each of top and bottom ends. The timing signals from all of these four tubes were collected during the experiment. There was another scintillator on each boom, a 6.4 mm thick $\Delta E$ counter placed 31 cm upstream of the E-counter. The positions of different boom elements are summarized in table 2.7. All distances were measured from the target center.

The delay line chamber (DLC1) closest to the FST on each boom had an active area of 30 cm by 30 cm. The operating voltage for this chamber was 3600 V. The three subsequent chambers (DLC2, DLC3 and DLC4) on the boom were considerably bigger in size, each with an active area of 58 cm by 58 cm, the corresponding voltages were between 4450 and 4550 V. All these chambers consisted of single anode planes sandwiched between cathode foils which were made of 20 $\mu m$ copper strips on 25 $\mu m$ mylar, the copper strips

being 3.5 mm wide with 0.5 mm gap in between. The separation between the anode plane and each cathode plane is 4.8 mm for the first chamber and 6.0 mm for the three subsequent chambers. This spacing is kept constant by flowing the chamber gas under pressure, enough to counter-balance the electrostatic attraction between the cathode and anode planes. The various materials that a particle traverses while passing through each chamber are listed in table 2.8. Each chamber had two delay lines, each with a capacitive input near both ends for pulser signal injection . The delay lines are solenoidal type [61] with propagation speed approximately equal to 28 ns/cm. Each end of each delay line has a 5.0 cm x 7.5 cm discriminator board mounted on it. 'Magic gas' consisting of 30% isobutane, 30% a mixture of 1% freon in argon and 40% argon bubbled through methylal was flowed at 100 cc/min through each chamber. The delay lines of the back chambers were calibrated by placing each group of four chambers as close together and as far from the target as possible thus allowing for full illumination of the chambers. The horizontal time difference spectra showed the 'picket fence' image of the anode wires (fig 2.12). The delay line linearity was calibrated by making use of this 'picket fence' spectrum. A calibration table relating the horizontal delay time with absolute anode wire positions was constructed. The calibration table for the vertical coordinate was formed in the following way. First, two out of four chambers were rotated by $90^0$ so that the 'picket fence' coordinate in these two chambers is in the vertical direction. By ray tracing through the chambers, the vertical coordinates of the unrotated chambers were calibrated with respect to the already calibrated picket fence coordinate. The delay lines on the first chamber of each boom is assumed linear and no calibration table for this chamber was constructed. The horizontal position resolution was $\pm 0.6\ mm$ whereas the vertical resolution

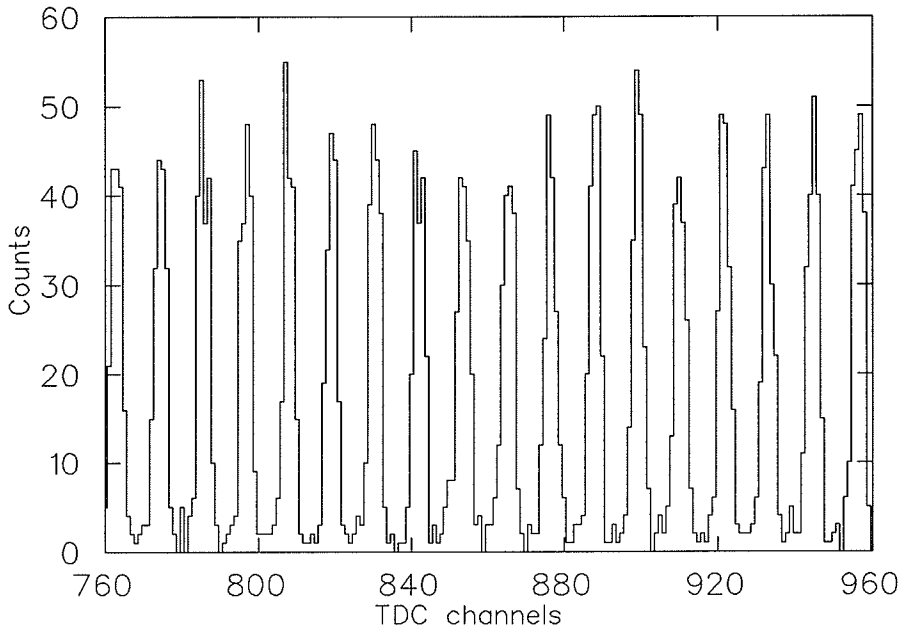


Figure 2.12: 'Picket fence' image of anode wires in DLC2

was about $\pm 0.4\ mm$, somewhat better compared to the horizontal resolution because of absence of any picket fence structure in the vertical direction.

The kinematic acceptance for coincident neutron-proton pairs was determined by the fourth delay line chamber furthest from the FST. If this chamber does not fire then the solid angle is defined by the third chamber.

## 2.6 Neutron Detection System

Scattered neutrons were detected in two large 1.05 m wide, 1.05 m high and 0.30 m thick identical scintillator arrays placed at angles conjugate to the elastic proton angles. Fig 2.13 shows a schematic diagram of one of the arrays. Each array was made of two vertical banks of seven 1.05 m long, 0.15 m deep and 0.15 m high scintillator bars. Both ends of each bar were

Table 2.8: DLC compositions

| Material | Thickness | Thickness ($mg/cm^2$) |
|---|---|---|
| Aluminized mylar | 25 $\mu m$ | 3.3 |
| Magic gas | 14-20 mm | 3.4 |
| Mylar | 25 $\mu m$ | 3.3 |
| Copper cathode strip | 20 $\mu m$ | 18.0 |
| Magic gas | 6 mm | 1.2 |
| Tungsten anode wire | 20 $\mu m$ | 38.0 |
| Magic gas | 6 mm | 1.2 |
| Copper cathode strip | 20 $\mu m$ | 18.0 |
| Mylar | 25 $\mu m$ | 3.3 |
| Magic gas | 14-20 mm | 3.4 |
| Aluminized mylar | 25 $\mu m$ | 3.3 |

terminated by modified Winston cone [62] light guides designed to accept light which falls on the inner surface of the bars at angles $\leq 15^0$. In order to veto charged particles three overlapping scintillators were placed in front of the array. Behind each bar of the rear bank of each neutron array there were a set of seven small 70 mm wide, 64 mm high and 7 mm thick 'button' scintillators (fig 2.12). They are imbedded in a lucite light guide. The signals from the passing protons which penetrated to the button counters were used to adjust the pulse height and time delays for each scintillator bar. This was done at the beginning of each phase of the two data taking runs. The arrays were put at forward angles where the passing protons were sufficiently energetic to penetrate the two stacks of scintillator bars. Data taken under this condition were analyzed off line immediately. On the basis of this analysis the phototube voltages and the different delays in the bars were adjusted to the desired values. A 1.6 mm thick scintillator (NTOF) placed 50 cm from the target guarantees that the charged particles

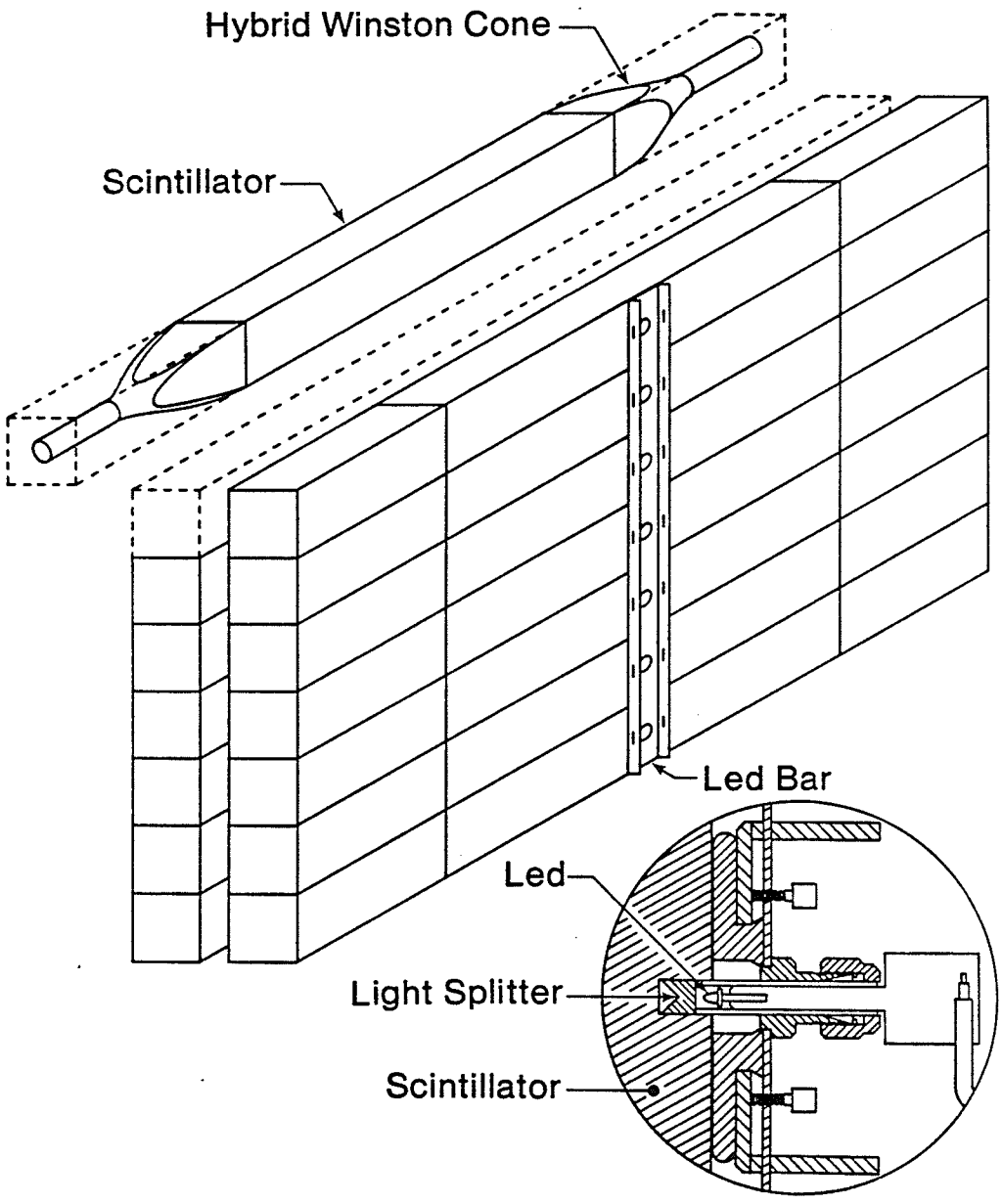


Figure 2.13: One of two Neutron Arrays.

Table 2.9: Distances of neutron arrays from FST center

| Scattered neutron angles (lab) : | | | | | | | | | |
|---|---|---|---|---|---|---|---|---|---|
| left& right | $67^0$ | $61^0$ | $57^0$ | $52^0$ | $47^0$ | $42^0$ | $37^0$ | $32^0$ | $27^0$ |
| Left neutron array positions (mm) : | | | | | | | | | |
| Veto | 2293 | 2720 | 3922 | 4282 | 4522 | 4611 | 4340 | 4270 | 4284 |
| 1st bank | 2454 | 2881 | 4083 | 4443 | 4683 | 4772 | 4501 | 4431 | 4445 |
| 2nd bank | 2644 | 3071 | 4273 | 4633 | 4873 | 4962 | 4691 | 4621 | 4635 |
| Button | 2769 | 3196 | 4398 | 4758 | 4998 | 5087 | 4816 | 4746 | 4760 |
| Right neutron array positions (mm) : | | | | | | | | | |
| Veto | 2261 | 2731 | 3934 | 4316 | 4530 | 4541 | 4383 | 4286 | 4302 |
| 1st bank | 2406 | 2876 | 4079 | 4461 | 4675 | 4686 | 4528 | 4431 | 4446 |
| 2nd bank | 2607 | 3077 | 4280 | 4662 | 4876 | 4887 | 4729 | 4632 | 4647 |
| Button | 2740 | 3210 | 4413 | 4795 | 5009 | 5020 | 4862 | 4765 | 4780 |

originate at the target. Details of this technique will be discussed in the following chapters. Pulser signals injected in each neutron bar through the light emitting diodes, were used to monitor the stability of neutron bars. Table 2.9 summarizes the positions of different detection elements of each neutron detection system.

The time difference from two ends of each bar gave the horizontal positions of the neutrons in the bars. The vertical coordinates were determined by knowing which of the seven bars were struck. The vertical resolution for a single bar hit was $\pm 75\ mm$ , half the height of each bar. The horizontal position resolution was obtained from the difference of the positions of button events in the front and back bars and was found to be 32 $mm$ FWHM. The neutron time-of-flight between the neutron array and the FST center was determined from the arrival time of neutrons in scintillator bars with respect to the proton time-of-flight start counter and then correcting for the travel time of neutrons between the target center and the start counter.

## 2.7 Alignment and Setting Up of the Detectors

The angles and the positions of the proton booms and the neutron arrays are listed in table 2.10. Because of the target holding field the recoil protons were deflected from their canonical angles. This holding field deflection was compensated for by displacing the booms by the corresponding angle. The target holding field was always 'up'. The proton boom on the right hand side of the incident beam (viewed along the beam direction) was put at angles larger than the canonical angles, whereas the boom on the left was put at angles smaller than the canonical angles.

The setting up of the proton booms and their alignment were done in the following way. First the booms were put at the nominal angles that were marked with theodolite from nominal target location to an accuracy of $\pm 0.05^0$ on the floor. Each boom is 4 m long and has a plumb bob hanging from the rear. A brass rule was made [63] with graduated marks on it. The smallest division on the rule corresponds to $0.1^0$ when placed at 4 m away from the pivot point. This rule was put right beneath the plumb bob and the boom angles were then corrected for the deflection, adding the deflection angle to one side (right) and subtracting from the other (left). Using a leveled theodolite and the fiducial lines on the boom uprights the feet of the booms were adjusted to bring the central median planes of the detectors to the beam height. The leveling of the booms was checked with spirit levels. The angles were carefully recorded and later checked before changing to set the booms at another angle. The booms were positioned to within $\pm 0.05^0$ to the correct angle. The heights of the detector median planes were within $\pm 1.0\ mm$ of the beam height.

The positioning of the neutron arrays was done in the following way. The set of angular positions of each array were the same for all three incident energies. However the radial position was changed with scattering angle to maximize the solid angle coverage of the detector system. For each neutron angle setting four holes were drilled in the floor and four brackets with brass positioning screws were put into the hole around the array. The lengths of these screws were varied to set the arrays at correct angle and positions. The arrays were jacked up to the beam height using a leveled theodolite as a reference. The bars were leveled by using a spirit level. In this way the neutron arrays could be positioned to within $\pm 0.05^0$ of the nominal angle.

Table 2.10: Kinematic table

| Neutron energy = 220 MeV | | | | |
|---|---|---|---|---|
| Neutron array angle (deg) (a) | Neutron array position (cm) (e) | Proton boom angle (deg) (b) | Recoil proton energy (MeV) (c) | Deflection angle (deg) (d) |
| 67.0 | 234.0 | 20.72 | 189.67 | 1.13 |
| 61.0 | 300.0 | 26.32 | 172.75 | 1.20 |
| 57.0 | 420.0 | 30.11 | 159.90 | 1.26 |
| 52.0 | 456.0 | 34.92 | 142.43 | 1.35 |
| 47.0 | 480.0 | 39.81 | 123.85 | 1.49 |
| 42.0 | 480.0 | 44.80 | 104.68 | 1.69 |
| 37.0 | 456.0 | 49.88 | 85.49 | 2.01 |
| Neutron energy = 325 MeV | | | | |
| 67.0 | 234.0 | 19.81 | 282.05 | 0.89 |
| 61.0 | 300.0 | 25.23 | 257.83 | 0.94 |
| 57.0 | 420.0 | 28.91 | 239.32 | 0.98 |
| 52.0 | 456.0 | 33.62 | 214.01 | 1.05 |
| 47.0 | 480.0 | 38.44 | 186.85 | 1.41 |
| 42.0 | 480.0 | 43.40 | 158.60 | 1.27 |
| 37.0 | 456.0 | 48.49 | 130.08 | 1.44 |
| 32.0 | 456.0 | 53.73 | 102.21 | 1.71 |
| Neutron energy = 425 MeV | | | | |
| 67.0 | 234.0 | 19.01 | 370.96 | 0.76 |
| 61.0 | 300.0 | 24.26 | 340.22 | 0.80 |
| 57.0 | 420.0 | 27.85 | 316.58 | 0.83 |
| 52.0 | 456.0 | 32.45 | 284.06 | 0.89 |
| 47.0 | 480.0 | 37.21 | 248.94 | 0.96 |
| 37.0 | 456.0 | 47.23 | 174.65 | 1.19 |
| 27.0 | 456.0 | 57.98 | 102.74 | 1.70 |

(a) Central angle of each neutron array. (b) Central angle of each proton boom. (c) Recoil proton energy at target center
(d) Proton deflection angle in 0.257 T magnetic holding field of the frozen spin target. (e) Distance between the vertical plane midway between two scintillator banks and the target center.

# Chapter 3

# Data Acquisition

As mentioned in the last chapter, the experiment was carried out in two phases. Each phase of $A_{yy}$ running was preceded and followed by target calibration runs. In this chapter only the $A_{yy}$ configuration of the experiment will be described. Most of the electronics involved were the same for both the $A_{yy}$ and the target calibration parts of the experiment.

## 3.1 Electronics

The electronic diagrams for the proton polarimeter (CSB) and the beam energy monitor are shown in fig 3.1. The number of accidental events for the polarimeter was determined by delaying the recoil counter signal by 44 ns which is the time interval between two beam bursts. In the beam energy monitor, the trigger for a particle stopping in the scintillator $B_i$ (fig 2.3) or in the copper between scintillator $B_i$ and $B_{i+1}$ is

$$A_1 \cdot A_2 \cdot A_3 \cdot B_1 \cdots B_i \cdot \bar{B}_{i+1} \cdots \bar{B}_6$$

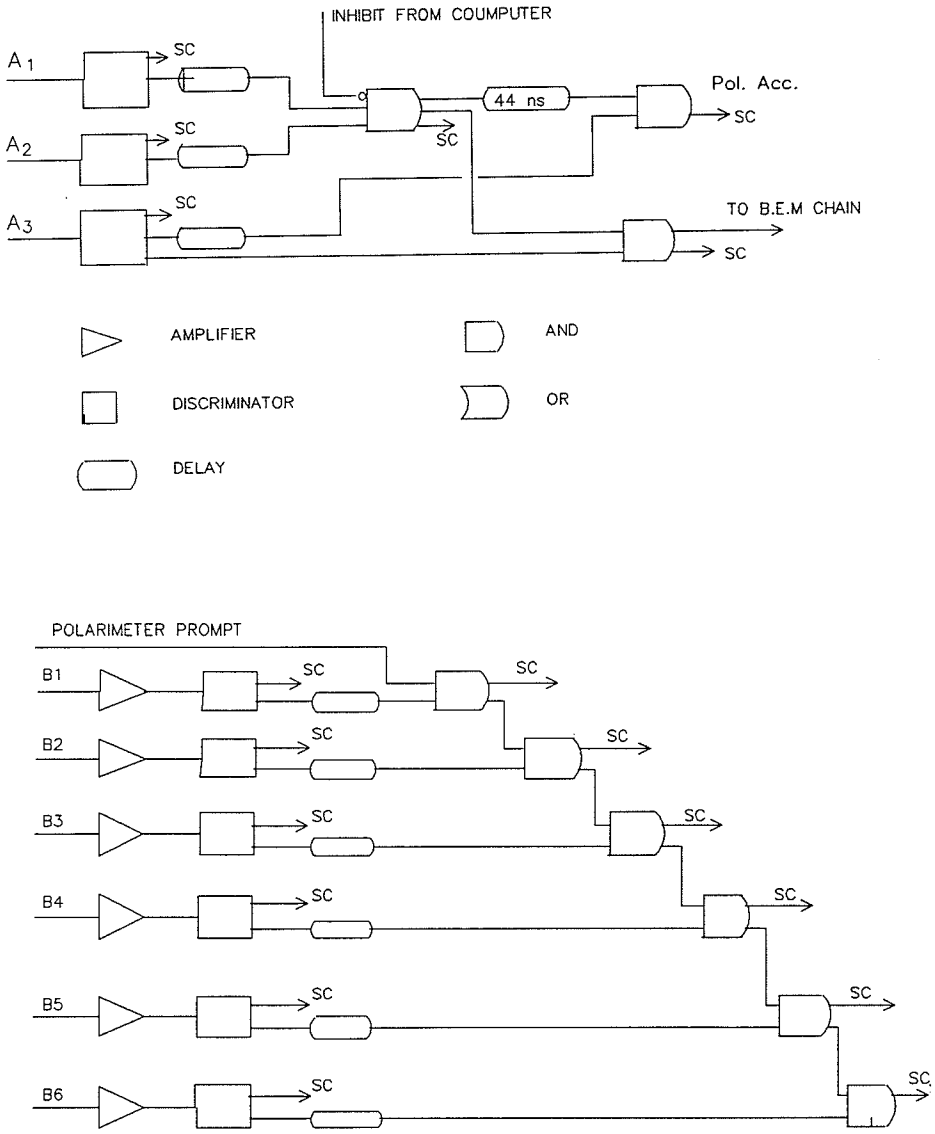


Figure 3.1: Proton polarimeter and beam energy monitor electronics (left or right side events)

The coincidences were scaled as :

$$(A_1.A_2.A_3.B_1), (A_1.A_2.A_3.B_1.B_2) \cdots (A_1.A_2.A_3.B_1. \cdots B_6)$$

and the rates for particles stopping in $B_i$ were determined by taking the difference between successive scalers.

The electronics diagram for the neutron polarimeter and profile monitor is shown in fig 3.2. During the experiment, the primary proton beam upstream of the $LD_2$ target had to be retuned for each energy. Once a satisfactory primary beam tune was established a prescale switch in the profile monitor was set to adjust the ratio of profile monitor events to main data events (10-20%). Both the horizontal and vertical neutron profiles were examined; the beam line elements upstream of the $LD_2$ target were adjusted to center the neutron beam on the profile monitor.

The electronic diagrams for the neutron and proton detection systems and the master triggering assembly are summarized in figs 3.3-3.5. A detected proton required the proton time-of-flight counter, $\Delta E$-counter and E-counter to fire, whereas a detected neutron required proton time-of-flight signal and the signal from neutron scintillator array with no signal from the veto counter. For a 'button' event, the n-tof, veto and button counters had to fire. In order to minimize the number of timing circuits, the signals from the scintillator bars 1,3,5 and 7 and the signals from bars 2,4 and 6 were daisy chained (fig 3.4). The signals from each bar were delayed by a certain amount in order to identify the individual bar.

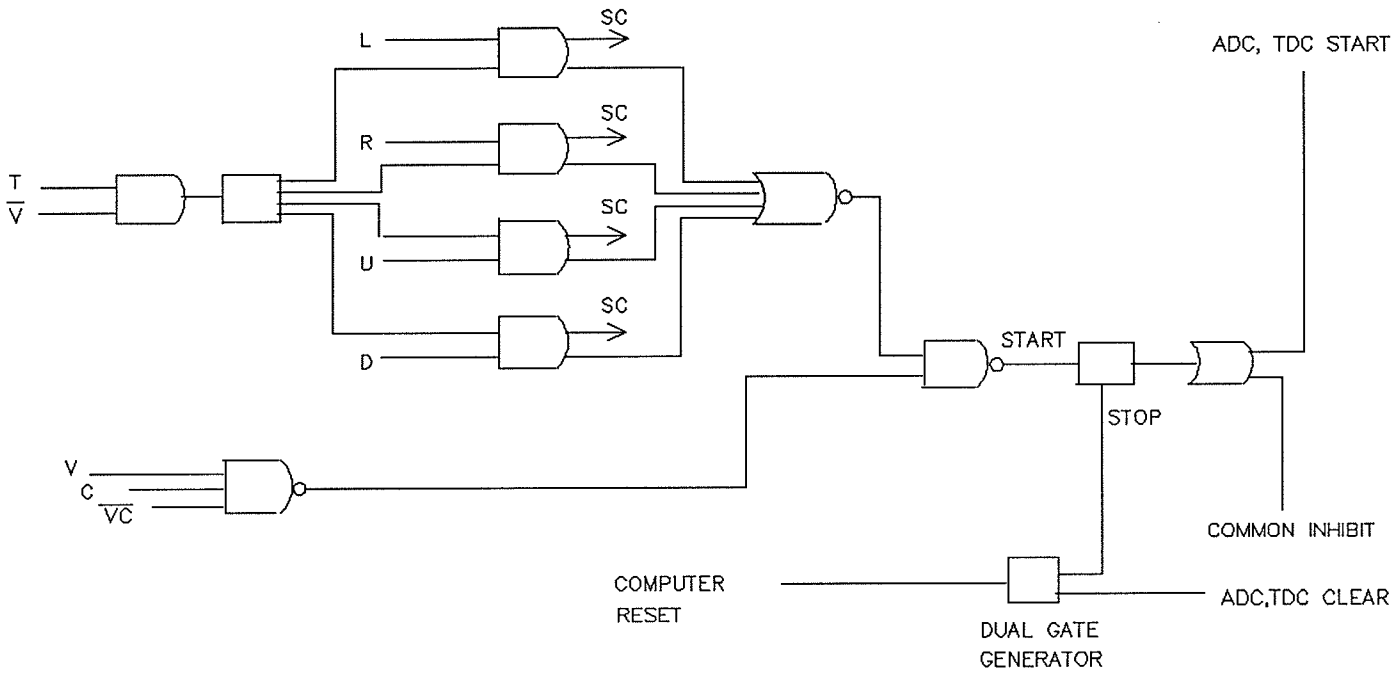


Figure 3.2: Neutron profile monitor and polarimeter electronics

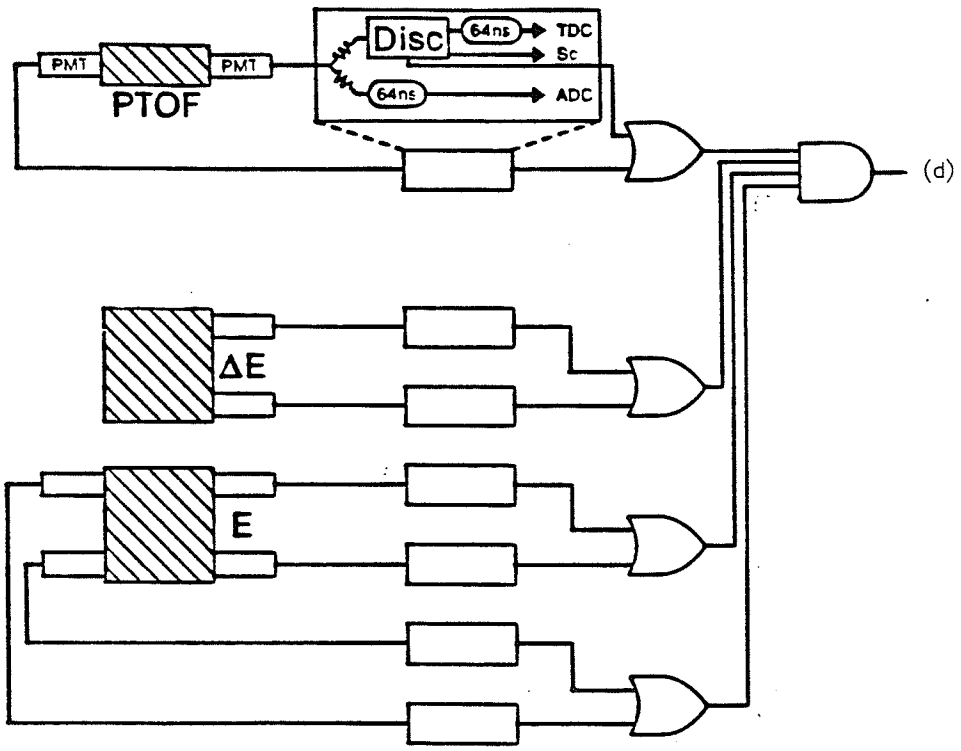


Figure 3.3: Proton detection system electronics

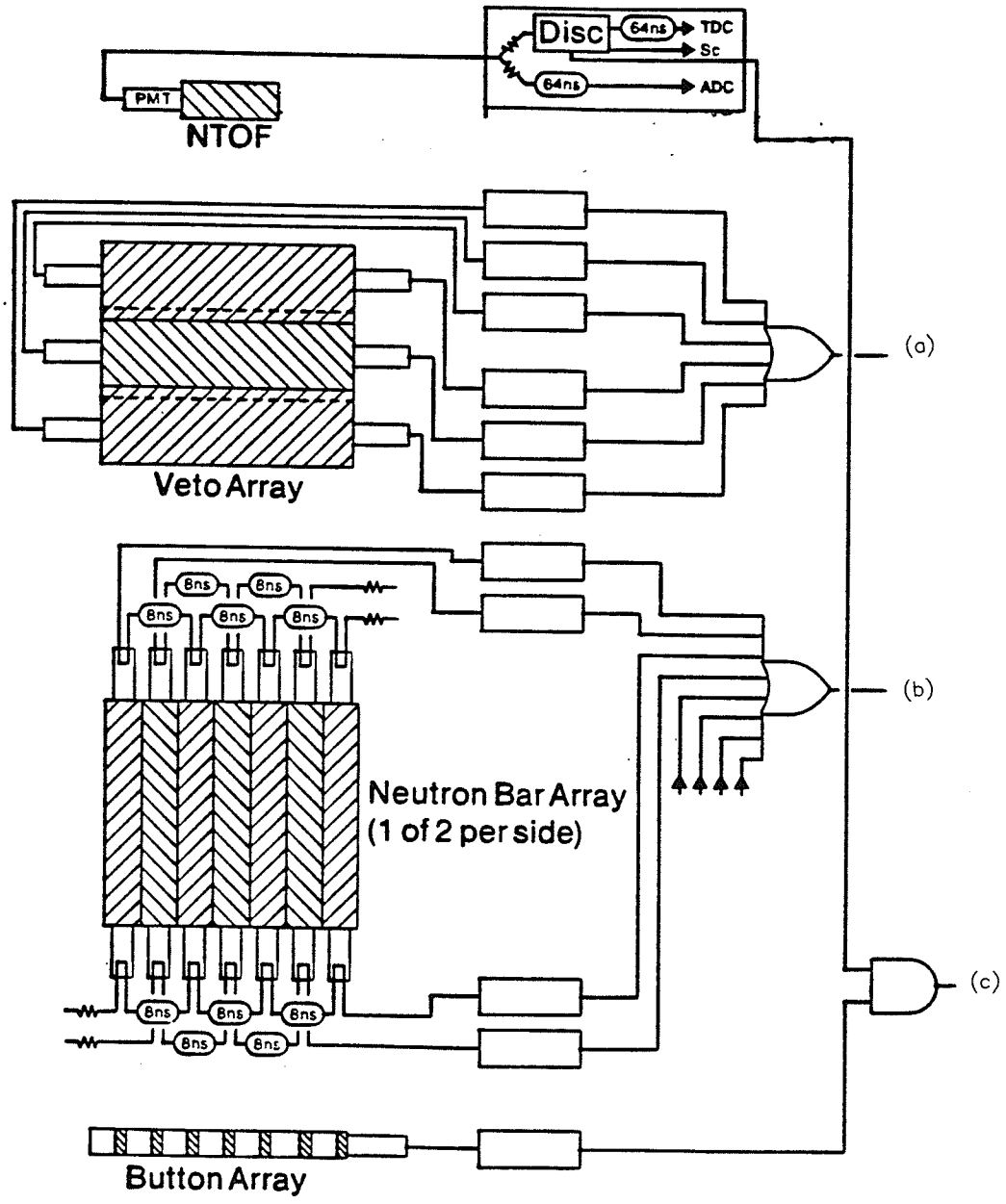


Figure 3.4: Neutron detection system electronics. The ends marked a,b and c are connected to the triggering system as shown in next figure.

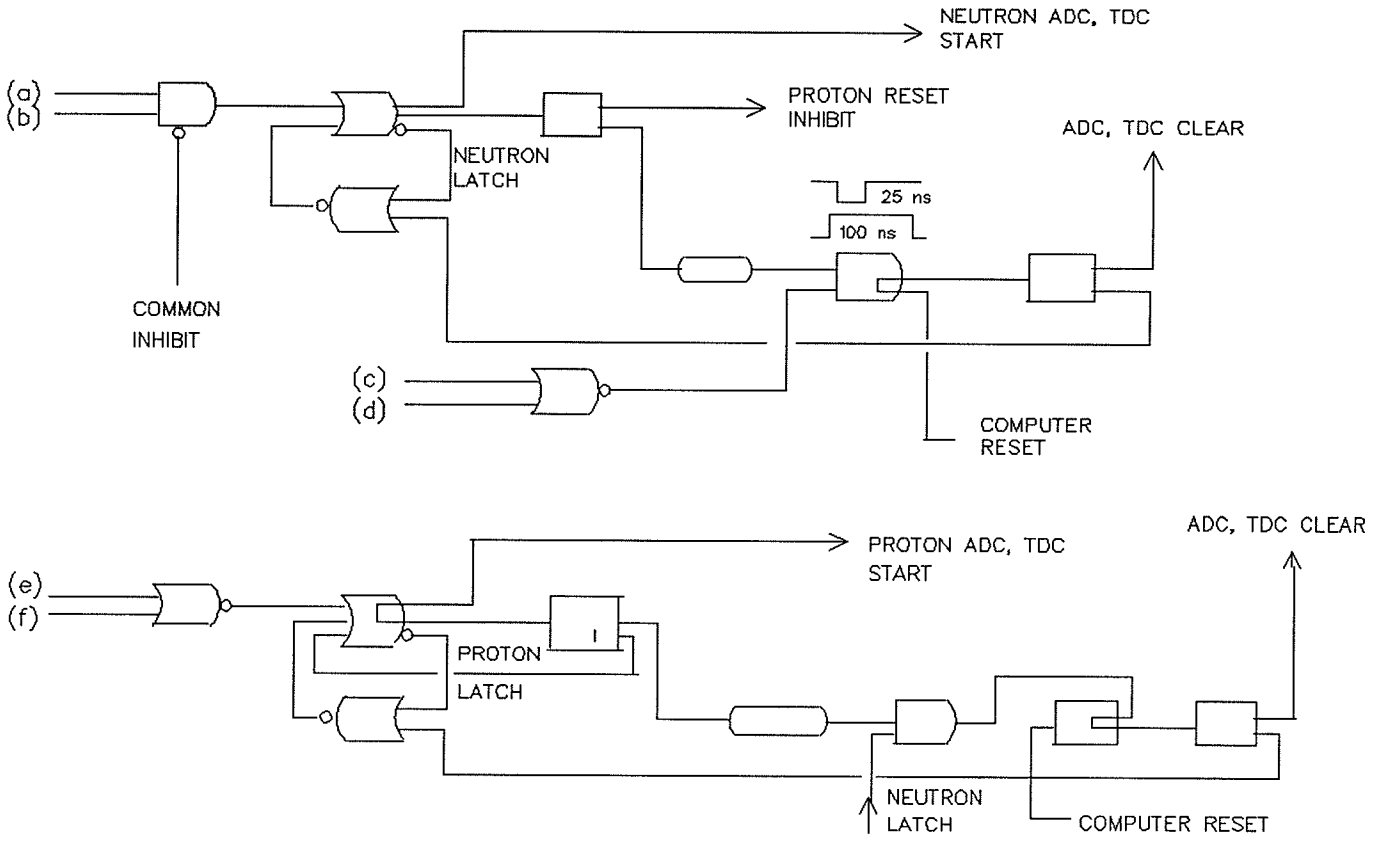


Figure 3.5: Neutron and proton trigger systems. The neutron latch is set by (a) no veto signal and (b) a neutron scintillator fired. The signals from (c) button events or (d) proton boom are required for the coincidence. For a proton trigger the signals from the time-of-flight and (e) $\Delta E$ counter and (f) the E-counter are required.

Table 3.1: Summary of a tape block

| Word # | What it contains |
|---|---|
| 1 | Start of a block, block length in bytes |
| 2 | Zero |
| 3 | First event, gives event length in bytes |
| 4 | Zero |
| 5 | Left byte of this word contains an event termination code. Right byte contains the length of the event. |
| 6 | Left byte of this word indicates the event type. The right byte contains high order 8 bits of a 24-bit event sequence number. |
| 7 | This word contains the low order 16 bits of the sequence number. |
| 8 | Beginning of real data. Header word for a module. |

## 3.2 Data Transfer and On-line Monitoring

The DACS data acquisition program running on the Data General ECLIPSE computers at TRIUMF was used for the acquisition and on-line monitoring of the data. Whenever an event triggered the logic the CAMAC modules were read and the data were transferred to tape. The computer sent a busy signal to inhibit the further acquisition of data while the previous data were still being transferred to the data buffer. There was a busy signal coming from the polarized ion source. The spin controller sent this busy signal whenever the beam spin was being changed. Data were written on tape in variable block length with a maximum of 1024 16-bit words per block. Events were also of variable length, each event contained entirely within one tape block. In table-3.1 we have summarized what a tape block looked like.

There were seven different event types.

- Event types 1 and 5 contained all the scaler information. In the ex-

periment there were about 130 scalers altogether. Both these types of event were read every five seconds as clock events.

- Event type 2 was the main n-p coincidence event where we had all the TDCs, ADCs and wire chamber information. Events with the left neutron array and right proton detectors firing were defined as left events. For right events, the right neutron array and the left proton detectors had to fire. Note that here left and right simply mean the left and right hand sides of the incident beam direction. Whether an event was a left event or a right event was identified by a bit in the Digital Coincidence Register (DCR) unit. The least significant bit signifies a left event while the next higher bit corresponds to a right event. Table-3.2 summarizes the assignments of the bits of the DCR.

- Event type 3 was the neutron profile monitor and polarimeter event. These events were prescaled in hardware.

- Event type 4 was a clock event which read the high voltages from all the LeCroy Mainframes every 10 minutes.

- Event type 7 was the FST event. This was also a clock event which was read every five minutes. The object of this event type was to check on various FST parameters such as the temperature, vacuum etc.

- Event type 9 was the button event (sec 4.3) triggered by the scattered protons that were energetic enough to penetrate the upstream and downstream banks of each neutron array to fire seven small 'button' scintillators located at the downstream side of each array. The purpose of this event type will be explained in the next chapter. Because of the low energy of 'button' protons there were not many button events at

Table 3.2: DCR bit asignments

| Bit # | Event |
|---|---|
| 0 | nL.pR neutron left, proton right |
| 1 | nR.pL neutron right , proton left |
| 2 | nL veto present (i.e. Left button event) |
| 3 | nR veto present (i.e. Right button event) |
| 4 | — |
| 5 | DLC trip |
| 6 | $U.\bar{B}$ spin up, not busy |
| 7 | $D.\bar{B}$ spin down, not busy |
| 8 | $O.\bar{B}$ spin off, not busy |
| 9 | RF signal present |
| 10 | B (busy) |
| 11 | Pulser |

most of the angle and energy settings.

There was no on-line rejection of data. Among various things that were monitored during the experiment the most important was a continuous check on the functioning of all the TDC and ADC modules. For this a two dimensional spectrum with the channel numbers on the x-axis and the word numbers on the y-axis was defined. Note that the word numbers correspond to the locations of different detector module channel address in a tape block. One such plot is shown in fig 3.6. In the figure, the first word corresponds to the location of word no. 6 of the table 3.1. Thus the words 8-17 (fig 3.6) are the proton boom ADCs, the corresponding TDCs are the words 19-29. The neutron array ADCs are the words 31-45 whereas the words 50-60 correspond to the neutron detection system TDCs. The delay line chamber TDCs are the words 62-78. There was also an on-line check of all the scalers and their rates. At the end of each tape the scalers were printed and were checked very carefully before starting the next tape. The check on the neu-

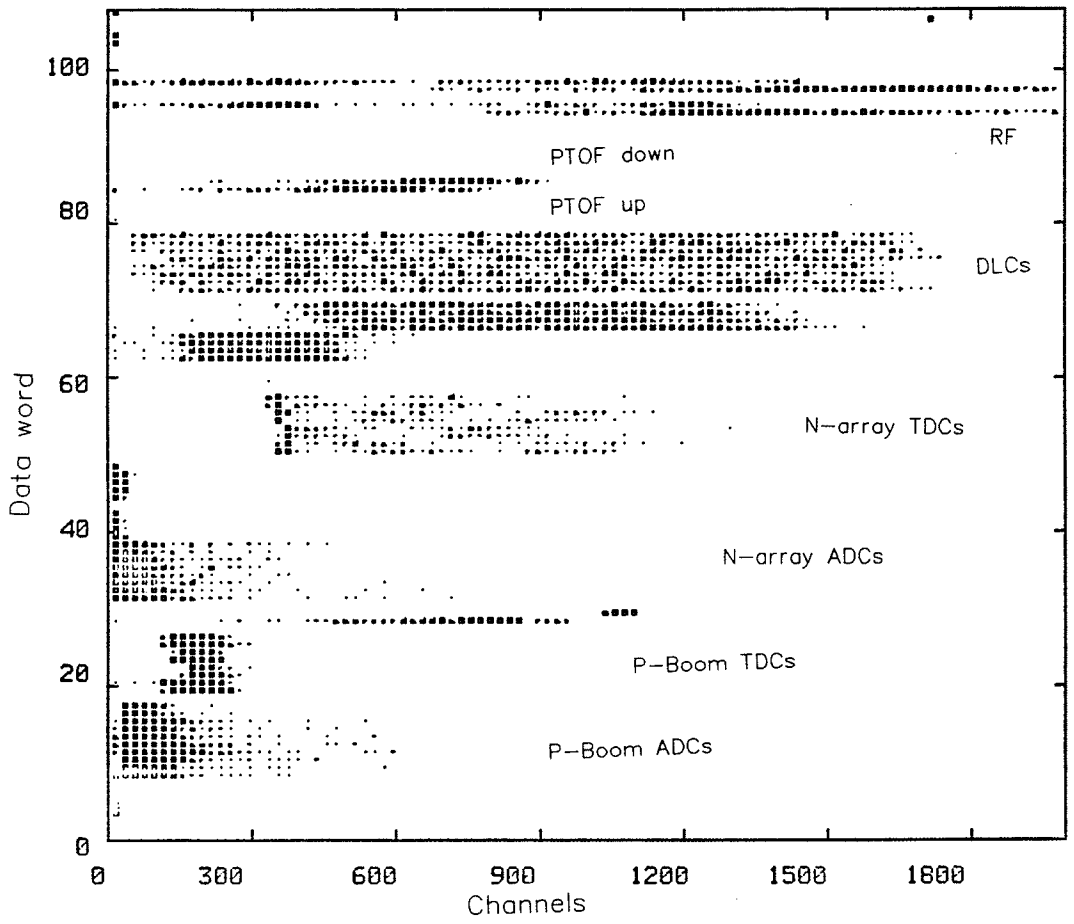


Figure 3.6: Two dimensional index spectrum showing the different TDC and ADC modules.

tron beam profiles ensured that the neutron beam was properly centered on the frozen spin target. For a beam current of 400 nA, the trigger rate for the np coincidence events was about 70 per second.

# Chapter 4

# Data Analysis

The complete analysis of the data taken in the $A_{yy}$ mode was carried out by using 'LISA' [64] which is a general purpose interactive data analysis program capable of working in the DCL environment of the VAX-VMS system. Fig 4.1 shows the flow chart for event by event processing in LISA. The user routine 'INSERT' does all the specific experiment dependent event by event transformations and manipulations of the data. Most of the subroutines in this routine have been adapted from another data analysis program called 'PERSEUS' [65], and then modified to suit our purpose. The hybridization of these two programs, LISA and PERSEUS, made this present analysis program extremely thorough, versatile and flexible.

## 4.1 Scaler Analysis

There were 130 scalers in total read in the experiment. At the beginning of the analysis we looked into all the scaler values and used the polarimeter scalers to determine the proton beam polarizations and its energy, the neutron polarimeter asymmetries and the computer dead times.

### 4.1.1 Proton Beam Polarization and Energy

The polarization and energy of the primary proton beam were measured by the BEM/Polarimeter combination referred to as the CSB polarimeter in chapter 3 (fig 2.1). In the In-Beam Polarimeter (IBP) we also measured the beam polarization independently. However, the primary beam was focussed on the CSB polarimeter. Furthermore, the same target foil was used in the IBP throughout each phase of the experiment and thus the polarizations obtained from this polarimeter could not be very reliable because of continuous hydrogen loss from the foil. The polarization values referred to in this thesis are actually the polarizations measured in the CSB polarimeter. During the experiment the spin direction of the beam was changed in a semi-random fashion ; the beam was 'up' for 3 minutes, 'down' for 3 minutes and 'off' for 1 minute in one complete spin cycle. At the end of two hours of running there were almost equal numbers of 'up' and 'down' events. The 'up'('+') and 'down'('-') polarizations are determined from :

$$P_+ = \frac{\epsilon_+}{A_y}, \quad P_- = \frac{\epsilon_-}{A_y} \tag{4.1}$$

$A_y$ is the p-p analyzing power at $17^0$(lab) obtained from Arndt's energy dependent phase shift analysis [13]. The $A_y$ values at three primary beam energies are summarized in table-4.1. The errors assigned to the analyzing powers are obtained from Arndt's single energy phase shift solutions and are treated as the systematic errors in the final error calculation. The $\epsilon$'s are the left-right asymmetries corrected for the instrumental asymmetry and are given by :

$$\epsilon = \frac{L - R}{L + R} - \epsilon_0 \tag{4.2}$$

where L and R are the accidental subtracted left and right yields. $\epsilon_0$ is the instrumental asymmetry. The polarization averaged over 'up' and 'down'

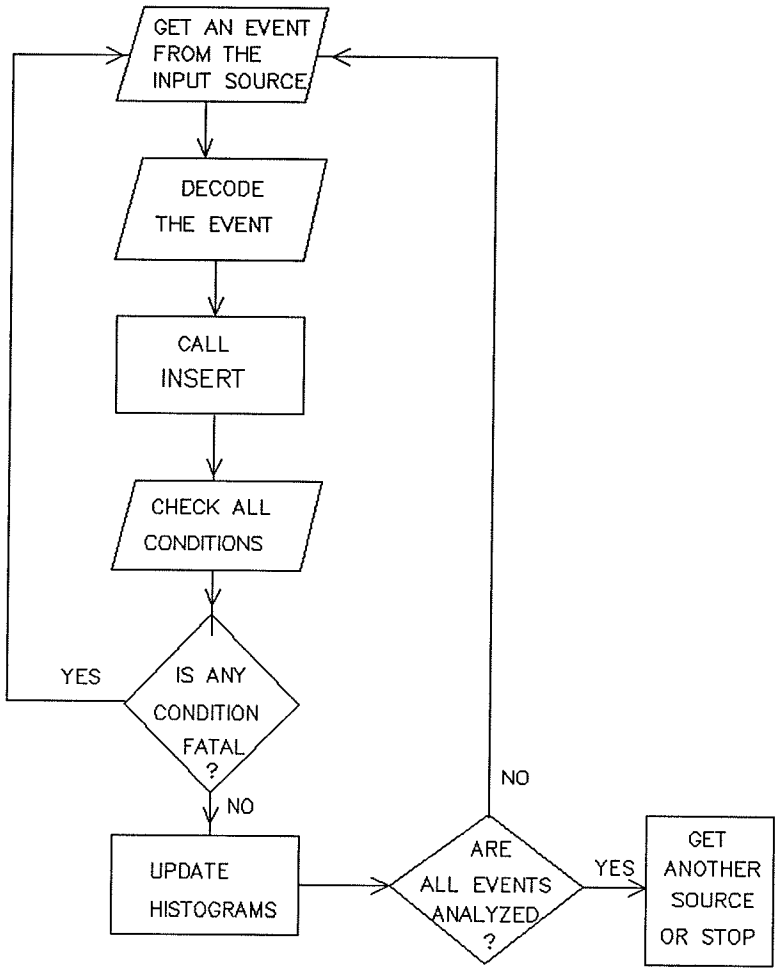


Figure 4.1: Flow chart for the 'LISA' event analysis program

Table 4.1: p-p analyzing powers

| Proton beam energy (MeV) | Scattering Angle (deg) | $A_y$ $(H_2)$ | $A_y$ $CH_2$ |
|---|---|---|---|
| 235 | 17 | 0.3450±1.5% | 0.3174±1.5% |
| 343 | 17 | 0.4388±1.5% | 0.4064±1.5% |
| 445 | 17 | 0.4918±1.5% | 0.4553±1.5% |

spin states is determined from:

$$P_{av} = \frac{\epsilon}{A_y} \equiv \frac{1}{A_y}\frac{\sqrt{X}-1}{\sqrt{X}+1} \tag{4.3}$$

$$X = \frac{L_+ R_-}{L_- R_+} \tag{4.4}$$

The target used in the CSB polarimeter was kapton foil. Since the target foil contains carbon, the above asymmetries in equations (4.2) and (4.3) are to be corrected for the carbon contamination. The corrected asymmetry is related to the above asymmetries by the following expression :

$$\epsilon_{corr} = \alpha\,\epsilon \tag{4.5}$$

$$\equiv (1+\rho-\rho\,\frac{\epsilon_C}{\epsilon})\epsilon \tag{4.6}$$

where $\rho$ is the fraction of carbon to hydrogen counts in either of kapton or $CH_2$ foil, i.e.

$$\rho = [\frac{L_C + R_C}{L_H + R_H}]_{kapton} \tag{4.7}$$

and $\epsilon_C$ is the asymmetry originating from Carbon and is obtained by using a 177.5 $mg/cm^2$ carbon target (the only carbon target available) in place of the kapton target.

From the total of left and right counts from kapton and carbon targets the following ratio is formed.

$$\frac{L_C^{kapton} + R_C^{kapton}}{L_C^{carbon} + R_C^{carbon}} = \frac{SEM_{kapton}}{SEM_{carbon}} \times \frac{r_{carbon} t_{kapton}}{t_{carbon}} \tag{4.8}$$

where $r_{carbon}$ is the fraction of carbon atoms present in one molecule of kapton. The t's are the thicknesses of the corresponding targets. The secondary electron emission monitor (SEM) counts and the sum of left and right counts from the carbon target ($L_C^{carbon} + R_C^{carbon}$) are known. Thus using the above equation one finds $L_C^{kapton} + R_C^{kapton}$. The total values of the left and right counts from a kapton target ($L + R$) is known. Thus

$$L_H + R_H = L + R - (L_C + R_C) \tag{4.9}$$

Knowing these values $\rho$ as well as $\alpha$ can be extracted. In the same way one can find the corresponding values for a $CH_2$ target. Note that $\alpha$ for the kapton targets is 1.028 and that for the $CH_2$ targets is 1.006. The variation of these two parameters with energy is negligible.

The polarimeter performance was checked by forming the left and right efficiency ratio (after correcting for accidentals), viz.

$$\frac{e_L}{e_R} = \sqrt{\frac{L_+ L_-}{R_+ R_-}} \tag{4.10}$$

This ratio should remain constant with time provided the 'up' and 'down' polarizations are the same and do not change with time. It is also assumed that the left and right solid angle acceptances are the same. However, that may change with the change in the instrumental asymmetry. This ratio found on a tape by tape basis for one energy is plotted in fig 4.2. The 'up', 'down' and average polarizations for each neutron angle setting are summarized in table 4.2.

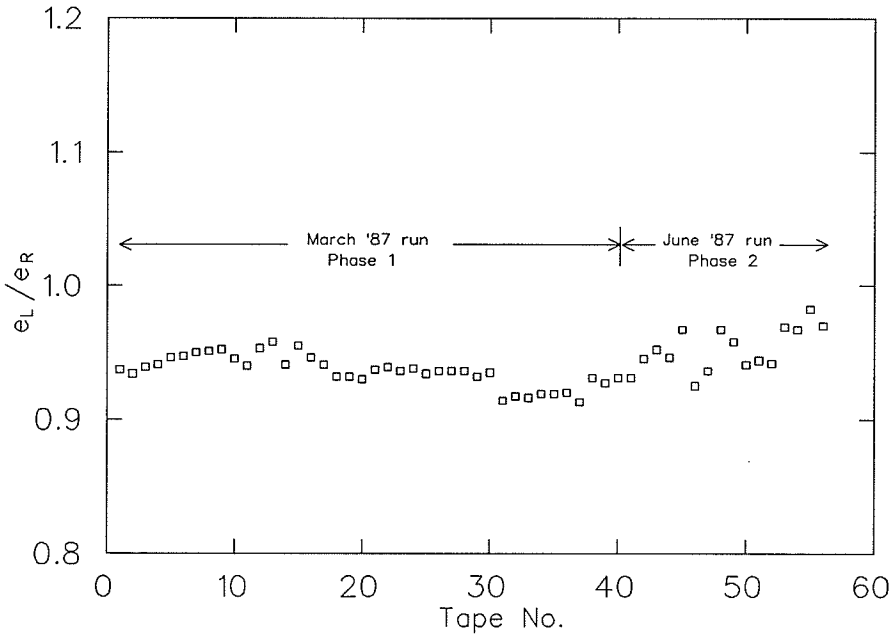


Figure 4.2: The proton polarimeter left-right efficiency ratio

The average energy of the incident proton beam was measured by knowing the number of stopping protons in each of six scintillators in the beam energy monitor assembly (fig 2.3). For example, if $N_i$ is the number of protons stopping in the i'th scintillator, $B_i$, then the average energy is extracted as :

$$< T > = \frac{\sum_i a_i(N_i - N_{i+1})}{\sum_i (N_i - N_{i+1})} \tag{4.11}$$

where $a_i$ is the energy of the protons whose range extend up to the $B_i$' th scintillator or to the Cu sheet after it. The number of protons stopping in the scintillator $B_i$ is determined from the trigger condition expressed in eqn 3.1. The BEM has two detector arms. The incident proton beam energy is averaged over both left and right arms of the BEM assembly. The primary proton beam energies as determined on a tape by tape basis are plotted in fig 4.3. During the 343 MeV run, the first scintillator on the right BEM assembly was not working between tape 36 and tape 48 in fig 4.3a. In

Table 4.2: Proton Beam Polarizations[!]

| Proton Beam energy (MeV) | Neutron Array angle (deg) | Proton beam polarization | | | | | |
|---|---|---|---|---|---|---|---|
| | | target spin up | | | target spin down | | |
| | | up | dn | av. | up | dn | av. |
| 445 | 67.0 | 0.730 | 0.705 | 0.718 | 0.725 | 0.710 | 0.718 |
| | 61.0 | 0.690 | 0.684 | 0.688 | 0.746 | 0.688 | 0.718 |
| | 57.0 | 0.710 | 0.691 | 0.701 | 0.726 | 0.701 | 0.714 |
| | 52.0 | 0.748 | 0.705 | 0.727 | 0.726 | 0.707 | 0.717 |
| | 47.0* | 0.747 | 0.704 | 0.726 | 0.737 | 0.699 | 0.718 |
| | 47.0# | 0.722 | 0.717 | 0.720 | 0.732 | 0.718 | 0.725 |
| | 37.0 | 0.726 | 0.710 | 0.719 | 0.723 | 0.714 | 0.719 |
| | 27.0 | 0.723 | 0.713 | 0.718 | 0.731 | 0.719 | 0.725 |
| 343 | 67.0 | 0.758 | 0.749 | 0.754 | 0.761 | 0.739 | 0.750 |
| | 61.0 | 0.759 | 0.748 | 0.754 | 0.768 | 0.737 | 0.753 |
| | 57.0 | 0.755 | 0.754 | 0.755 | 0.767 | 0.738 | 0.753 |
| | 52.0 | 0.722 | 0.759 | 0.741 | 0.768 | 0.728 | 0.748 |
| | 47.0 | 0.725 | 0.780 | 0.753 | 0.757 | 0.754 | 0.756 |
| | 42.0 | 0.771 | 0.736 | 0.755 | 0.756 | 0.750 | 0.753 |
| | 37.0 | 0.724 | 0.734 | 0.729 | 0.728 | 0.731 | 0.730 |
| | 32.0 | 0.729 | 0.739 | 0.734 | 0.728 | 0.715 | 0.722 |
| 235. | 67.0 | 0.796 | 0.776 | 0.786 | 0.814 | 0.788 | 0.801 |
| | 61.0 | 0.797 | 0.774 | 0.785 | 0.820 | 0.793 | 0.806 |
| | 57.0 | 0.791 | 0.773 | 0.782 | 0.815 | 0.789 | 0.802 |
| | 52.0 | 0.786 | 0.770 | 0.778 | 0.836 | 0.797 | 0.816 |
| | 47.0 | 0.789 | 0.767 | 0.778 | 0.804 | 0.806 | 0.805 |
| | 37.0 | 0.801 | 0.813 | 0.808 | 0.795 | 0.806 | 0.802 |

! typical error in polarization is $\pm 0.002$

* March 1987 run ; # June 1987 run

Table 4.3: Average Primary Proton Beam Energies

| Run | Phase 1 | | | | Phase 2 | | | |
|---|---|---|---|---|---|---|---|---|
| | Average energy (MeV) | Standard deviation (MeV) | Maximum energy (MeV) | Minimum energy (MeV) | Average energy (MeV) | Standard deviation (MeV) | Maximum energy (MeV) | Minimum energy (MeV) |
| 1 | 444.09 | 0.19 | 444.39 | 443.79 | 443.50 | 0.04 | 443.53 | 443.44 |
| 2 | 342.86 | 0.07 | 343.04 | 342.74 | 341.31 | 0.54 | 342.10 | 340.72 |
| 3 | 234.57 | 0.59 | 235.60 | 233.46 | 234.97 | 0.42 | 235.04 | 233.40 |

finding the average energy during that period the first scintillator on both left and right sides has been excluded. Also at that time the cyclotron RF was very unstable. This may explain the lower values of the beam energy for that period. There are also some step like discontinuities in all three energies evident in the figure. These discontinuities occur right after the shut down for the maintenance day or after an angle change which involved removing the stripper foil for a prolonged access. The mean energies averaged over about 60 tapes for each incident energy run are summarized in table-4.3.

### 4.1.2 Neutron Beam Polarization

The neutron polarimeter scalers were used to measure both horizontal and vertical asymmetries caused by the vertical and horizontal components of the neutron beam polarization. Since the effective analyzing power for this polarimeter is not well known, the beam polarizations could not be inferred directly from these asymmetries. Instead, the proton beam polarization and the polarization transfer coefficients were used to extract the vertical component of the neutron beam polarization (eqn. 2.3). The effective analyzing powers for the left-right and up-down asymmetries are not the same. This is because the vertical and horizontal neutron beam profiles are different and

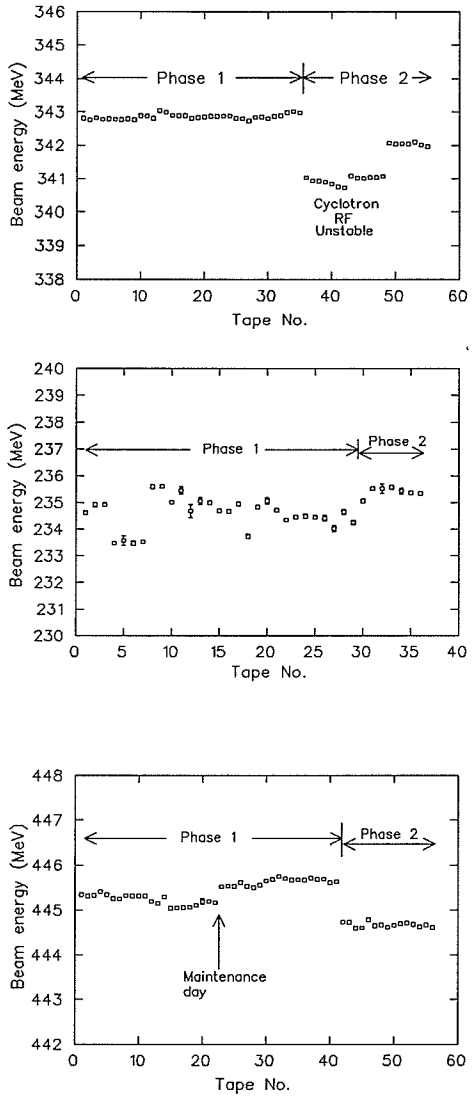


Figure 4.3: Incident beam energies measured in the Beam Energy Monitor (relative scale).

Table 4.4: Quasi-elastic spin transfer coefficients [13]

| Incident beam energy (MeV) | Energy at the center $LD_2$ target | $r_t$ | $r'_t$ |
|---|---|---|---|
| 235 | 227.8 | $-0.919 \pm 0.004$ | $0.011 \pm 0.005$ |
| 343 | 337.2 | $-0.938 \pm 0.008$ | $0.002 \pm 0.009$ |
| 445 | 440.0 | $-0.849 \pm 0.009$ | $0.015 \pm 0.008$ |

thus the horizontal and vertical acceptances differ. However, the difference in analyzing powers is very small and thus the ratio of these two asymmetries is almost equal to the ratio of the two components of polarization. The polarization transfer coefficients, $r_t$ and $r'_t$, used for determining the neutron beam polarization are given in table-4.4. These values are taken from ref.[13] and then corrected for final state interaction effects [54]. The neutron beam polarizations and the horizontal and vertical asymmetries are given in table 4.5. In the same table the ratio of the horizontal asymmetries from the neutron polarimeter and the CSB proton polarimeter have been summarized. This ratio is fairly constant for both target up and down runs.

As is evident from the table, the horizontal component of the polarization is only a small fraction of the vertical component. This knowledge is important in estimating the systematic error resulting from the spin correlation parameters, $A_{xz}$, and $A_{xx}$, which are due to the coupling of the horizontal($x$) component of the neutron beam spin with the horizontal ($x$) and longitudinal($z$) components of the proton target spin.

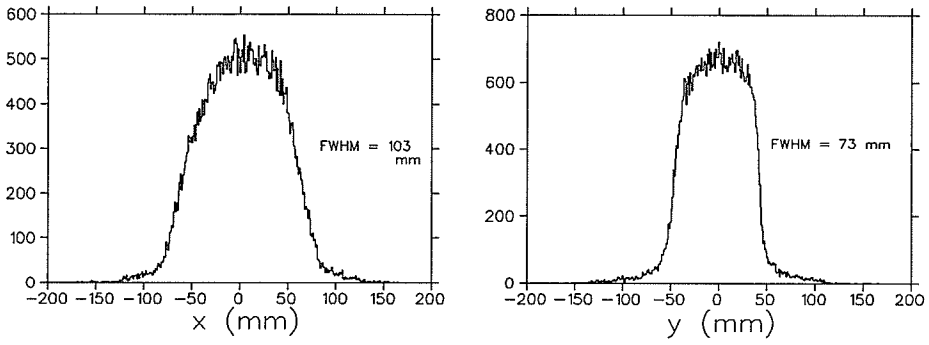


Figure 4.4: (a)Horizontal and (b)Vertical neutron beam profiles at the profile monitor located 16.9 m downstream of the $LD_2$ target.

Table 4.5: Neutron Beam Polarizations Neutron Polarimeter Asymmetries[!]

| Neutron Beam energy (MeV) | Neutron Array angle (deg) | Target spin up | | | | Target spin down | | | |
|---|---|---|---|---|---|---|---|---|---|
| | | Beam polarization | Horizontal asymmetry | Vertical asymmetry | (N/P)POL horizontal asymmetry | Beam polarization | Horizontal asymmetry | Vertical asymmetry | (N/P)POL horizontal asymmetry |
| 424.7 ±2.0 | 67.0 | 0.610 | 0.111 | -0.001 | 0.315 | 0.610 | 0.110 | 0.025 | 0.314 |
| | 61.0 | 0.584 | 0.105 | -0.001 | 0.312 | 0.610 | 0.111 | -0.039 | 0.314 |
| | 57.0 | 0.595 | 0.110 | -0.001 | 0.316 | 0.606 | 0.109 | -0.016 | 0.313 |
| | 52.0 | 0.617 | 0.108 | -0.055 | 0.304 | 0.609 | 0.108 | 0.001 | 0.310 |
| | 47.0* | 0.617 | 0.112 | 0.000 | 0.312 | 0.610 | 0.109 | 0.002 | 0.309 |
| | 47.0# | 0.611 | 0.111 | 0.001 | 0.316 | 0.616 | 0.112 | -0.001 | 0.314 |
| | 37.0 | 0.611 | 0.111 | 0.001 | 0.314 | 0.611 | 0.112 | 0.001 | 0.317 |
| | 27.0 | 0.610 | 0.111 | 0.001 | 0.317 | 0.616 | 0.113 | 0.000 | 0.317 |
| 324.8 ±2.0 | 67.0 | 0.707 | 0.118 | 0.007 | 0.354 | 0.703 | 0.116 | 0.007 | 0.351 |
| | 61.0 | 0.707 | 0.117 | 0.007 | 0.353 | 0.706 | 0.118 | 0.006 | 0.356 |
| | 57.0 | 0.708 | 0.117 | 0.004 | 0.355 | 0.706 | 0.117 | 0.007 | 0.354 |
| | 52.0 | 0.695 | 0.115 | 0.005 | 0.357 | 0.701 | 0.118 | 0.008 | 0.361 |
| | 47.0 | 0.706 | 0.116 | 0.002 | 0.348 | 0.709 | 0.119 | 0.008 | 0.360 |
| | 37.0 | 0.683 | 0.118 | 0.009 | 0.372 | 0.684 | 0.116 | 0.006 | 0.357 |
| | 32.0 | 0.688 | 0.117 | 0.007 | 0.359 | 0.677 | 0.114 | 0.006 | 0.357 |
| 219.6 ±2.0 | 67.0 | 0.722 | 0.086 | 0.005 | 0.315 | 0.736 | 0.089 | 0.001 | 0.320 |
| | 61.0 | 0.721 | 0.087 | 0.005 | 0.320 | 0.741 | 0.089 | 0.004 | 0.318 |
| | 57.0 | 0.719 | 0.088 | 0.003 | 0.325 | 0.737 | 0.089 | 0.009 | 0.321 |
| | 52.0 | 0.715 | 0.086 | 0.003 | 0.318 | 0.750 | 0.088 | 0.012 | 0.312 |
| | 47.0 | 0.715 | 0.087 | 0.004 | 0.320 | 0.740 | 0.089 | 0.008 | 0.320 |
| | 37.0 | 0.743 | 0.087 | 0.007 | 0.315 | 0.737 | 0.091 | 0.008 | 0.332 |

! Typical error in polarization is ±0.002
March 1987 run; # June 1987 run

## 4.2 Analysis of the Profile Events

As mentioned in the previous chapter the neutron profile monitor events were categorized as a specific type of event (event type 3). A total of 22 words were written in each block for this event type. These words contain information on all of the ADCs of the various scintillators and the TDCs of two delay line multiwire proportional wire chambers of the neutron profile monitor. These two wire chambers are used to reconstruct the tracks of the charged particles knocked out of the converter scintillator by the incident neutron beam. The horizontal and vertical profiles of the neutron beam for one of the runs are shown in fig 4.4. The centroids and the width of the neutron beam profiles are summarized in table-4.6. The neutron beam profile at the frozen spin target is roughly 78 mm wide (FWHM) and 56 mm high (FWHM). A displacement of 3 mm of the neutron beam on the target produces an angle error of $0.03^0$ which has virtually no effect on $A_{yy}$ and $A_y$.

## 4.3 Analysis of the n-p Elastic Events

### 4.3.1 Proton Track Reconstruction

The track reconstruction of the recoil protons has been done with the data of the four delay line wire chambers mounted on each proton boom. In the software analysis the first two and the last two chambers are grouped to form two pairs. A valid event must have at least one x- and one y-coordinate in each pair. This arrangement helps to reduce the position error of the track origin while making the overall efficiency very high.

Table 4.6: Centroids and widths of neutron beam profiles at the profile monitor.

| Neutron beam energy (MeV) | Neutron array angle (deg) | Target spin up | | | | Target spin down | | | |
|---|---|---|---|---|---|---|---|---|---|
| | | Y-cent. (mm) | X-cent. (mm) | FWHM (mm) Y | FWHM (mm) X | Y-cent. (mm) | X-cent. (mm) | FWHM (mm) Y | FWHM (mm) X |
| 219.6 ±2.0 | 37.0 | -5.8 | 2.2 | 73.0 | 94.0 | -9.5 | -0.2 | 75.2 | 92.0 |
| | 47.0 | -1.9 | -4.0 | 71.0 | 102.0 | # | 4.7 | 74.5 | 92.0 |
| | 52.0 | -1.4 | -4.0 | 69.3 | 102.0 | 2.4 | -2.5 | 70.5 | 103.4 |
| | 57.0 | -0.3 | -3.3 | 64.6 | 102.2 | 4.6 | -2.2 | 73.0 | 102.2 |
| | 61.0 | 0.02 | -2.7 | 69.3 | 102.2 | -1.6 | -2.3 | 73.0 | 103.4 |
| | 67.0 | 0.4 | -3.4 | 69.3 | 102.0 | -1.3 | -2.8 | 73.0 | 102.2 |
| 324.8 ±2.0 | 37.0 | # | 1.6 | 27.0 | 82.0 | -2.1 | 3.8 | 73.0 | 95.6 |
| | 42.0 | -4.2 | -2.2 | 72.3 | 102.2 | -4.0 | -1.6 | 73.0 | 103.0 |
| | 52.0 | -1.5 | -2.9 | 70.0 | 102.2 | -4.2 | -1.5 | 73.6 | 102.2 |
| | 57.0 | -1.3 | -1.9 | 69.3 | 103.0 | -1.6 | -1.2 | 71.7 | 103.0 |
| | 61.0 | -1.5 | -1.8 | 69.3 | 102.0 | -1.4 | -1.4 | 71.7 | 103.0 |
| | 67.0 | -1.4 | -2.1 | 69.0 | 102.2 | -1.0 | -1.7 | 71.7 | 103.0 |
| 424.7 ±2.0 | 52.0 | -2.1 | -1.9 | 70.0 | 102.2 | -1.4 | -2.4 | 70.0 | 102.2 |
| | 57.0 | -2.0 | -2.1 | 70.0 | 103.4 | -1.5 | -2.3 | 70.5 | 102.2 |
| | 61.0 | -2.2 | -2.1 | 71.7 | 100.0 | -1.4 | -2.2 | 70.0 | 103.0 |
| | 67.0 | -1.9 | -1.8 | 70.0 | 102.2 | -1.8 | -2.2 | 74.0 | 102.0 |

# One of the discriminators was oscillating.

The x- and y-coordinates of the intersection point in each delay line chamber are calculated in the following way. Since the absolute positions of the pulsers are well known from the calibration of the chambers (chapter 2), the apparent x position of the event is determined with respect to the extreme right hand side horizontal pulser position and is given by :

$$x_a = (P_h - \Delta T)\Delta_h + \beta \tag{4.12}$$

where $P_h$ is the channel position of the high (positive channel number) pulser, $\Delta T$ is the time difference between the left and right TDCs, $\beta$ is the offset in mm of the pulser $P_h$ with respect to the extreme right hand side anode wire and $\Delta_h$ is the average horizontal dispersion and is calculated as :

$$\Delta_h = \frac{\Delta X_p}{\Delta C_p} \quad mm/channel \tag{4.13}$$

where $\Delta X_p$ is the separation in mm of the two pulsers on the horizontal delay line and $\Delta C_p$ is the same separation in channel numbers. Because of the nonlinearity in delay line the position $x_a$ is not the true position for the event. In order to know the correct event position a calibration table [66], which relates the absolute spatial position of the anode wire to the channel number in the horizontal time difference spectrum (Chapter 2), has been used. From $x_a$ and using the calibration table the anode wire that is struck is found and the true coordinate is then obtained as :

$$X = 2(n-1) - 290 - x_{off} \quad mm \tag{4.14}$$

where n is the wire number that is struck. The factor 2 accounts for the 2 mm wire spacing. 290 mm is the distance between the central anode wire and the wire at either end; subtracting this factor puts the coordinate at the center of the chamber. $x_{off}$ is the absolute horizontal offsets for the chamber.

The coordinate in the vertical direction is, however, handled differently because of the lack of 'picket fence' structure. Like the horizontal coordinate an apparent vertical coordinate, $y_a$, is determined as:

$$y_a = (\Delta T - P_l)\Delta_v \quad mm \tag{4.15}$$

where $\Delta T$ is the difference in raw TDC values of bottom and top discriminators. $\Delta_v$ is the vertical dispersion in mm/channel. The true vertical coordinate is calculated by adding a position dependent correction to the apparent vertical position. Thus the true vertical position is :

$$Y = y_a + VCOR - 276.25 - y_{off} \quad mm \tag{4.16}$$

where the position dependent correction 'VCOR' is available from the calibration table. The term 276.25 mm, which is exactly half the distance between two pulsers, puts the origin of the vertical coordinate at the center of the chamber.

Once the observed hit positions are determined in the chambers, the particle tracks are traced through each chamber by a linear least square fit. The deviations between the actual hit and the best fit for each chamber are plotted. The constants $x_{off}$ and $y_{off}$ are then adjusted to center the deviation spectra for each chamber around zero. Some of the deviation spectra are plotted in figure 4.5. The horizontal position resolution of each delay line chamber is $\pm 0.6$ mm. The typical vertical resolution is $\pm 0.4$ mm and is better than the horizontal resolution because of the absence of any anode wire in the vertical direction. The efficiency for each chamber is defined as the ratio of number of events detected in a chamber and the total number of triggered events. The overall detection efficiencies, which are the ratio of number of valid events having at least one x- and one y-coordinate in each

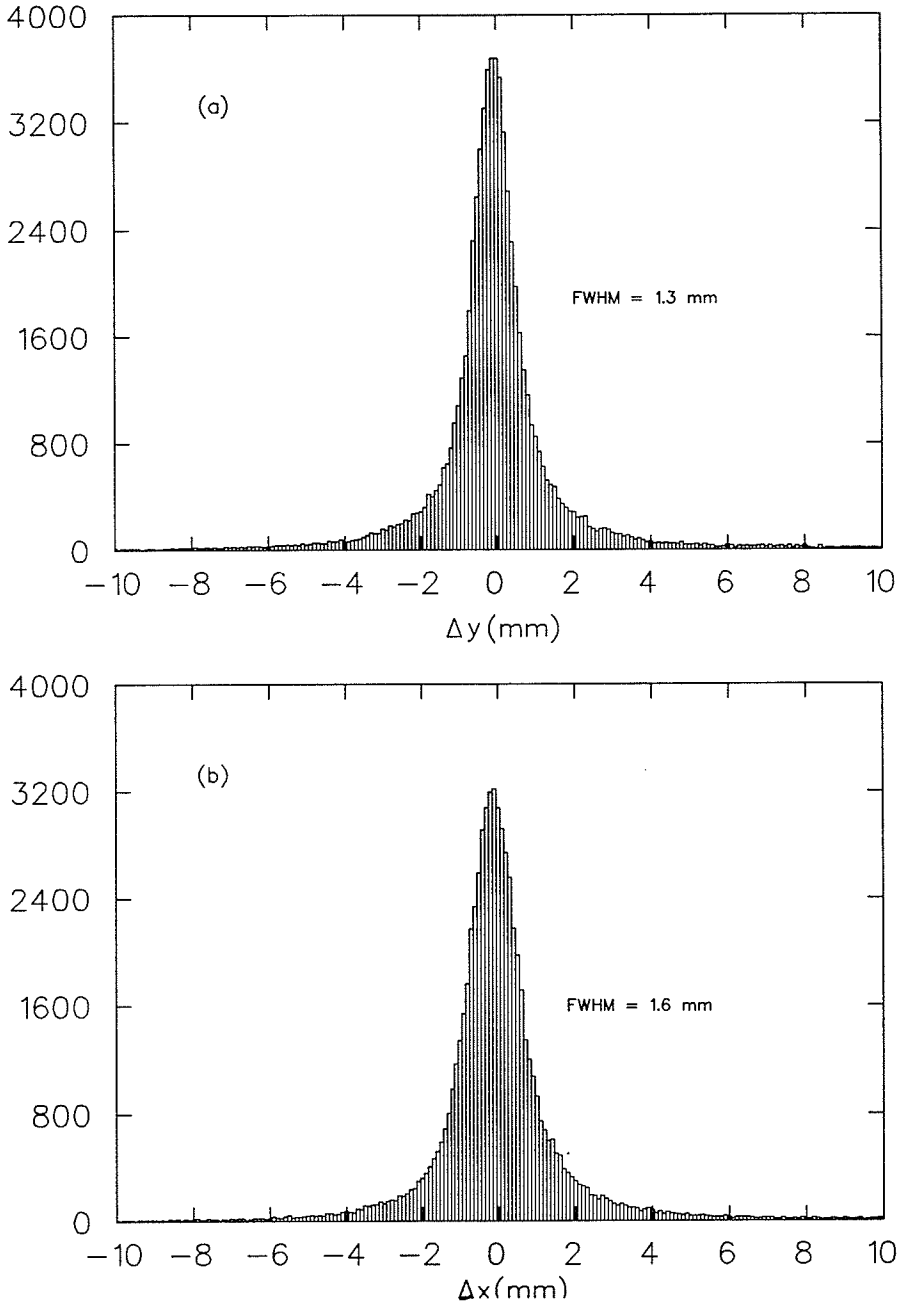


Figure 4.5: (a)Vertical and (b)horizontal position deviations of the third DLC on the left boom.

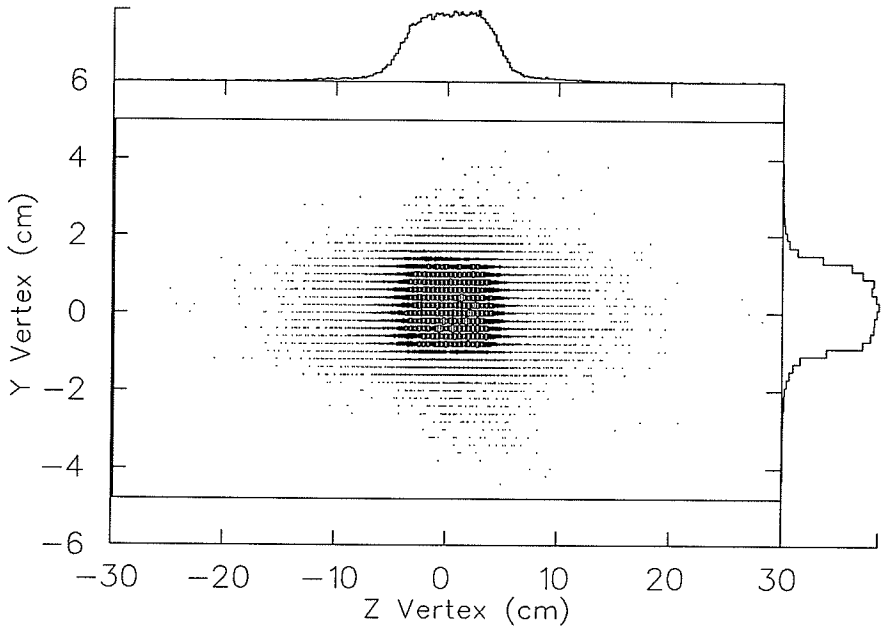


Figure 4.6: Reconstructed y-z vertex

pair of DLCs and the total number of events detected, are listed in table-4.7.

### 4.3.2 Vertex Reconstruction and the Scattering Angles

The vertex reconstruction is done by tracing the proton tracks back to the target. The neutron is assumed to be produced on the axis of the target (i.e. at x=0), the vertical height is taken as the vertical intersection point (y-coordinate) with the proton track. Since the proton scattering angle is determined from the delay line chambers the displacement of the target does not affect the calculated proton angle. The neutron scattering angle is determined by knowing the neutron hit point in the neutron array and the

Table 4.7: Delay Line Chamber overall efficiencies

| Neutron Energy (MeV) | Neutron array angle (deg) | Target spin up | | Target spin down | |
|---|---|---|---|---|---|
| | | Left chambers | right chambers | Left chambers | Right chambers |
| 219.6 ±2.0 | 67.0 | 0.977 | 0.980 | 0.981 | 0.983 |
| | 61.0 | 0.984 | 0.985 | 0.982 | 0.984 |
| | 57.0 | 0.983 | 0.983 | 0.986 | 0.987 |
| | 52.0 | 0.984 | 0.985 | 0.988 | 0.988 |
| | 47.0 | 0.986 | 0.986 | 0.990 | 0.987 |
| | 37.0 | 0.992 | 0.991 | 0.992 | 0.990 |
| 324.8 ±2.0 | 67.0 | 0.951 | 0.967 | 0.957 | 0.970 |
| | 61.0 | 0.966 | 0.974 | 0.970 | 0.977 |
| | 57.0 | 0.973 | 0.976 | 0.975 | 0.979 |
| | 52.0 | 0.977 | 0.979 | 0.973 | 0.978 |
| | 47.0 | 0.973 | 0.972 | 0.969 | 0.974 |
| | 42.0 | 0.975 | 0.973 | 0.973 | 0.972 |
| | 37.0 | 0.971 | 0.980 | 0.982 | 0.978 |
| | 32.0 | 0.986 | 0.982 | 0.990 | 0.980 |
| 424.7 ±2.0 | 67.0 | 0.925 | 0.943 | 0.916 | 0.902 |
| | 61.0 | 0.952 | 0.963 | 0.947 | 0.964 |
| | 57.0 | 0.960 | 0.965 | 0.953 | 0.932 |
| | 52.0 | 0.958 | 0.965 | 0.958 | 0.962 |
| | 47.0* | 0.951 | 0.955 | 0.950 | 0.960 |
| | 47.0# | 0.941 | 0.941 | 0.941 | 0.940 |
| | 37.0 | 0.968 | 0.962 | 0.968 | 0.960 |
| | 27.0 | 0.978 | 0.975 | 0.980 | 0.960 |

* March 1987 run ; # June 1987 run

Table 4.8: Frozen Spin Target Position Offsets

| Run | x-offset (mm) | z-offset ( mm) |
|---|---|---|
| March, 1987 | $-1.0 \pm 1.0$ | $1.0 \pm 1.0$ |
| June, 1987 | $-1.0 \pm 1.0$ | $0.0 \pm 1.0$ |

position of the point of origin of the neutron at the target. The displacement of the target changes the neutron angle and in consequence the opening angle. The exact location of the target cell with respect to the pivot position was determined from the x-ray radiographs taken before and after each phase of the data taking runs. The position offsets of the target cell are summarized in table-4.8. The target center was on the beam plane to within $\pm 1\ mm$. The neutron-proton vertex projected on the y-z plane is illustrated in figure 4.6. The vertex positions are not corrected for the deflection of recoil protons in the target magnetic field. The z-vertex centroid is therefore somewhat shifted from its canonical zero position, in opposite directions for left and right events. The cut on the z-vertex is deliberately kept loose.

Because of the vertical component of the target holding field the recoil protons are deflected horizontally. During the experiment the holding field direction was always up. Thus the proton scattered to the right was deflected towards a larger angle whereas the proton on the left bent towards a smaller angle. In the analysis the proton angles are corrected for the horizontal deflections of recoil protons by adding or subtracting a momentum dependent correction factor to the measured proton angles. The parametric form of this correction factor is determined by simulating the proton tracks through the DLCs in the target holding field. A spline fit is made to the path and the fit is

used to calculate the intersection points with the DLC planes. A least square straight line fit to these points is used to determine the apparent scattering angle of the proton as seen by the DLCs. When the target holding field is 'up' this correction factor is expressed as :

$$\Delta\theta = \frac{698.1}{p\,(MeV/c)} \quad deg. \tag{4.17}$$

where $p$ is the proton momentum. Note that this expression is derived under the assumption that the proton trajectories are always horizontal and the target holding field only has a vertical component. This assumption is adequate because the effect of coupling of the vertical component of the proton velocity to the radial component of the magnetic field is very small. Typically, for a 200 MeV proton and with target holding field 'up' the horizontal deflection is $1.1^0$.

### 4.3.3 Proton Energies

The proton kinetic energies are determined from the time-of-flight between the proton TOF start scintillator and the E scintillator. The timing signal from the TOF scintillator is taken as the software average of the signals from the two ends. Since the scintillator is small (17.5 cm x 17.5 cm) and the interacting region is mostly concentrated around a narrow zone there is no need for a position dependent correction for the signal. However, the E-counter is 67 cm x 67 cm in size and is viewed by four photo-tubes, two at the top and two at the bottom. The timing signal is the average over the number of photo-tubes that fired. For this the E-counter is divided into five regions (fig 4.7). The central region requires all four photo-tubes to fire, whereas the other four regions at the corners require only three photo-tubes to fire. In these four regions the photo-tube on the same 'up-down' side but

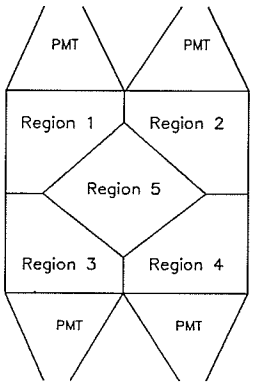


Figure 4.7: Segmentation of the E-counter

on the opposite 'left-right' side with respect to the event position is neglected because the timing information from this photo-tube has been found to be unreliable. This is due to the fact that this particular tube does not 'see' the event well enough.

Because of the large size of the E-counter, timing signals from the E-counter are corrected for the time necessary for the light to travel from the hit position to each photo-tube. This is accomplished by dividing the whole of the E-counter into 18 segments along the x-axis and 28 segments along the y-axis making an 18 x 28 element array. The signal propagation time from each of these 504 elements to the photo-tubes is measured and recorded in a table. In the analysis this correction table is used to subtract the propagation time from the TDC sum of either four or three photo-tubes depending on the hit position. The time-of-flight is the difference in timing signals from the E-counter and the TOF scintillator adjusted for the electronic delays. The energy thus obtained is only the average energy of the proton while in

flight between the start and the stop scintillators. The energy at the center of the target is determined by taking into account the energy losses in the target material. A constant is added to the signal from each of five regions to account for the electronic delays. The value of this constant is determined by forcing the derived proton energies from all of these regions to be the same as kinematically expected values. The proton energy error which is the difference between the energy measured and the energy expected from kinematics is plotted in fig 4.8 for all five regions. Note that all the regions are not equally populated. During the analysis it has been found that a photo-tube corresponding to a less populated region of fig 4.8 quite often cannot 'see' an event (time-out) if the event happens to be in the region diagonally across from the tube. Thus if this event fires three photo-tubes, the tube diagonally across from the event does not give a valid coordinate because of the time out. This way effectively only two photo tubes fire where at least three are needed and thus the event is rejected creating a 'hole' in that region.

### 4.3.4 Neutron Position Determination

The position of a neutron scattered in one of the scintillator bars is determined from the time difference between the two ends of the bar. Since the seven bars in each bank of an array were daisy chained in groups of four and three (chap 2), an appropriate hardware delay was introduced to separate the individual bars in the TDIF spectrum (fig 4.9). The steep dropoff in individual TDIF spectrum signifies the end of the bar. The neutron bar coordinate system is defined in such a way that the positive x-axis increases to the left when viewed along the incident beam direction. Thus for a left event neutron (neutron detected in the left neutron array) smaller x corresponds

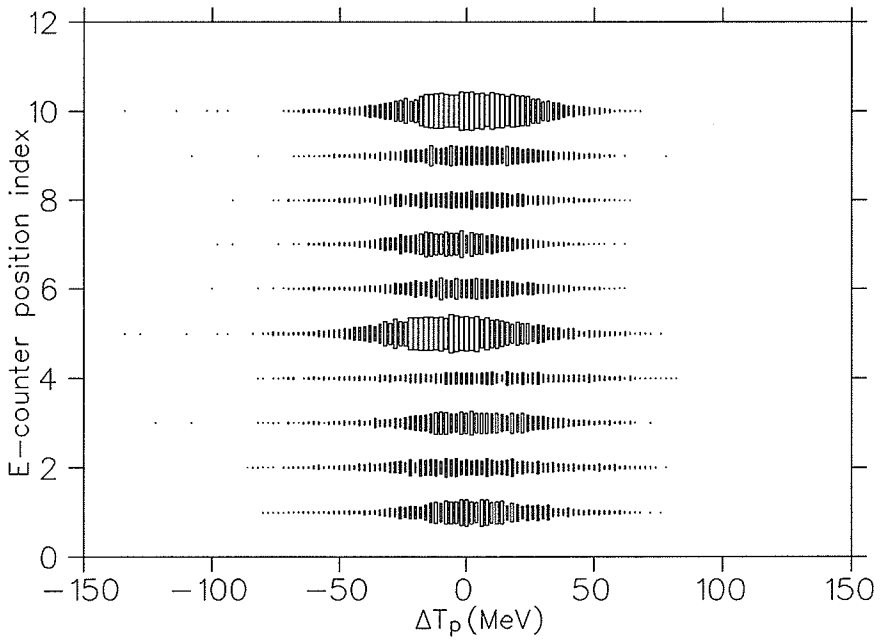


Figure 4.8: The proton energy error vs. the E-counter position index. Index 1-5 stands for the counter on the right boom, the rest are for the counter on the left boom

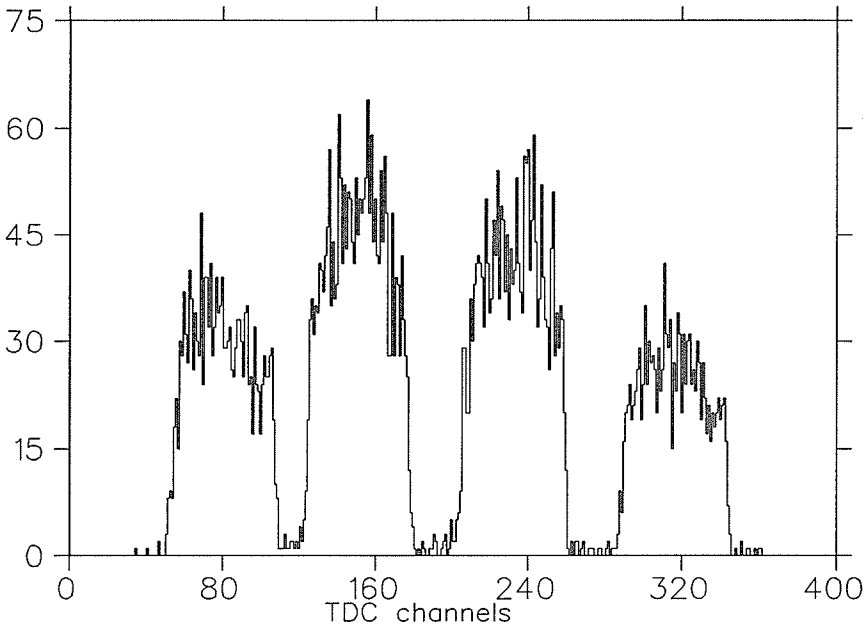


Figure 4.9: TDIF spectrum for a gang of four neutron bars.

to smaller angle. But for the right event neutron it is exactly opposite. The horizontal position of a struck neutron is given by :

$$x_n = \frac{L}{2} - \frac{(T_l - T_s)L}{2\Delta T} \tag{4.18}$$

where $T_l$ and $T_s$ are the TDC values for the large and small angle sides of the neutron bar. $L$ is the physical length of the bar and is equal to 1050 mm. $\Delta T$ is the length of the neutron bar in TDC channel units. This timing width of each bar corresponds to the distance between two points that lie half way down the steep dropoff at the end of each TDIF spectrum. The average length has been found to be equal to 280 TDC channels. When more than one bar in a single bank is hit, the x-coordinate is taken as the average of values for the struck bars. If two non-adjacent bars are hit the event is rejected. If both the back and front banks in an array have a valid x-coordinate, the horizontal position is taken from the front bank, the back

bank is ignored.

The vertical coordinate is assumed to be at the center of the bar if a single bar is hit. When two adjacent bars are hit the y-coordinate is taken at the interface of the two bars. Thus the y-coordinate is expressed as :

$$y_n = (N - 7)75 \ \ mm \tag{4.19}$$

where the factor 7 is for the seven bars in each bank. The factor 75 is half the vertical height of each bar in $mm$. The parameter $N$ is an index which assumes an odd value for a single bar hit. Thus for example, for bar# 1 $N$ is 1 while, for bar# 7 it is 13. When two adjacent bars are hit $N$ becomes even, 2 for bars 1 and 2, 4 for bars 2 and 3 and so on.

Thus for a single bar hit the position resolution in the vertical direction is limited to $\pm 75\ mm$. Like the x-coordinate, the y- coordinate is always taken from the front bank when both banks have valid coordinates. The horizontal position resolution for each bar is estimated to be 32 mm FWHM. This is determined from the difference of button proton positions in front and back bars (fig 4.10).

The button protons are protons which are energetic enough to go through the upstream and downstream banks of the scintillator array to fire seven small 'button' scintillators located at the downstream side of each array. One continously calibrates the neutron bar photomultipliers by looking at the drifts in button protons' pulse heights in each bar. The difference in positions of the actual button proton and the apparent positions determined from the TDIF spectrum is a convenient way to monitor the timing drifts of the neutron bars. However, in the actual experiment at most of the angles and energies, there were no meaningful button events (event type 9) because of the low energy of the recoil protons. During the experiment the drift in

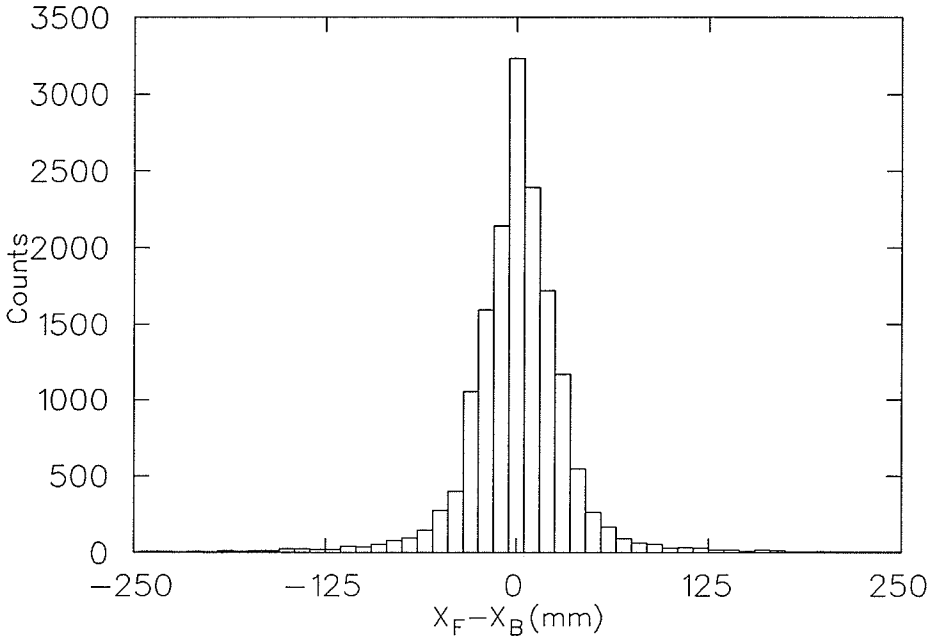


Figure 4.10: The difference of front and back neutron bar horizontal positions for 'button' protons.

neutron bar high voltages was found to be negligible and thus the need for the continous monitoring of the button events was minimal.

### 4.3.5 Neutron Energies

The neutron energy is determined from the neutron time-of-flight between the center of the frozen spin target and the struck neutron bar. The time of flight of the neutron is determined with respect to the coincident proton time-of-flight start counter. Since the proton energy is known, the flight time of the proton from the FST center to the start counter is also known. This time is subtracted from the neutron flight time to give the correct time of flight of the neutron with respect to the target center. The position dependence

of timing in a neutron bar is removed by taking the average time from the opposite ends. The delays in individual bars are adjusted by forcing the neutron energy to approach the kinematically expected energy.

### 4.3.6 Data Constraints

The experimentally measured quantities are the polar and azimuthal angles of the neutron and proton, their kinetic energies and the transverse momentum sum. For a two body scattering any two of the above quantities are sufficient to select the n-p elastic events from the n-np backgrounds. In the present analysis four kinematic constraints are formed. These are :

- The sum of kinetic energies of the neutron and proton : $T_p + T_n$
- The opening angle error : $\theta_p + \theta_n - \theta_{kin}$
- The non-coplanarity angle : $\phi_p + \phi_n - 180^0$
- The x-component of the transverse momentum sum : $P_p \cos\phi_p \sin\theta_p + P_n \cos\phi_n \sin\theta_n$.

Note that $\theta_{kin}$ is the opening angle expected from the kinematics and is expressed as a cubic polynomial of neutron scattering angle. For example, for a 325 MeV incident neutron it is written as :

$$\theta_{kin} = 91.66 - 0.321\theta_n + 0.473.10^{-2}\theta_n^2 - 0.153.10^{-4}\theta_n^3 \ \ deg. \qquad (4.20)$$

where the quadratic and the cubic terms are included to correct for the variation of the opening angle with the scattering angle. Since, in a two body scattering, the recoil and scattered particles azimuthal angles differ by $180^0$, the non-coplanarity angle defined above should be equal to zero. Similarly,

because of momentum conservation, the x-component of the transverse momentum sum is also equal to zero.

The elastic n-p events are selected on the basis of cuts on the sum of $\chi^2$ of the above four variables determined as :

$$\chi^2_{sum} = \sum_{i=1}^{4} \frac{(x_i - < x_i >)^2}{\sigma_i^2} = \sum_{i=1}^{4} \chi_i^2 \tag{4.21}$$

$\sigma_i$ is the measured error in the i'th variable, $x_i$ is the measured value of any of the above four kinematic constraints, $< x_i >$ is the expected value for the same quantity. The measured errors for the $\chi^2_{sum}$ determination, $\sigma_i$, are summarized in table-4.9. A typical plot for the $\chi^2_{sum}$ is illustrated in fig 4.13 with the applied cut shown as well. The above four kinematic variables satisfying $\chi^2_{sum} \leq 10$ for a 325 MeV incident neutron with the neutron array set at $67^0$ is plotted in figures 4.11 and 4.12. The width in the opening angle error comes mainly from multiple scattering of the protons inside the target. The width in the spectrum of non-coplanarity angle is because of the limited vertical position resolution in the neutron bars.

Since the $\chi^2_{sum}$ reconstruction does demand energy and momentum conservation the cut on $\chi^2$ is singularly effective in selecting the free n-p elastic events. However, some additional cuts are also applied to reject some events which would otherwise have evaded the $\chi^2$ cuts. One such cut is demonstrated in fig.4.14 where $\Delta t$ is the difference of measured and expected values of the recoil protons time-of-flight. Note that only 1% of the events would have evaded the $\chi^2$ cuts in absence of any $\Delta t$ cut. However, with the vertex cuts the tail in the above figure goes away. The percentage of events at various angles and energies after applying the $\chi^2_{sum}$, $\Delta t$ and vertex cuts is summarized in the table-4.10. While analysing the data from the first phase of the experiment it was found that the pulser events could not be definitively

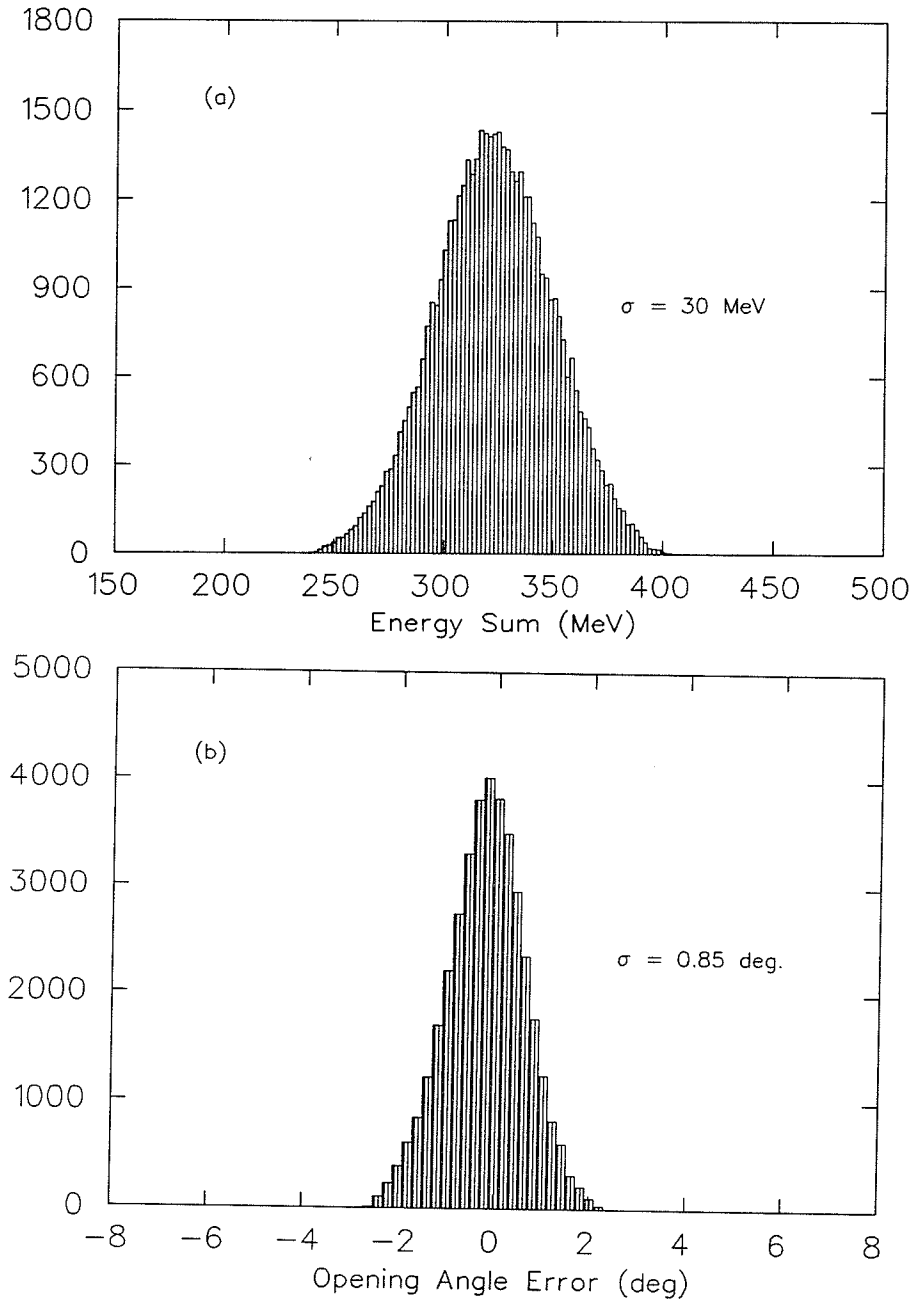


Figure 4.11: (a)Energy sum and (b) Opening angle error for 325 MeV incident neutron with neutron array set at $67^0$.

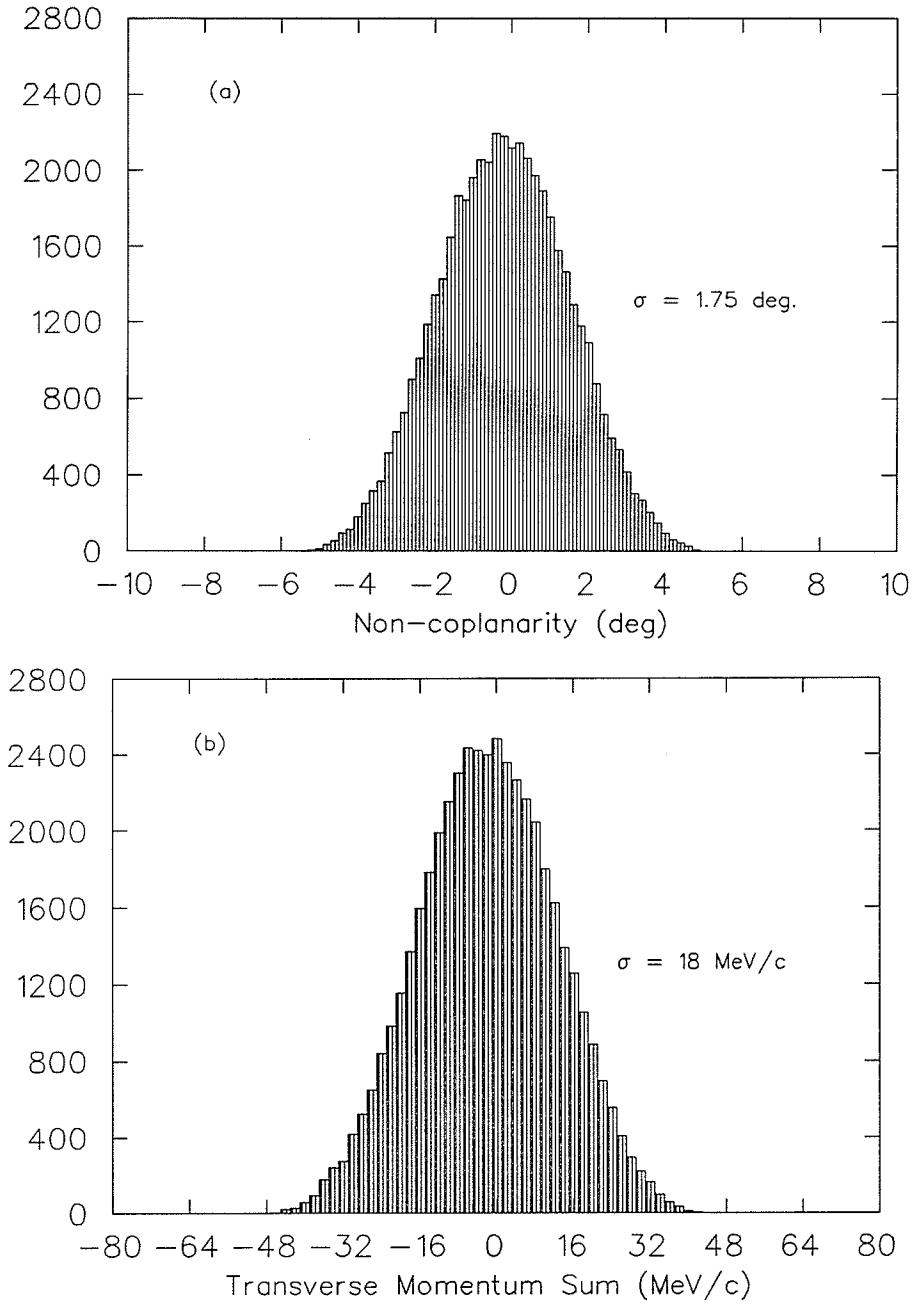


Figure 4.12: (a)Non-coplanarity and (b)x-component of the transverse momentum sum for 325 MeV incident neutron with neutron array set at $67^0$.

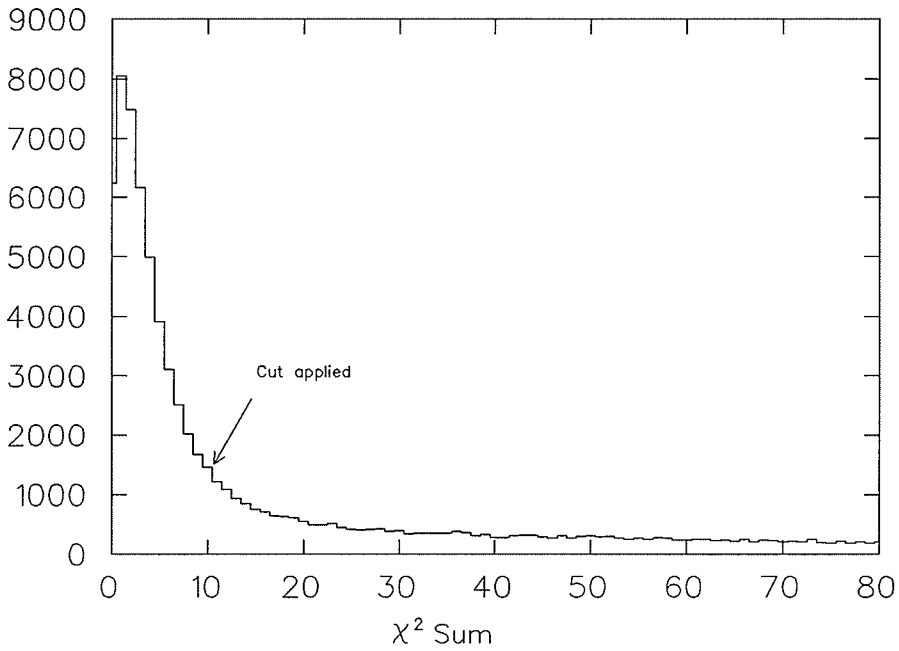


Figure 4.13: Chi-square sum for the four kinematic variables

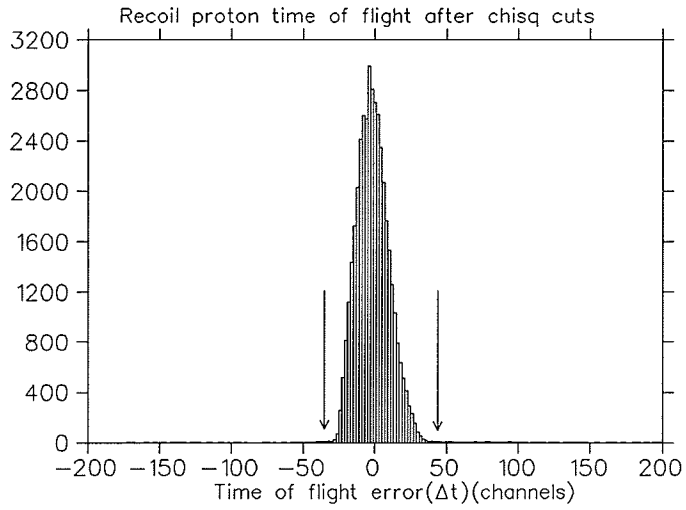


Figure 4.14: $\Delta t$ after the $\chi^2$ cut. The arrows indicate the window for event selection.

Table 4.9: Error estimates for different variables

| Energy MeV | $\theta_n$ deg | $\sigma_{open}$ deg | $\sigma_{copl}$ deg | $\sigma_{ESUM}$ MeV | $\sigma_{P_x}$ Mev/c |
|---|---|---|---|---|---|
| | 67 | 0.77 | 1.70 | 43.0 | 20.0 |
| | 61 | 0.72 | 1.30 | 38.0 | 19.0 |
| | 57 | 0.60 | 1.24 | 37.0 | 20.8 |
| 424.7 | 52 | 0.65 | 1.05 | 25.0 | 16.5 |
| ±2.0 | 47 | 0.60 | 1.05 | 26.0 | 17.0 |
| | 37 | 0.77 | 1.27 | 22.0 | 17.0 |
| | 27 | 1.05 | 1.87 | 22.0 | 18.3 |
| | 67 | 0.85 | 1.75 | 30.0 | 18.0 |
| | 61 | 0.77 | 1.50 | 26.0 | 16.2 |
| | 57 | 0.68 | 1.25 | 23.0 | 15.0 |
| 324.8 | 52 | 0.68 | 1.25 | 20.0 | 15.0 |
| ±2.0 | 47 | 0.68 | 1.28 | 19.0 | 15.0 |
| | 42 | 0.81 | 1.40 | 18.0 | 15.5 |
| | 37 | 0.90 | 1.40 | 15.3 | 16.0 |
| | 32 | 0.94 | 1.80 | 15.0 | 15.0 |
| | 67 | 0.85 | 1.85 | 16.5 | 10.5 |
| | 61 | 0.85 | 1.85 | 14.0 | 11.5 |
| 219.6 | 57 | 0.77 | 1.55 | 13.0 | 11.9 |
| ±2.0 | 52 | 0.85 | 1.50 | 12.5 | 11.0 |
| | 47 | 0.96 | 1.62 | 12.0 | 13.2 |
| | 37 | 1.30 | 1.80 | 11.0 | 13.5 |

identified from the DCR bit alone. However, since the physical locations of the pulsers on the DLCs are well known, the events that fall on the pulser locations are rejected considering them as the pulser events. This method of identifying the pulser events is found to be very effective and compatible with the method of identifying the pulser events on the basis of the pulser bit in the DCR.

Table 4.10: Percentage of events accepted for binning, after all cuts

| $\theta_n$ | Neutron energies (MeV) | | |
|---|---|---|---|
| (deg) | 425 | 325 | 220 |
| 67 | 11.0 | 18.0 | 26.0 |
| 61 | 11.0 | 17.0 | 32.0 |
| 57 | 12.0 | 20.0 | 39.0 |
| 52 | 13.0 | 20.0 | 38.0 |
| 47 | 15.0 | 19.0 | 35.0 |
| 42 | | 21.0 | |
| 37 | 19.0 | 21.1 | 37.0 |
| 32 | | 21.2 | |
| 27 | 27.0 | | |

## 4.4 Background Estimate :

Since there were no separate background runs the estimate of the background is not an easy task. The way the background has been estimated can be summarized in the following three steps.

**Step 1:** The events are selected with $\chi^2_{ESUM} \leq 5, \chi^2_{P_x} \leq 5$ and $|\Delta\phi| \leq 6^0$ (coplanar). The distribution in the opening angle error is plotted under these conditions, a strong elastic peak is observed at $\Delta\theta \simeq 0$ superimposed on top of a broad background distribution.

**Step 2:** The same distribution is plotted for the non-coplanar events selected on the basis of : $\chi^2_{ESUM} \leq 5, \chi^2_{P_x} \leq 5$ and $|\Delta\phi| > 6^0$. These two distributions are then matched to the tails on both sides of the elastic peak. The superposition of these two distributions is shown in fig. 4.15.

**Step 3:** The integrated background events between the limits defined by $\chi^2_{ESUM} \leq 5, \chi^2_{P_x} \leq 5$ and $\chi^2_{\Delta\theta} \leq 5$ cuts on the opening angle error are then calculated for both the above two distributions. The ratio of the number of events within the specified limits of the two distributions gives an estimate

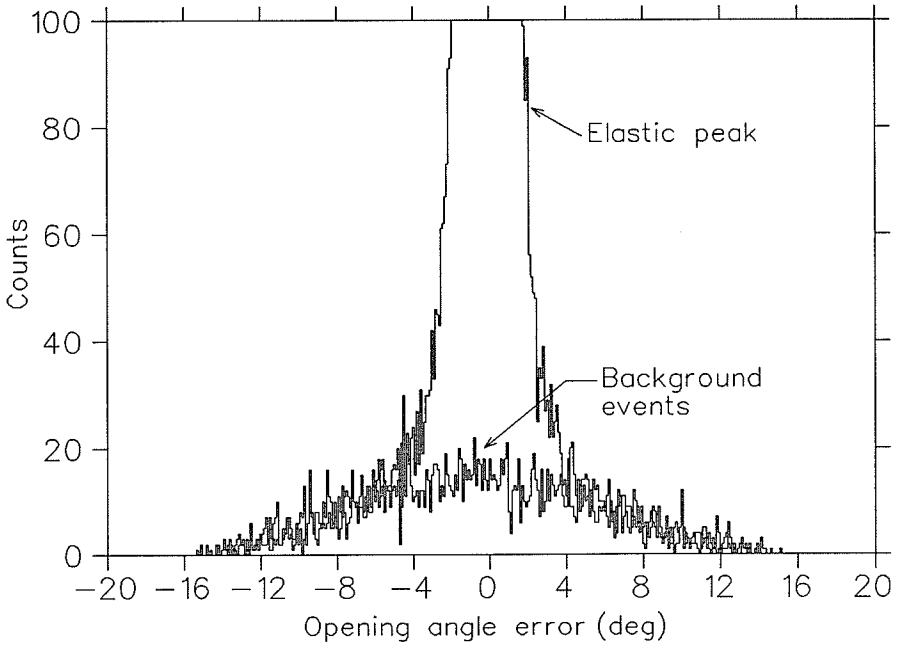


Figure 4.15: Elastic and background peaks in the distribution of opening angle error.

of the background.

The estimated background for 325 MeV incident neutron with the neutron array set at $67^0$ is 3.5%. At the same angle at 425 MeV the background is 5%. This is the worst case scenario. At forward neutron angles and at lower energies the background is 2-3%. The background arising from the accidental coincidences caused by the low energy neutrons arriving at the detector 43 ns (or its multiple) after the elastic neutrons is statistically insignificant, estimated to be $< 0.1\%$ of the elastic neutron events.

# Chapter 5

# Results and Discussions

The analysis of data for each neutron angle setting and for each energy, left and right scattering angles for all possible spin orientations, is carried out for three sets of $\chi^2$ cuts, viz., $\chi^2_{sum} \leq 10$, $\chi^2_{sum} \leq 5$ and $\chi^2_i \leq 5$ (the definitions of different $\chi^2$ can be found in chapter 4). All other cuts are the same as mentioned in chapter 4. Extraction of the spin correlation parameter and analyzing power is done in two steps. First a FORTRAN program called 'READ_SPECTRA' is linked to 'LISA' to extract the contents of different spectra which are then written in an output file. In the second step this output file and a file containing the beam and target polarizations and the beam flux are read in another FORTRAN routine called 'EXTRACT_AYY' which then combines the left and right counts in six different ways to calculate $A_{yy}$ and in two different ways to calculate $A_y$. The different methods of calculating $A_{yy}$ are discussed in Appendix B. In the present chapter, the results quoted are obtained by using the method which is found least sensitive to different systematic errors (Appendix C). In order not to throw away too many elastic events and at the same time to minimize the (n,np) background the final data presented here are from the events satisfying $\chi^2_{sum} \leq 10$ with

all other cuts mentioned in chapter 4. Since the background contamination in the data is very small (chapter 4 and appendix C), the data are not corrected for the background events on a bin by bin basis. Instead, the effect of the remaining background events are studied in appendix C and the systematic error arising from it is calculated. Apart from affecting the statistics, different cuts on the neutron bar pulse height do not have any noticeable effect on $A_{yy}$.

## 5.1 Extraction of the spin correlation parameter, $A_{yy}$

The left and right yields in detectors placed symmetrically around the incident beam direction for polarized beam (first index) and polarized target(second index) are given by :

$$L_{\pm\pm} = NI_{\pm}\Omega_L\epsilon_L\sigma_0(1 \pm A_y(P_B + P_T) + P_BP_TA_{yy}) \quad (5.1)$$

$$R_{\pm\pm} = NI_{\pm}\Omega_R\epsilon_R\sigma_0(1 \mp A_y(P_B + P_T) + P_BP_TA_{yy}) \quad (5.2)$$

$$L_{\pm\mp} = NI_{\pm}\Omega_L\epsilon_L\sigma_0(1 \pm A_y(P_B - P_T) - P_BP_TA_{yy}) \quad (5.3)$$

$$R_{\pm\mp} = NI_{\pm}\Omega_R\epsilon_R\sigma_0(1 \mp A_y(P_B - P_T) - P_BP_TA_{yy}) \quad (5.4)$$

where $\sigma_0$ is the unpolarized cross-section. $P_B$ and $P_T$ are the magnitudes of the beam and target polarizations. $N$ is the number of target protons per unit area. $I$ is the integrated neutron beam flux on the target. $\Omega$ and $\epsilon$ are the solid angle and efficiency respectively. In order to remove systematic errors arising from the different integrated beam fluxes for different beam and target spin orientations the above left-right yields have been normalized

with respect to the primary proton integrated beam flux which can be determined either from the SEM counts or from the corrected CSB polarimeter counts corrected for the accidentals. The SEM counts are sensitive to beam focusing whereas the polarimeter counts are not. However, if the Kapton target in the proton polarimeter was continually depleted of hydrogen then the polarimeter counts would not be very reliable either. During the experiment this possibility was monitored and no evidence of hydrogen loss from the Kapton target was found. In the final analysis, the left-right polarimeter counts are used. As is evident in table 4.7 (chapter 4), the efficiencies of the delay line chambers on the left and right booms differ between two target spin runs. Even though it is not certain whether this dependency has any correlation with the target spin reversal, the present data are corrected for this change in efficiencies.

Since there were two sets of detectors set at equal angles and since there were four different spin combinations, the systematic errors arising from different detector efficiencies, beam normalization and solid angle can be made to cancel in first order (Appendix C). Defining

$$S^2 = \frac{(L_{++} + L_{--})(R_{++} + R_{--})}{(L_{+-} + L_{-+})(R_{+-} + R_{-+})} \tag{5.5}$$

one gets the spin correlation parameter,

$$A_{yy} = \frac{1}{P_B P_T} \frac{(S-1)}{(S+1)} \tag{5.6}$$

the associated error is :

$$\frac{\delta A_{yy}}{A_{yy}} = \sqrt{\left(\frac{\delta P_B}{P_B}\right)^2 + \left(\frac{\delta P_T}{P_T}\right)^2 + \left(\frac{2\delta S}{(S^2-1)}\right)^2} \tag{5.7}$$

where

$$\delta S = S\sqrt{\frac{1}{L_{++} + L_{--}} + \frac{1}{R_{++} + R_{--}} + \frac{1}{L_{+-} + L_{-+}} + \frac{1}{R_{+-} + R_{-+}}}$$

Table 5.1: The spin correlation parameter, $A_{yy}$

| Neutron array angle (deg) | 425 MeV | | | 325 MeV | | | 220 MeV | | |
|---|---|---|---|---|---|---|---|---|---|
| | Central bin (c.m.) | $A_{yy}$ | Stat. error | Central bin (c.m.) | $A_{yy}$ | Stat. error | Central bin (c.m.) | $A_{yy}$ | Stat. error |
| 67 | 146.29 | 0.134 | 0.038 | 145.92 | 0.233 | 0.020 | 144.18 | 0.336 | 0.019 |
| | 141.94 | 0.210 | 0.028 | 141.65 | 0.312 | 0.016 | 140.00 | 0.371 | 0.017 |
| | 137.60 | 0.305 | 0.024 | 137.39 | 0.318 | 0.014 | 135.83 | 0.433 | 0.015 |
| | 133.29 | 0.300 | 0.024 | 133.15 | 0.377 | 0.014 | 131.67 | 0.464 | 0.015 |
| | 129.00 | 0.329 | 0.028 | 128.93 | 0.370 | 0.015 | 127.52 | 0.448 | 0.016 |
| 61 | 135.01 | 0.289 | 0.034 | 134.42 | 0.367 | 0.016 | 132.71 | 0.461 | 0.014 |
| | 130.72 | 0.331 | 0.029 | 130.20 | 0.390 | 0.014 | 128.56 | 0.484 | 0.012 |
| | 126.44 | 0.315 | 0.028 | 125.99 | 0.383 | 0.014 | 124.42 | 0.492 | 0.012 |
| | 122.19 | 0.366 | 0.028 | 121.79 | 0.399 | 0.015 | 120.30 | 0.478 | 0.013 |
| | 117.96 | 0.317 | 0.033 | 117.62 | 0.360 | 0.016 | 116.19 | 0.502 | 0.014 |
| 57 | 127.08 | 0.335 | 0.026 | 126.62 | 0.398 | 0.014 | 124.42 | 0.510 | 0.014 |
| | 122.82 | 0.312 | 0.023 | 122.42 | 0.368 | 0.013 | 120.30 | 0.495 | 0.014 |
| | 118.59 | 0.309 | 0.022 | 118.25 | 0.331 | 0.013 | 116.19 | 0.493 | 0.014 |
| | 114.39 | 0.253 | 0.022 | 114.09 | 0.324 | 0.013 | 112.09 | 0.460 | 0.014 |
| | 110.22 | 0.232 | 0.025 | 109.96 | 0.318 | 0.014 | 108.01 | 0.454 | 0.016 |
| 52 | 117.54 | 0.247 | 0.022 | 116.79 | 0.338 | 0.017 | 114.34 | 0.482 | 0.014 |
| | 113.34 | 0.238 | 0.020 | 112.64 | 0.321 | 0.016 | 110.25 | 0.469 | 0.015 |
| | 109.18 | 0.210 | 0.020 | 108.52 | 0.294 | 0.017 | 106.17 | 0.482 | 0.017 |
| | 105.03 | 0.194 | 0.020 | 104.42 | 0.281 | 0.018 | 102.11 | 0.416 | 0.018 |
| | 100.92 | 0.169 | 0.023 | 100.33 | 0.238 | 0.019 | 98.07 | 0.381 | 0.022 |
| 47* | 107.72 | 0.179 | 0.026 | 106.88 | 0.240 | 0.020 | 104.95 | 0.446 | 0.013 |
| | 103.59 | 0.176 | 0.023 | 102.78 | 0.255 | 0.018 | 100.90 | 0.443 | 0.013 |
| | 99.49 | 0.146 | 0.021 | 98.71 | 0.205 | 0.019 | 96.86 | 0.392 | 0.013 |
| | 95.42 | 0.105 | 0.021 | 94.66 | 0.162 | 0.019 | 92.83 | 0.417 | 0.014 |
| | 91.37 | 0.116 | 0.024 | 90.63 | 0.137 | 0.020 | 88.82 | 0.395 | 0.016 |
| 47# | 105.45 | 0.203 | 0.028 | | | | | | |
| | 101.33 | 0.190 | 0.025 | | | | | | |
| | 97.24 | 0.123 | 0.026 | | | | | | |
| | 93.19 | 0.125 | 0.027 | | | | | | |
| | 89.16 | 0.111 | 0.032 | | | | | | |
| 42 | | | | 96.68 | 0.209 | 0.017 | | | |
| | | | | 92.64 | 0.159 | 0.016 | | | |
| | | | | 88.63 | 0.159 | 0.016 | | | |
| | | | | 84.63 | 0.146 | 0.017 | | | |
| | | | | 80.66 | 0.143 | 0.017 | | | |
| 37 | 87.35 | 0.066 | 0.024 | 88.12 | 0.152 | 0.016 | 83.83 | 0.394 | 0.015 |
| | 83.37 | 0.085 | 0.023 | 82.44 | 0.141 | 0.016 | 79.86 | 0.437 | 0.015 |
| | 79.41 | 0.100 | 0.022 | 78.48 | 0.170 | 0.016 | 75.90 | 0.429 | 0.016 |
| | 75.47 | 0.103 | 0.022 | 74.55 | 0.186 | 0.016 | 71.96 | 0.465 | 0.017 |
| | 71.57 | 0.095 | 0.023 | 70.63 | 0.205 | 0.016 | 68.03 | 0.454 | 0.020 |
| 32 | | | | 74.55 | 0.180 | 0.014 | | | |
| | | | | 70.63 | 0.182 | 0.014 | | | |
| | | | | 66.73 | 0.214 | 0.014 | | | |
| | | | | 62.86 | 0.215 | 0.015 | | | |
| | | | | 59.00 | 0.271 | 0.022 | | | |
| 27 | 65.57 | 0.094 | 0.022 | | | | | | |
| | 61.73 | 0.116 | 0.022 | | | | | | |
| | 57.91 | 0.079 | 0.023 | | | | | | |
| | 54.12 | 0.118 | 0.024 | | | | | | |
| | 50.35 | 0.101 | 0.032 | | | | | | |

* March 1987 runs, # June 1987 runs.

The systematic error in beam polarization is 1.8% where the maximum contribution of 1.5% comes from the uncertainty in the analyzing power of the Kapton target in the proton polarimeter and the rest 1.1% is due to the error in the prediction of $r_t$ (table-4.4). The statistical error in beam polarization is very small, typically 0.002 per tape. The statistical error in target polarization as measured in the calibration part of the experiment is 0.8% whereas the systematic error has been estimated to be 1.7% [58]. For each neutron angle setting data are binned in $2^0$ laboratory angle bins. Since the detectors span about $10^0$ there are five angle bins for each neutron array setting. The spin correlation parameters for all three energies are summarized in table-5.1. Note that the data in this table are derived from the target polarization measured by the NMR system and the beam polarization obtained from using the transfer coefficients given in table-4.4.

## 5.2 Extraction of the Analyzing Power, $A_y$ :

One can also extract the analyzing power either by using the beam or the target polarization as follows :

(a) From Beam Polarization :

$$A_y^b = \frac{1}{P_B}\frac{S_b - 1}{S_b + 1} \tag{5.8}$$

$$S_b^2 = \frac{(L_{++} + L_{+-})(R_{-+} + R_{--})}{(R_{++} + R_{+-})(L_{-+} + L_{--})} \tag{5.9}$$

(b)From Target Polarization :

$$A_y^t = \frac{1}{P_T}\frac{S_t - 1}{S_t + 1} \tag{5.10}$$

$$S_t^2 = \frac{(R_{++} + R_{-+})(L_{--} + L_{+-})}{(R_{--} + R_{+-})(L_{++} + L_{-+})} \tag{5.11}$$

Note that, for any particular angle and for any particular energy, since there were always several days in between target up and down runs the analyzing powers obtained from the target polarization are more susceptible to long term drifts than those obtained from the beam polarization. In Appendix C these two methods of obtaining analyzing powers are compared on the basis of cancellation of different systematic errors. The analyzing powers obtained from using the above two methods are listed in tables 5.2-5.3. Again the target polarization used is the value as measured by the NMR system (table-2.6). For beam polarizations we have used the values listed in the table-4.5.

Table 5.2: The analyzing power, $A_y$, obtained from beam polarization

| Neutron array angle (deg) | 425 MeV | | | 325 MeV | | | 220 MeV | | |
|---|---|---|---|---|---|---|---|---|---|
| | Central bin (c.m.) | $A_y$ | Stat. error | Central bin (c.m.) | $A_y$ | Stat. error | Central bin (c.m.) | $A_y$ | Stat. error |
| 67 | 146.29 | -0.045 | 0.028 | 145.92 | -0.115 | 0.015 | 144.18 | -0.081 | 0.015 |
| | 141.94 | -0.144 | 0.021 | 141.65 | -0.114 | 0.012 | 140.00 | -0.111 | 0.013 |
| | 137.60 | -0.135 | 0.018 | 137.39 | -0.120 | 0.011 | 135.83 | -0.094 | 0.011 |
| | 133.29 | -0.183 | 0.018 | 133.15 | -0.134 | 0.011 | 131.67 | -0.093 | 0.011 |
| | 129.00 | -0.226 | 0.020 | 128.93 | -0.121 | 0.011 | 127.52 | -0.124 | 0.012 |
| 61 | 135.01 | -0.115 | 0.025 | 134.42 | -0.128 | 0.012 | 132.71 | -0.114 | 0.010 |
| | 130.72 | -0.144 | 0.022 | 130.20 | -0.143 | 0.011 | 128.56 | -0.122 | 0.009 |
| | 126.44 | -0.205 | 0.021 | 125.99 | -0.160 | 0.011 | 124.42 | -0.127 | 0.009 |
| | 122.19 | -0.201 | 0.021 | 121.79 | -0.178 | 0.011 | 120.30 | -0.125 | 0.009 |
| | 117.96 | -0.226 | 0.025 | 117.62 | -0.178 | 0.012 | 116.19 | -0.149 | 0.010 |
| 57 | 127.08 | -0.127 | 0.020 | 126.62 | -0.159 | 0.010 | 124.42 | -0.132 | 0.011 |
| | 122.82 | -0.172 | 0.017 | 122.42 | -0.171 | 0.010 | 120.30 | -0.126 | 0.010 |
| | 118.59 | -0.206 | 0.016 | 118.25 | -0.193 | 0.010 | 116.19 | -0.148 | 0.010 |
| | 114.39 | -0.240 | 0.016 | 114.09 | -0.193 | 0.010 | 112.09 | -0.128 | 0.011 |
| | 110.22 | -0.278 | 0.019 | 109.96 | -0.236 | 0.010 | 108.01 | -0.127 | 0.012 |
| 52 | 117.54 | -0.206 | 0.016 | 116.79 | -0.165 | 0.012 | 114.34 | -0.139 | 0.011 |
| | 113.34 | -0.243 | 0.015 | 112.64 | -0.184 | 0.012 | 110.25 | -0.134 | 0.012 |
| | 109.18 | -0.271 | 0.014 | 108.52 | -0.216 | 0.012 | 106.17 | -0.097 | 0.013 |
| | 105.03 | -0.300 | 0.015 | 104.42 | -0.225 | 0.013 | 102.11 | -0.113 | 0.014 |
| | 100.92 | -0.253 | 0.017 | 100.33 | -0.211 | 0.014 | 98.07 | -0.071 | 0.016 |
| 47* | 107.72 | -0.238 | 0.019 | 106.88 | -0.206 | 0.015 | 104.95 | -0.124 | 0.010 |
| | 103.59 | -0.277 | 0.017 | 102.78 | -0.202 | 0.013 | 100.90 | -0.110 | 0.010 |
| | 99.49 | -0.249 | 0.015 | 98.71 | -0.202 | 0.014 | 96.86 | -0.075 | 0.011 |
| | 95.42 | -0.258 | 0.016 | 94.66 | -0.184 | 0.014 | 92.83 | -0.052 | 0.011 |
| | 91.37 | -0.221 | 0.017 | 90.63 | -0.160 | 0.015 | 88.82 | -0.015 | 0.013 |
| 47# | 105.45 | -0.280 | 0.021 | | | | | | |
| | 101.33 | -0.278 | 0.019 | | | | | | |
| | 97.24 | -0.266 | 0.020 | | | | | | |
| | 93.19 | -0.241 | 0.021 | | | | | | |
| | 89.16 | -0.232 | 0.025 | | | | | | |
| 42 | | | | 96.68 | -0.209 | 0.013 | | | |
| | | | | 92.64 | -0.187 | 0.013 | | | |
| | | | | 88.63 | -0.163 | 0.013 | | | |
| | | | | 84.63 | -0.118 | 0.013 | | | |
| | | | | 80.66 | -0.093 | 0.014 | | | |
| 37 | 87.35 | -0.211 | 0.019 | 86.43 | -0.148 | 0.013 | 83.83 | 0.054 | 0.012 |
| | 83.37 | -0.175 | 0.018 | 82.44 | -0.105 | 0.012 | 79.86 | 0.092 | 0.012 |
| | 79.41 | -0.149 | 0.017 | 78.48 | -0.067 | 0.012 | 75.90 | 0.170 | 0.012 |
| | 75.47 | -0.058 | 0.017 | 74.55 | -0.008 | 0.012 | 71.96 | 0.187 | 0.013 |
| | 71.57 | -0.039 | 0.018 | 70.63 | 0.032 | 0.013 | 68.03 | 0.254 | 0.013 |
| 32 | | | | 74.55 | -0.012 | 0.011 | | | |
| | | | | 70.63 | 0.059 | 0.011 | | | |
| | | | | 66.73 | 0.115 | 0.011 | | | |
| | | | | 62.86 | 0.161 | 0.012 | | | |
| | | | | 59.00 | 0.181 | 0.017 | | | |
| 27 | 65.57 | 0.053 | 0.017 | | | | | | |
| | 61.73 | 0.095 | 0.017 | | | | | | |
| | 57.91 | 0.175 | 0.018 | | | | | | |
| | 54.12 | 0.203 | 0.019 | | | | | | |
| | 50.35 | 0.241 | 0.025 | | | | | | |

* March '87 runs, # June '87 runs.

## 5.3 Presentation of final data

There is considerable overlap between angles and thus it is best to combine data in the overlap regions. Since repositioning the arrays altered the solid angle acceptance of the detectors the data in overlapping bins are combined by taking the average weighted by the statistical errors. For each data point, $A_{yy}, A_y^b$ and $A_y^t$ and the associated errors are calculated using the following formulae.

$$A = \frac{\sum_i A_i/\Delta A_i^2}{\sum_i 1/\Delta A_i^2} \tag{5.12}$$

$$(1/\Delta A)^2 = \sum_i (1/\Delta A_i)^2 \tag{5.13}$$

where $A_i$ is either $A_{yy}, A_y^b$ or $A_y^t$. $\Delta A_i$ is the statistical error for each point.

The absolute value of the target polarization is known from the calibration part of the experiment. The target polarization obtained from the proton-proton scattering (calibration) is related to the value obtained from the NMR by the following expression,

$$P_T(scatt) = \mu \; P_T(NMR) \tag{5.14}$$

The factor $\mu$ is found to be equal to $0.961 \pm 0.008(stat) \pm 0.020(sys)$ (appendix A). Thus the analyzing powers obtained from the target polarization are to be multiplied $1/\mu$ i.e., $A_y^t(corrected) = A_y^t(measured)/\mu$. Furthermore, since the analyzing powers obtained from the beam and target polarizations must be the same because of charge symmetry, one can deduce the absolute value of the neutron beam polarization and hence the polarization transfer coefficients $\sqrt{r_t^2 + r_t'^2}$. Equating $A_y^b$ with $A_y^t$ for each data point one gets ,

$$A_y^t(corrected) = \alpha \; A_y^b(measured) \tag{5.15}$$

Table 5.3: The analyzing power, $A_y$, obtained from target polarization

| Neutron array angle (deg) | 425 MeV | | | 325 MeV | | | 220 MeV | | |
|---|---|---|---|---|---|---|---|---|---|
| | Central bin (c.m.) | $A_y$ | Stat. error | Central bin (c.m.) | $A_y$ | Stat. error | Central bin (c.m.) | $A_y$ | Stat. error |
| 67 | 146.29 | -0.075 | 0.033 | 145.92 | -0.101 | 0.019 | 144.18 | -0.064 | 0.019 |
| | 141.94 | -0.106 | 0.024 | 141.65 | -0.102 | 0.015 | 140.00 | -0.118 | 0.017 |
| | 137.60 | -0.147 | 0.021 | 137.39 | -0.128 | 0.014 | 135.83 | -0.121 | 0.015 |
| | 133.29 | -0.202 | 0.021 | 133.15 | -0.136 | 0.014 | 131.67 | -0.103 | 0.015 |
| | 129.00 | -0.222 | 0.023 | 128.93 | -0.132 | 0.015 | 127.52 | -0.095 | 0.016 |
| 61 | 135.01 | -0.099 | 0.027 | 134.42 | -0.132 | 0.015 | 132.71 | -0.115 | 0.013 |
| | 130.72 | -0.147 | 0.024 | 130.20 | -0.160 | 0.014 | 128.56 | -0.119 | 0.012 |
| | 126.44 | -0.222 | 0.023 | 125.99 | -0.179 | 0.014 | 124.42 | -0.125 | 0.012 |
| | 122.19 | -0.245 | 0.023 | 121.79 | -0.188 | 0.014 | 120.30 | -0.141 | 0.012 |
| | 117.96 | -0.196 | 0.027 | 117.62 | -0.203 | 0.015 | 116.19 | -0.141 | 0.014 |
| 57 | 127.08 | -0.081 | 0.022 | 126.62 | -0.161 | 0.014 | 124.42 | -0.141 | 0.014 |
| | 122.82 | -0.182 | 0.019 | 122.42 | -0.181 | 0.013 | 120.30 | -0.131 | 0.013 |
| | 118.59 | -0.248 | 0.018 | 118.25 | -0.208 | 0.012 | 116.19 | -0.137 | 0.013 |
| | 114.39 | -0.265 | 0.018 | 114.09 | -0.219 | 0.013 | 112.09 | -0.152 | 0.014 |
| | 110.22 | -0.306 | 0.021 | 109.96 | -0.239 | 0.014 | 108.01 | -0.105 | 0.016 |
| 52 | 117.54 | -0.153 | 0.018 | 116.79 | -0.194 | 0.016 | 114.34 | -0.147 | 0.014 |
| | 113.34 | -0.222 | 0.017 | 112.64 | -0.214 | 0.015 | 110.25 | -0.138 | 0.016 |
| | 109.18 | -0.266 | 0.016 | 108.52 | -0.206 | 0.016 | 106.17 | -0.145 | 0.017 |
| | 105.03 | -0.308 | 0.017 | 104.42 | -0.219 | 0.017 | 102.11 | -0.127 | 0.019 |
| | 100.92 | -0.328 | 0.019 | 100.33 | -0.234 | 0.018 | 98.07 | -0.087 | 0.022 |
| 47* | 107.72 | -0.257 | 0.022 | 106.88 | -0.222 | 0.019 | 104.95 | -0.143 | 0.012 |
| | 103.59 | -0.277 | 0.018 | 102.78 | -0.250 | 0.017 | 100.90 | -0.108 | 0.012 |
| | 99.49 | -0.275 | 0.017 | 98.71 | -0.242 | 0.018 | 96.86 | -0.094 | 0.013 |
| | 95.42 | -0.279 | 0.017 | 94.66 | -0.197 | 0.018 | 92.83 | -0.053 | 0.014 |
| | 91.37 | -0.283 | 0.019 | 90.63 | -0.162 | 0.019 | 88.82 | -0.026 | 0.015 |
| 47# | 105.45 | -0.250 | 0.021 | | | | | | |
| | 101.33 | -0.275 | 0.019 | | | | | | |
| | 97.24 | -0.251 | 0.020 | | | | | | |
| | 93.19 | -0.278 | 0.020 | | | | | | |
| | 89.16 | -0.241 | 0.025 | | | | | | |
| 42 | | | | 96.68 | -0.219 | 0.015 | | | |
| | | | | 92.64 | -0.194 | 0.015 | | | |
| | | | | 88.63 | -0.177 | 0.015 | | | |
| | | | | 84.63 | -0.142 | 0.015 | | | |
| | | | | 80.66 | -0.073 | 0.016 | | | |
| 37 | 87.35 | -0.216 | 0.019 | 86.43 | -0.141 | 0.014 | 83.83 | 0.047 | 0.015 |
| | 83.37 | -0.155 | 0.018 | 82.44 | -0.087 | 0.014 | 79.86 | 0.109 | 0.015 |
| | 79.41 | -0.119 | 0.017 | 78.48 | -0.074 | 0.014 | 75.90 | 0.161 | 0.016 |
| | 75.47 | -0.072 | 0.017 | 74.55 | 0.003 | 0.014 | 71.96 | 0.235 | 0.016 |
| | 71.57 | -0.019 | 0.018 | 70.63 | 0.037 | 0.015 | 68.03 | 0.270 | 0.019 |
| 32 | | | | 74.55 | -0.001 | 0.012 | | | |
| | | | | 70.63 | 0.054 | 0.012 | | | |
| | | | | 66.73 | 0.115 | 0.012 | | | |
| | | | | 62.86 | 0.155 | 0.013 | | | |
| | | | | 59.00 | 0.206 | 0.019 | | | |
| 27 | 65.57 | 0.079 | 0.017 | | | | | | |
| | 61.73 | 0.111 | 0.017 | | | | | | |
| | 57.91 | 0.166 | 0.018 | | | | | | |
| | 54.12 | 0.191 | 0.019 | | | | | | |
| | 50.35 | 0.205 | 0.025 | | | | | | |

* March '87 runs, # June '87 runs.

The average values of $\alpha$ for three incident energies are found to be equal to, $1.10 \pm 0.03$ at 220, $1.10 \pm .02$ at 325 MeV and $1.06 \pm 0.02$ at 425 MeV. Thus $\alpha$ is the overall normalization factor and all the $A_y^b$'s are multiplied by this factor. The overall normalization factors for $A_{yy}$ are $\alpha/\mu$ or $1.14 \pm 0.04$ at 220 MeV, $1.15 \pm 0.03$ at 325 MeV and $1.10 \pm 0.03$ at 425 MeV.

The weighted average data after normalization by the above factors are listed in tables 5.4-5.6. The errors in the table include only the errors due to counting statistics. The systematic error for each $A_{yy}$ data point at 425 MeV due to the background subtraction error and other possible sources as calculated in Appendix-C is estimated to be 3% at 425 MeV, 2.1% at 325 MeV and 1.7% at 220 MeV. Furthermore the systematic error arising from the error in beam polarization is 1.8% and that from the uncertainty in target polarization is 1.7% at all three energies. Thus the total systematic error is 6.5% at 425 MeV, 5.6% at 325 MeV and 5.2% at 220 MeV. For each data point of $A_y$, the total systematic error from various sources is estimated to be 4.1% at 425 MeV, 3.5% at 325 MeV and 3.1% at 220 MeV.

Neglecting $r_t'$, one gets the transfer coefficient $r_t$ as,

$$r_t(measured) = r_t(used)/\alpha \tag{5.16}$$

At the three incident proton energies the transfer coefficients ($r_t$) at $\theta_n = 9^0$(lab) are, $-0.837 \pm 0.024$ at 228 MeV, $-0.841 \pm 0.016$ at 337 MeV and $-0.803 \pm 0.016$ at 440 MeV. Using Bugg and Wilkin's [54] prescription one gets the transfer coefficients for free n-p scattering ($R_t$) at $9^0$ (lab) as, $-0.798 \pm 0.030$, $-0.795 \pm 0.020$ and $-0.766 \pm 0.020$ at the three energies mentioned above compared to $-0.991 \pm 0.004$, $-0.938 \pm 0.008$ and $-0.849 \pm 0.009$ predicted by the phase shift analysis of Arndt et al. [13].

Figures 5.1-5.3 show the plots of normalized $A_{yy}$ data together with the

predictions from different phase shift analyses and the potential model calculations. LAMPF data on $A_{yy}$ measured at 395 MeV [24] are also shown. At 220 MeV, 325 MeV and 425 MeV Bonn potential predictions are those from the most recent Bonn potential which has been extended beyond the pion production threshold [45], [46]. The extrapolation of the Paris potential up to 425 MeV is somewhat questionable. The present Paris potential predictions obtained from SAID are good up to 350 MeV. However, since the inelasticities in the I=0 channel of the n-p system are small below 1000 MeV, the extrapolation is probably justified. Figs 5.4-5.9 show the analyzing power data along with the 425 MeV data from LAMPF [6] and of the BASQUE group at TRIUMF [7]. At 325 MeV our analyzing power data agree very well with the previous measurement [7] in the intermediate and backward angle range. However, at 220 MeV and also in 425 MeV there appears to be a difference in shape between the present data and the old BASQUE data.

## 5.4 Consistency Checks :

The data for each energy are subjected to several consistency checks. The equality of left and right acceptances are checked by forming a ratio,

$$\eta = \frac{\Omega_L \epsilon_L}{\Omega_R \epsilon_R} \tag{5.17}$$

$$= \left( \frac{L_{++} L_{--} L_{+-} L_{-+}}{R_{++} R_{--} R_{+-} R_{-+}} \right)^{1/4} \tag{5.18}$$

where $\epsilon$ and $\Omega$ are, as defined before, the efficiency and solid angle for the detection system. This ratio in principle should be equal to 1 and be constant over the angles, provided there is no difference in polarization magnitudes between up and down spin states of both target and beam. Now if $P_{B+} \neq P_{B-}$

and $P_{T+} \neq P_{T-}$ then one can show that

$$\eta = \eta_0(\frac{1+\delta(\theta)}{1-\delta(\theta)}) \tag{5.19}$$

where $\delta(\theta)$ is related to the angular dependence of $A_y$ and as well as of $A_{yy}$. However, this dependence is not very large. Furthermore, because of the inequality of the efficiencies in left and right detectors, because of deflections in the target holding field, and because of shadowing of neutron arrays at angles where the proton boom and neutron array overlap this ratio does deviate from 1. Note that data are not rejected on the basis of this parameter. One can also form a ratio of acceptances for target spin up and down runs by defining:

$$\beta = \frac{G_+(\theta)}{G_-(\theta)} \tag{5.20}$$

$$= \left(\frac{L_{++}L_{-+}R_{++}R_{-+}}{R_{+-}R_{--}L_{+-}L_{--}}\right)^{1/4} \tag{5.21}$$

The constancy of this parameter shows that the product of left-right acceptances did not change between two target spin runs. These two ratios are plotted in figs 5.10 and fig 5.11 for 325 MeV neutron data.

## 5.5 Analyzing power zero crossing angles

By least square fitting the analyzing power data from beam polarization to a straight line over $55^0 - 85^0$, the zero crossing angles are extracted for all three energies. The zero crossing angles together with the errors are presented below (table 5.7). Note that the error due to the uncertainty in beam energy is not included in the data. The energy dependence of the zero crossing angle is evident from fig 5.12. The IUCF zero crossing angle is from ref. [23]. The LAMPF data on zero crossing angle are from the thesis

of R. Newsom [6]. The zero crossing angle at 477 MeV has been measured recently with very high precision in a charge symmetry breaking experiment [53]. This datum is also included in the figure.

## 5.6 Spinka Amplitudes at $90^0$ c.m.

In chapter 1 various spin observables in terms of the Spinka amplitudes were defined. The I=1 amplitudes allow one to determine the I=0 amplitudes at any angle $\theta$ from the measurement of six spin observables, $d\sigma/d\Omega$, $P$, $A_{zx}$, $A_{yy}$, $A_{xx}$ and $A_{zz}$ at one energy and angles $\theta$ and $\pi - \theta$ up to a 4-fold ambiguity. However, at $\theta = \pi/2$ three I=0 amplitudes viz., $\phi_s$, $\phi_t$ and $\phi_T$ vanish leaving only two amplitudes to be determined. At $\theta_{c.m.} = 90^0$ the following relations hold,

$$A_{yy} + A_{xx} + A_{zz} = 1 \tag{5.22}$$

$$A_{xx} = A_{zz} = (1 - A_{yy})/2 \tag{5.23}$$

The magnitudes of two I=0 amplitudes, $\phi_\tau$ and $\phi_5$ are related to $A_{yy}$ by the following expressions.

$$|\phi_\tau|^2 = \frac{(1 - A_{yy})}{2}\left(\frac{d\sigma}{d\Omega}\right) \tag{5.24}$$

$$|\phi_5|^2 = \frac{(1 + A_{yy})}{4}\left(\frac{d\sigma}{d\Omega}\right) \tag{5.25}$$

The calculated magnitudes from our present data are summarized in table 5.8. The differential cross section values are taken from the single energy solutions of SP88 version of SAID[13]. Fig 5.13 shows the magnitudes of these two amplitudes obtained from equations 5.24 and 5.25 using the data from present experiment and the phase shift predictions of SP88.

## 5.7 Effect on Phase Parameters

To see the effect of our data on different n-p phases Arndt's scattering analysis program, SAID [13] has been used. The present $A_{yy}$ data with a normalization error of $\pm 0.03$ have been incorporated into the SP88 version of SAID. As expected, at all three energies $^1P_1$, $^3D_2$ and $\epsilon_1$ are affected most strongly by the present data. This version of Arndt's scattering analysis program (SP88) [13] also includes preliminary data on $D_t/R_t$ measured at TRIUMF by the present group [67]. The inclusion of $D_t/R_t$ data shows a large effect on $\epsilon_1$, $^3S_1$, $^3D_1$ and $^3D_2$ phases. To see the effect of $A_{yy}$ data without the $D_t/R_t$ data, the phase shifts predicted from the SM87 version of SAID are also shown in fig 5.14. This version does not include the $D_t/R_t$ data. As shown in figs 5.15-5.16 inclusion of $A_{yy}$ also reduces the phase errors considerably.

Because of its importance, the mixing parameter, $\epsilon_1$, is plotted separately in fig 5.17. Note that beyond 200 MeV, the Bonn and Paris potential predictions diverge from each other. Besides the $\epsilon_1$ obtained from the present data and SM87, the low energy preliminary Karlsruhe data of Klages et al. [22] are also included in the figure. At low energy, the Karlsruhe data has improved the situation for $\epsilon_1$ considerably, but still the remaining uncertainties are large [22] and thus are unable to select one potential model from the other. Our data together with SM87 at higher energy clearly support the Paris Potential predictions of $\epsilon_1$.

Fig 5.18 shows the plot of $^3D_2$ phase obtained from different predictions and our data. The $^3D_2$ phase predicted in the Paris potential [39] is considerably greater than the predictions from the Bonn potentials[38,45] and the phase shift analyses at all energies from 200 to 500 MeV. As is evident

Table 5.4: 425 MeV data

| Angle (c.m.) | $A_{yy}$ | Error | $A_y^b$ | Error | $A_y^t$ | Error |
|---|---|---|---|---|---|---|
| 52.24 | 0.130 | 0.021 | 0.230 | 0.017 | 0.216 | 0.016 |
| 57.92 | 0.095 | 0.018 | 0.175 | 0.015 | 0.166 | 0.014 |
| 63.65 | 0.114 | 0.018 | 0.077 | 0.014 | 0.103 | 0.014 |
| 74.50 | 0.098 | 0.018 | -0.060 | 0.014 | -0.065 | 0.014 |
| 80.40 | 0.102 | 0.018 | -0.161 | 0.014 | -0.133 | 0.014 |
| 86.36 | 0.085 | 0.019 | -0.217 | 0.015 | -0.206 | 0.015 |
| 91.75 | 0.134 | 0.017 | -0.238 | 0.013 | -0.283 | 0.013 |
| 96.06 | 0.119 | 0.015 | -0.276 | 0.012 | -0.290 | 0.012 |
| 100.87 | 0.187 | 0.013 | -0.277 | 0.010 | -0.286 | 0.010 |
| 105.20 | 0.205 | 0.013 | -0.300 | 0.010 | -0.291 | 0.010 |
| 109.61 | 0.242 | 0.015 | -0.284 | 0.011 | -0.289 | 0.012 |
| 113.87 | 0.268 | 0.015 | -0.256 | 0.011 | -0.252 | 0.012 |
| 118.18 | 0.315 | 0.014 | -0.223 | 0.011 | -0.209 | 0.012 |
| 122.77 | 0.364 | 0.017 | -0.197 | 0.013 | -0.215 | 0.014 |
| 127.64 | 0.362 | 0.017 | -0.182 | 0.013 | -0.171 | 0.014 |
| 132.28 | 0.344 | 0.019 | -0.179 | 0.014 | -0.183 | 0.015 |
| 136.79 | 0.336 | 0.020 | -0.147 | 0.015 | -0.145 | 0.017 |
| 143.57 | 0.198 | 0.023 | -0.117 | 0.017 | -0.089 | 0.020 |

from fig 1.3, this over prediction of $^3D_2$ phase is the most probable cause of large deviation of the Paris potential predictions of $A_{yy}$ from the data near $90^0$(c.m.). Regarding this phase shift the extended Bonn potential does a better job.

The analyzing power data are also included separately in the program, SAID. Some of the phases are affected, however, the effect is not very large. Unfortunately, the combined effect of $A_{yy}$ and $A_y$ on the phases can not be seen using the program SAID because there is no provision of putting two different sets of data together. The effect of $R_t$ data (page 124) on different phases is also investigated. It is found that at 325 MeV the $^1P_1$, $^3S_1$ and $^3D_3$ phases are changed by 0.14 deg., 0.11 deg., and 0.10 deg. respectively by the addition of $R_t$ data in the present data base of SAID.

## 5.8 Further Measurements

It has been demonstrated by Chulick et al. [12] on the basis of 1987 data base that the coupling parameter, $\epsilon_1$, is poorly constrained between $1^0$ and $7^0$ at 325 MeV. The present $A_{yy}$ data together with the $D_t/R_t$ data [67] constrain this parameter to a large extent. However, a very high precision ($\leq$ 1%) measurement of $D_t$ at some other energies can further pin down the $\epsilon_1$ parameter. This parameter is fundamentally important because of its dependence on the tensor component of the NN interaction. Above 400 MeV, the Saclay-Geneva phase shift analysis predicts this parameter to drop, from a few deg at 400 MeV to $-10^0$ at 800 MeV. This is completely contradictory to Arndt's predictions. In figs 5.19-5.20 the angle energy correlation of the difference in predictions of different spin observables based on two different phase shift analyses are plotted. As is evident, even at intermediate energies

Table 5.5: 325 MeV data

| Angle (c.m.) | $A_{yy}$ | Error | $A_y^b$ | Error | $A_y^t$ | Error |
|---|---|---|---|---|---|---|
| 61.89 | 0.259 | 0.013 | 0.179 | 0.010 | 0.173 | 0.011 |
| 67.92 | 0.237 | 0.011 | 0.113 | 0.008 | 0.102 | 0.009 |
| 72.59 | 0.214 | 0.009 | 0.011 | 0.007 | 0.017 | 0.008 |
| 77.18 | 0.193 | 0.012 | -0.054 | 0.009 | -0.037 | 0.010 |
| 82.05 | 0.171 | 0.010 | -0.105 | 0.008 | -0.097 | 0.009 |
| 86.82 | 0.165 | 0.011 | -0.161 | 0.009 | -0.155 | 0.010 |
| 91.14 | 0.177 | 0.013 | -0.184 | 0.010 | -0.184 | 0.011 |
| 95.16 | 0.203 | 0.012 | -0.215 | 0.010 | -0.223 | 0.011 |
| 99.31 | 0.256 | 0.012 | -0.234 | 0.009 | -0.253 | 0.011 |
| 103.86 | 0.314 | 0.012 | -0.235 | 0.009 | -0.241 | 0.011 |
| 108.46 | 0.333 | 0.011 | -0.249 | 0.008 | -0.225 | 0.010 |
| 113.12 | 0.366 | 0.010 | -0.216 | 0.007 | -0.230 | 0.009 |
| 117.59 | 0.392 | 0.009 | -0.197 | 0.006 | -0.212 | 0.008 |
| 122.36 | 0.432 | 0.010 | -0.192 | 0.007 | -0.193 | 0.009 |
| 127.26 | 0.443 | 0.010 | -0.163 | 0.006 | -0.165 | 0.008 |
| 131.67 | 0.445 | 0.011 | -0.151 | 0.008 | -0.146 | 0.010 |
| 135.74 | 0.393 | 0.012 | -0.138 | 0.008 | -0.141 | 0.011 |
| 141.12 | 0.360 | 0.014 | -0.120 | 0.010 | -0.110 | 0.013 |
| 145.92 | 0.266 | 0.020 | -0.127 | 0.014 | -0.107 | 0.018 |

Table 5.6: 220 MeV data

| Angle (c.m.) | $A_{yy}$ | Error | $A_y^b$ | Error | $A_y^t$ | Error |
|---|---|---|---|---|---|---|
| 70.97 | 0.535 | 0.016 | 0.230 | 0.011 | 0.257 | 0.014 |
| 76.89 | 0.503 | 0.015 | 0.168 | 0.010 | 0.162 | 0.012 |
| 82.84 | 0.456 | 0.014 | 0.061 | 0.010 | 0.057 | 0.012 |
| 90.33 | 0.437 | 0.015 | -0.026 | 0.010 | -0.020 | 0.012 |
| 95.35 | 0.458 | 0.014 | -0.075 | 0.010 | -0.085 | 0.012 |
| 99.72 | 0.481 | 0.012 | -0.103 | 0.008 | -0.114 | 0.010 |
| 104.31 | 0.506 | 0.011 | -0.132 | 0.007 | -0.142 | 0.009 |
| 108.86 | 0.536 | 0.012 | -0.132 | 0.008 | -0.133 | 0.010 |
| 113.49 | 0.539 | 0.011 | -0.152 | 0.007 | -0.150 | 0.009 |
| 117.52 | 0.563 | 0.011 | -0.160 | 0.007 | -0.145 | 0.009 |
| 121.84 | 0.562 | 0.012 | -0.132 | 0.007 | -0.145 | 0.009 |
| 125.97 | 0.556 | 0.012 | -0.144 | 0.007 | -0.127 | 0.009 |
| 130.11 | 0.539 | 0.012 | -0.119 | 0.007 | -0.111 | 0.009 |
| 134.12 | 0.515 | 0.013 | -0.116 | 0.008 | -0.127 | 0.011 |
| 139.48 | 0.432 | 0.016 | -0.114 | 0.011 | -0.121 | 0.015 |
| 144.18 | 0.384 | 0.021 | -0.088 | 0.015 | -0.067 | 0.019 |

Table 5.7: Zero crossing angle

| Energy (MeV) | Zero crossing angle in deg. (c.m.) |
|---|---|
| 477* | 69.69±0.33 |
| 425 | 69.48±0.61# |
| 325 | 74.33±0.35# |
| 220 | 89.02±0.63# |

* Charge symmetry breaking experiment [53]. # The error in beam energy is not included.

there are large differences between these two predictions for almost all the spin observables. At higher energies (> 500 MeV) the situation is worse. No doubt a more complete data base for n-p system is required for unique phase shift solutions.

In order to determine the I=0 imaginary parts of the phase shifts, precise data on the total cross-section in the reaction $np \rightarrow np\pi^0$ using a free neutron beam is highly desirable [3]. Furthermore, the measurement of the difference in the polarized total cross-section, $\Delta\sigma_L$ is very important. For example the energy dependence of $\Delta\sigma_L$ as predicted from the Saclay-Geneva phase shift analysis shows oscillations at energies between 70 and 200 MeV which are unphysical and is due to the lack of precise $\Delta\sigma_L$ data in this energy region [3].

Table 5.8: Spinka amplitudes

| Energy (MeV) | $A_{yy}$ at $90^0$ (c.m.) | $d\sigma/d\Omega$ mb/sr from SAID * | $\|\phi_\tau\|^2$ mb/sr | $\|\phi_5\|^2$ mb/sr |
|---|---|---|---|---|
| 425 | 0.113±0.013 | 1.36±0.01 | 0.603±0.010 | 0.378±0.005 |
| 325 | 0.172±0.015 | 1.47±0.01 | 0.609±0.012 | 0.431±0.006 |
| 220 | 0.435±0.014 | 1.69±0.012 | 0.477±0.012 | 0.606±0.007 |

* Fixed energy solutions e.g.C200, C300 and C400

## 5.9 Conclusions

The spin correlation parameter $A_{yy}$ and the analyzing powers $A_y$ have been measured with absolute accuracy of ±0.03 in n-p elastic scattering. Prior to this measurement there were no $A_{yy}$ data available over a wide range of intermediate energy (200-390 MeV). The 220 MeV $A_{yy}$ data agree quite well with the extended Bonn potential prediction in the intermediate and backward angle range. At 325 MeV the shape of the angular distribution of $A_{yy}$ closely resembles the extended Bonn potential prediction, however, the absolute values are different. The longstanding problem with the difference in measured values of 425 MeV $A_y$ is somewhat resolved. It may not be apparent from the figure, however, a renormalization of the LAMPF data [6] by 0.9 brings the LAMPF values very close to the present measurement, both in magnitude as well as in shape. Thus it seems that the normalization for the LAMPF measurement was not properly estimated. Because of the difference in shape there is no way one can renormalize the BASQUE data to fit the present measurement. Also at the backward angles at 325 MeV the BASQUE $A_y$ data show a significant deviation from the present data and

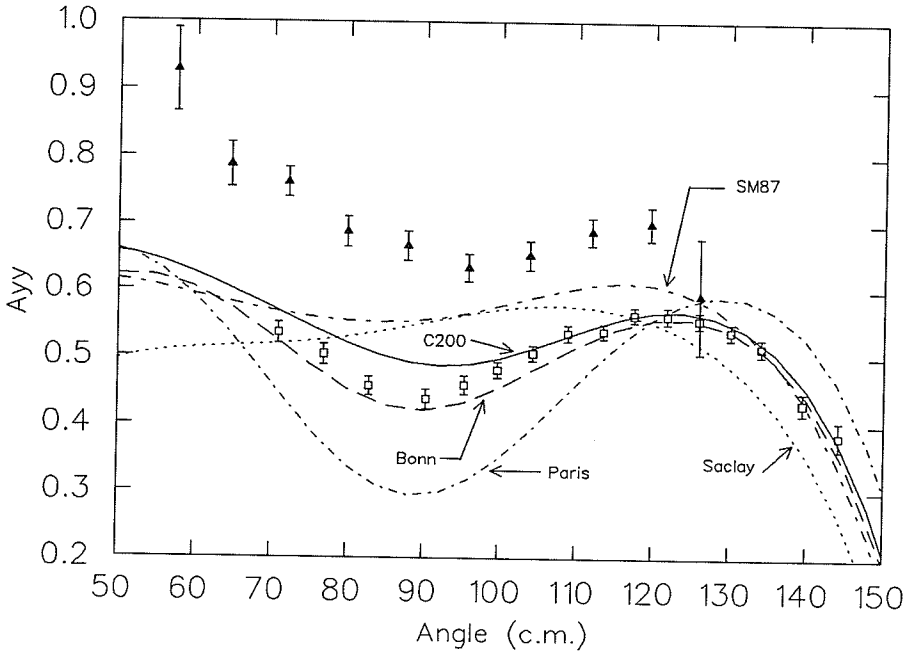


Figure 5.1: $A_{yy}$ at 220 MeV. The IUCF data at 181 MeV are also included (solid triangles). The Bonn potential prediction is from ref. [47].

also from the phase shift prediction of Arndt et al.

The new data have a great impact on the phase shift parametrization of the I=0 scattering amplitudes. The present set of data will definitely help refine the commonly used nucleon-nucleon potentials such as the Paris and Bonn potentials.

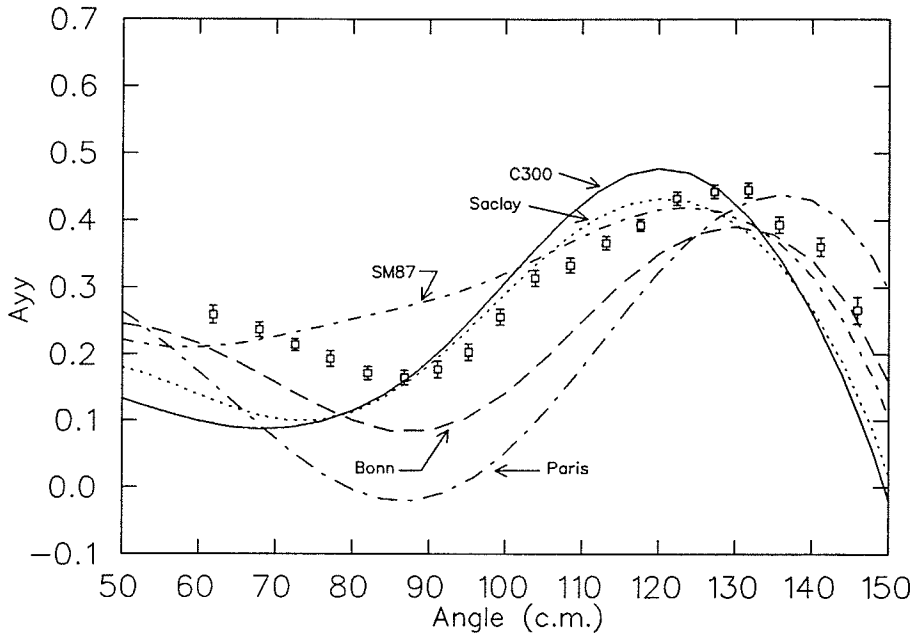


Figure 5.2: $A_{yy}$ at 325 MeV. The Bonn potential prediction is from ref. [47].

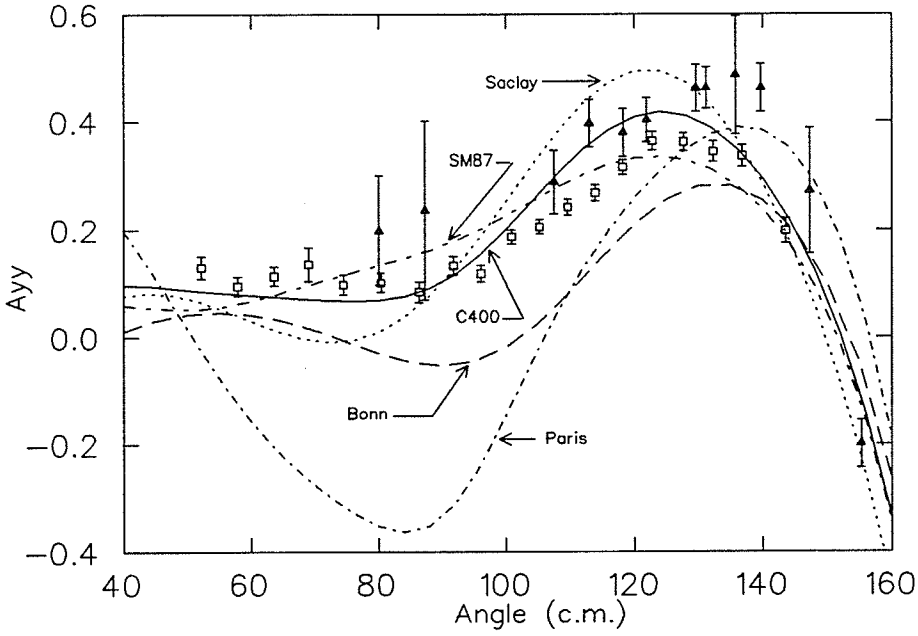


Figure 5.3: $A_{yy}$ at 425 MeV. Solid triangles are LAMPF 395 MeV data. Open squares are the present measurement.

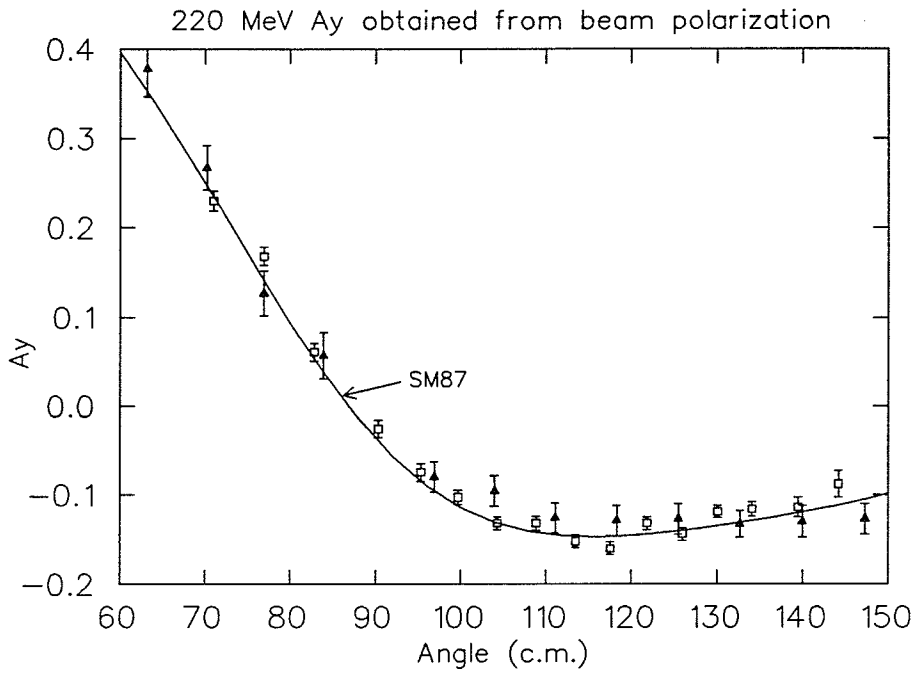


Figure 5.4: $A_y^b$ at 220 MeV. Solid triangles are the previous BASQUE data [7] at 220 MeV.

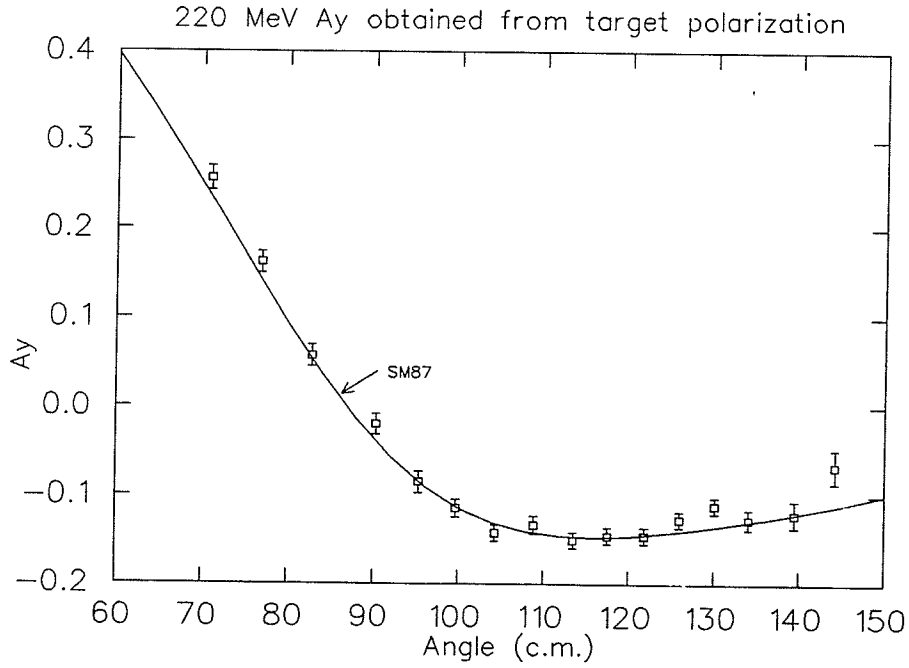


Figure 5.5: $A_y^t$ at 220 MeV.

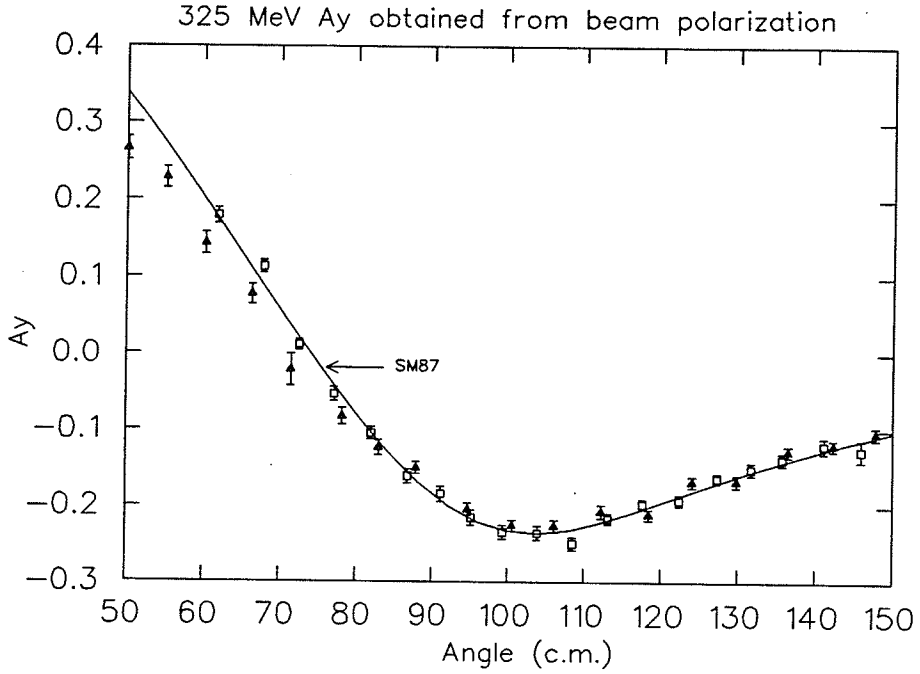


Figure 5.6: $A_y^b$ at 325 MeV. Solid triangles are from previous BASQUE measurement

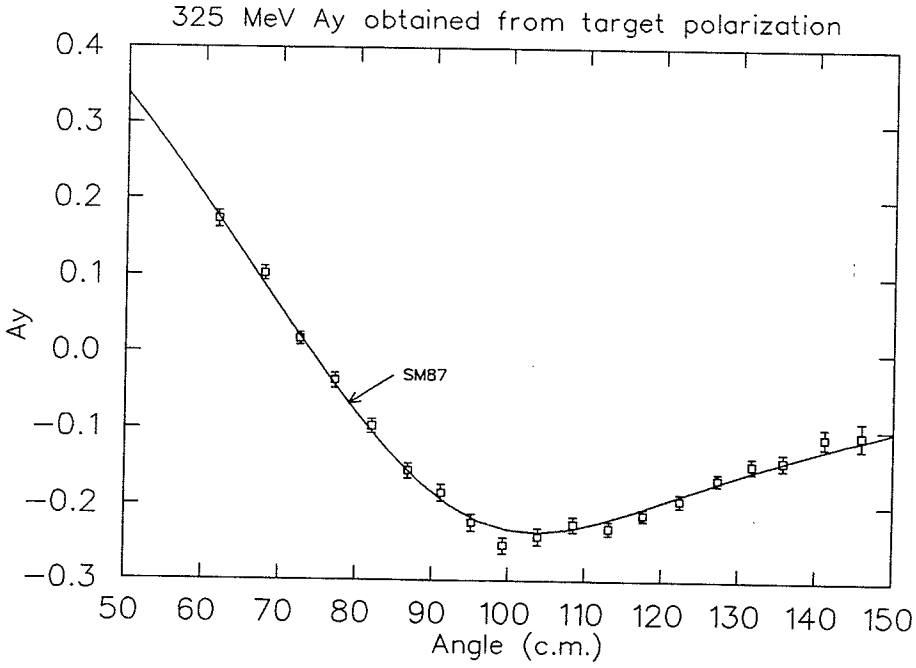


Figure 5.7: $A_y^t$ at 325 MeV.

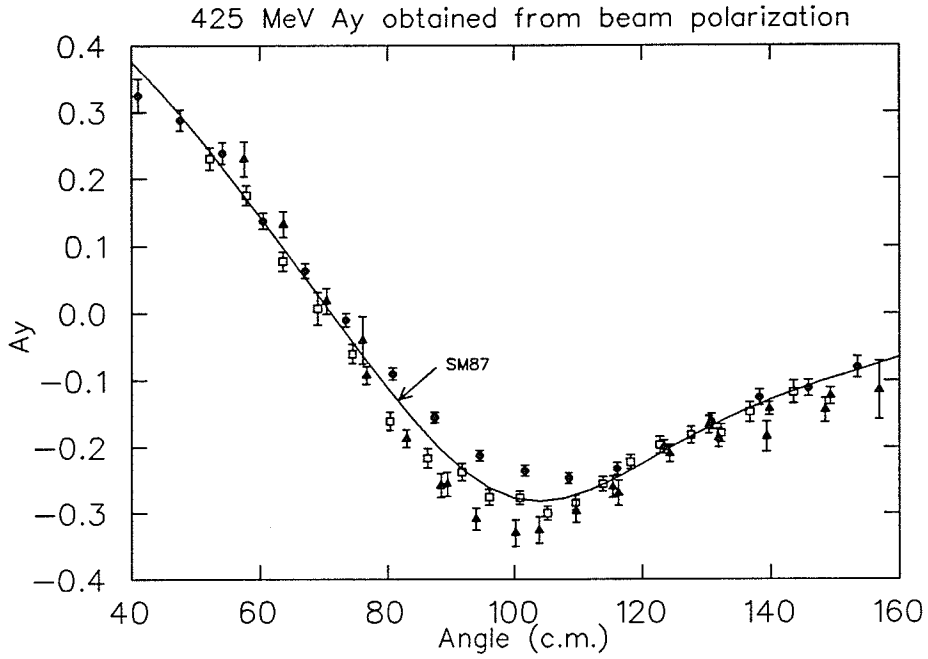


Figure 5.8: $A_y^b$ at 425 MeV. Triangles are the LAMPF data, solid circles are the BASQUE measurement

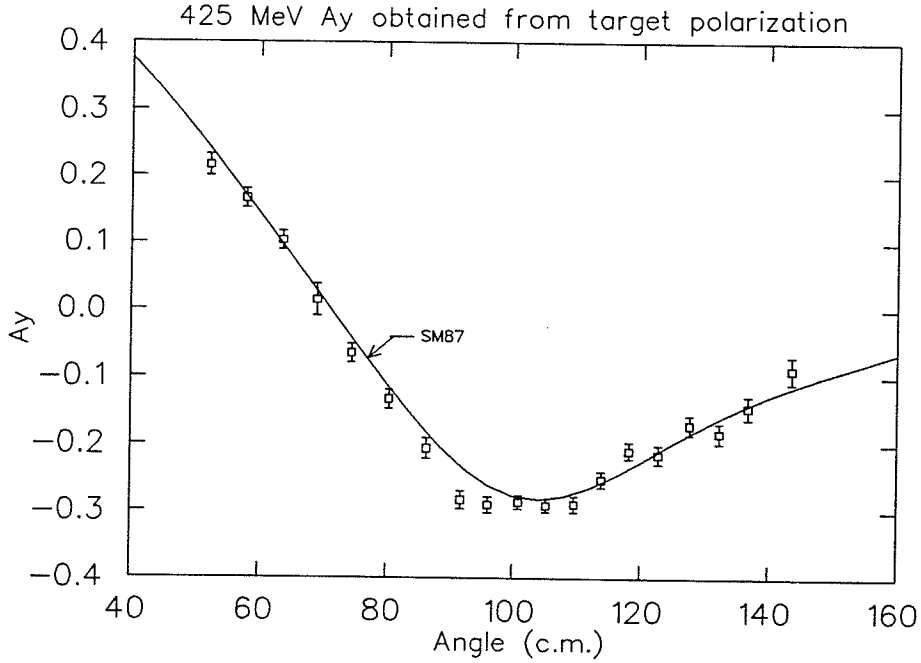


Figure 5.9: $A_y^t$ at 425 MeV

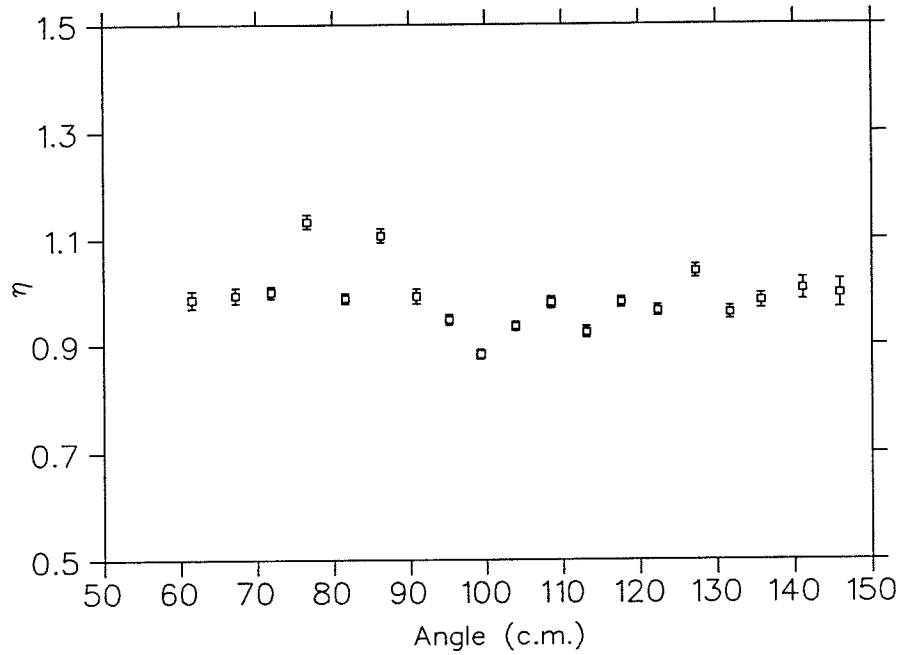


Figure 5.10: Ratio of left-right acceptances

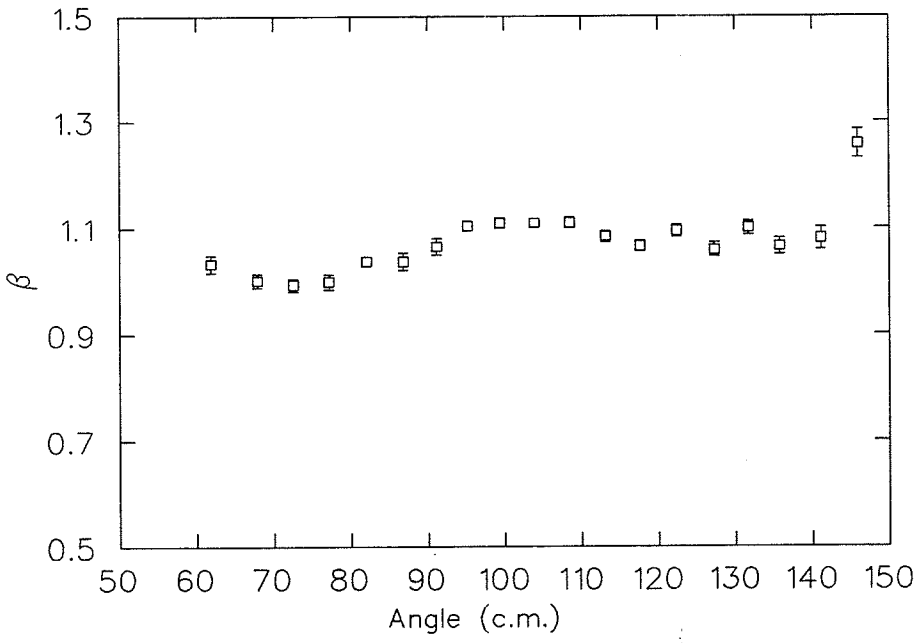


Figure 5.11: Ratio of acceptances for two different target spin orientations.

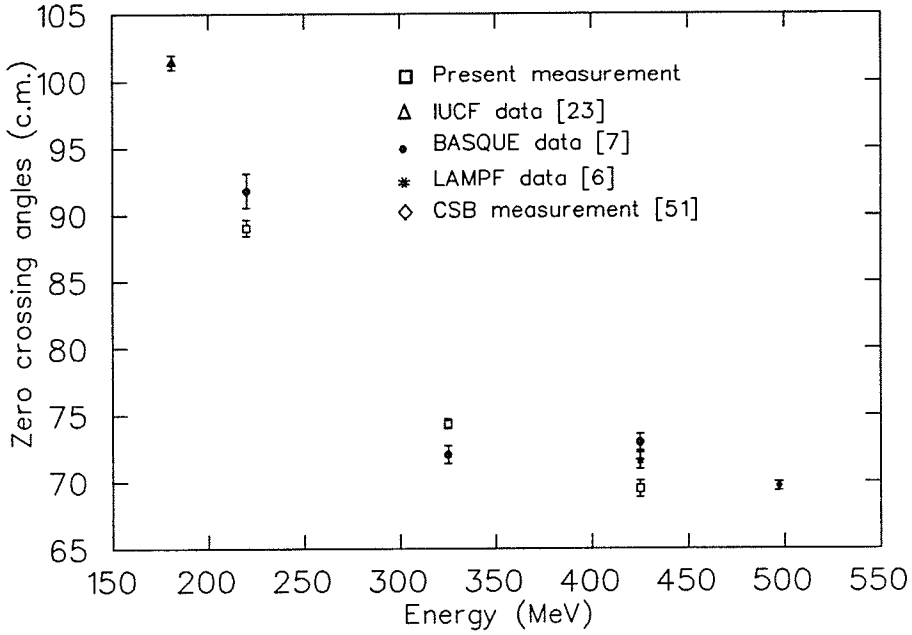


Figure 5.12: Analyzing power zero crossing angles

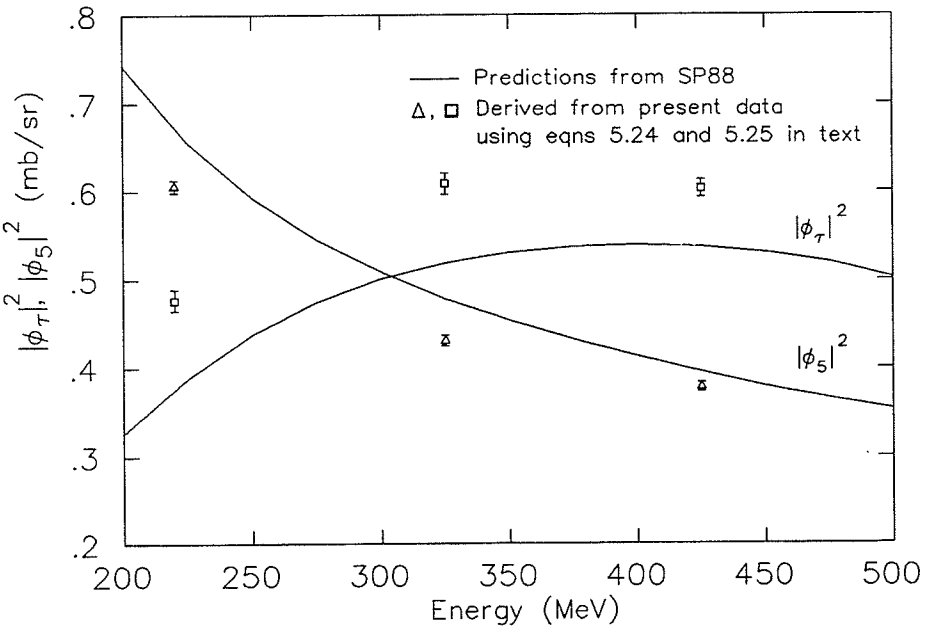


Figure 5.13: Spinka amplitudes at $90^0$ c.m.

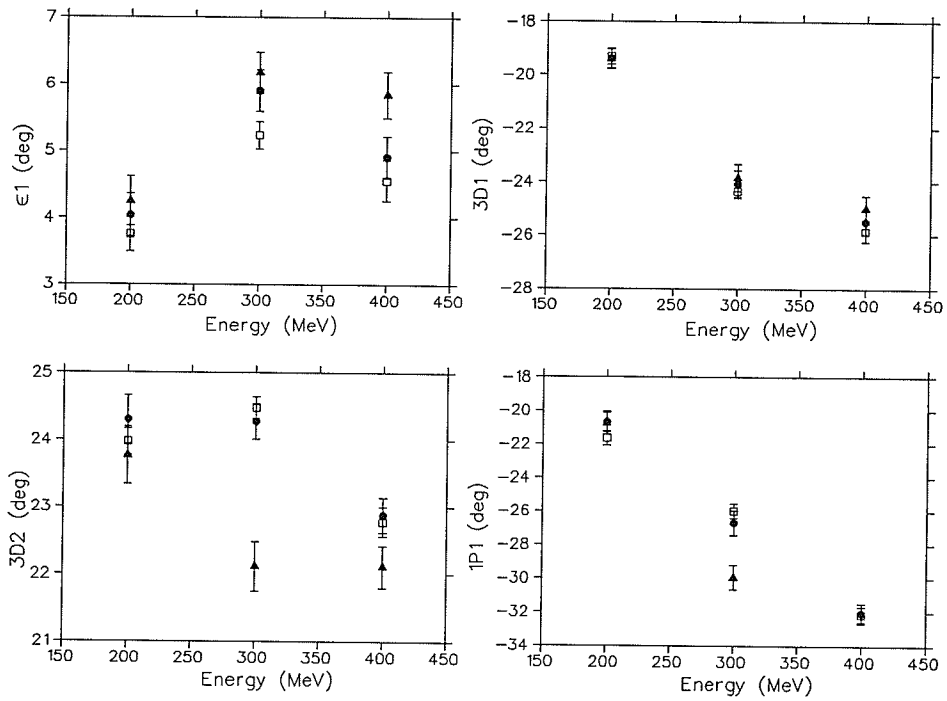


Figure 5.14: Predicted phase shifts without and with the present data. Solid triangle is from SM87, solid circle is from SP88 which also includes Dt/Rt data. Open square is after putting the Ayy data in the SP88 data base.

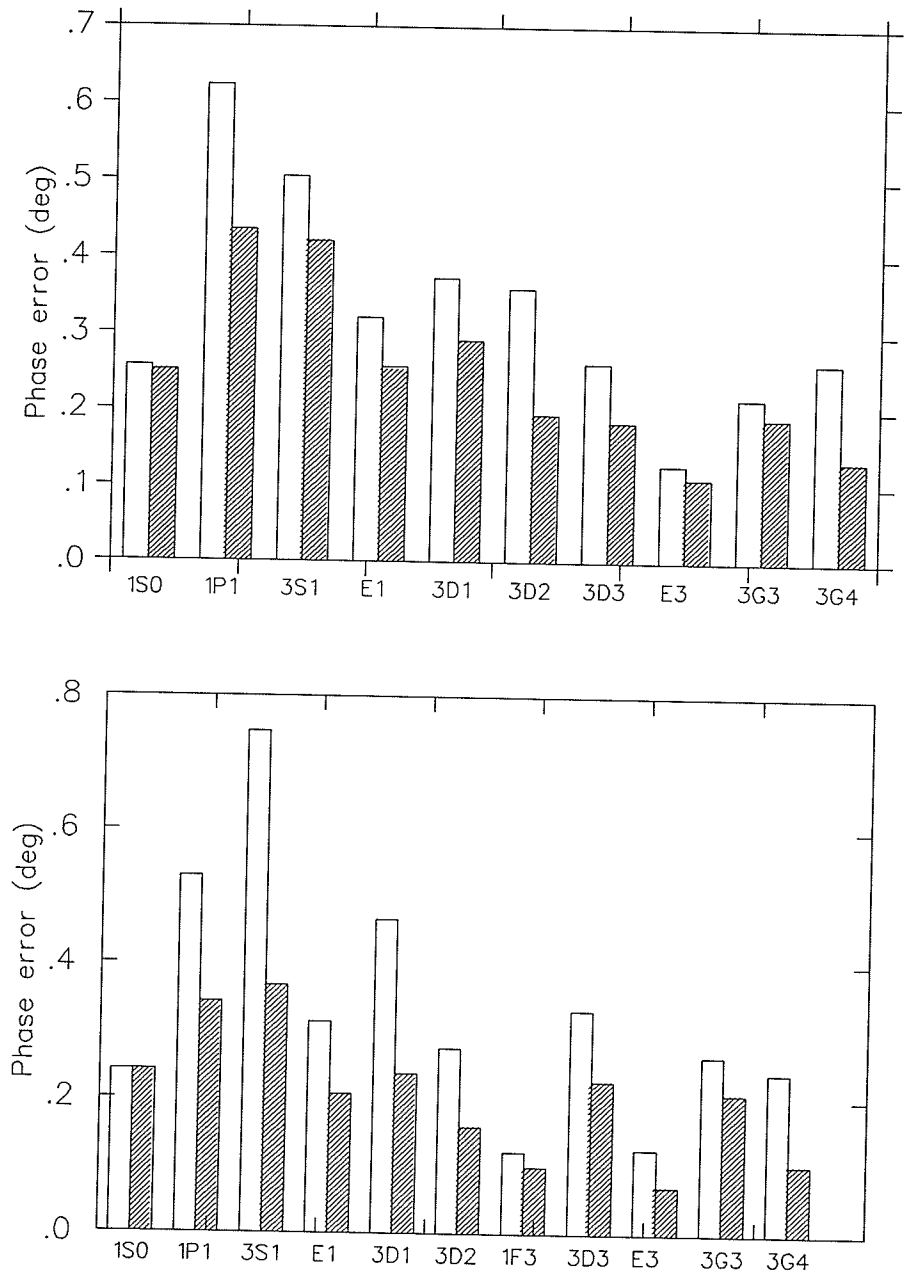


Figure 5.15: Phase errors at (a) 220 MeV and (b) 325 MeV. The hatched part is after the inclusion of present data.

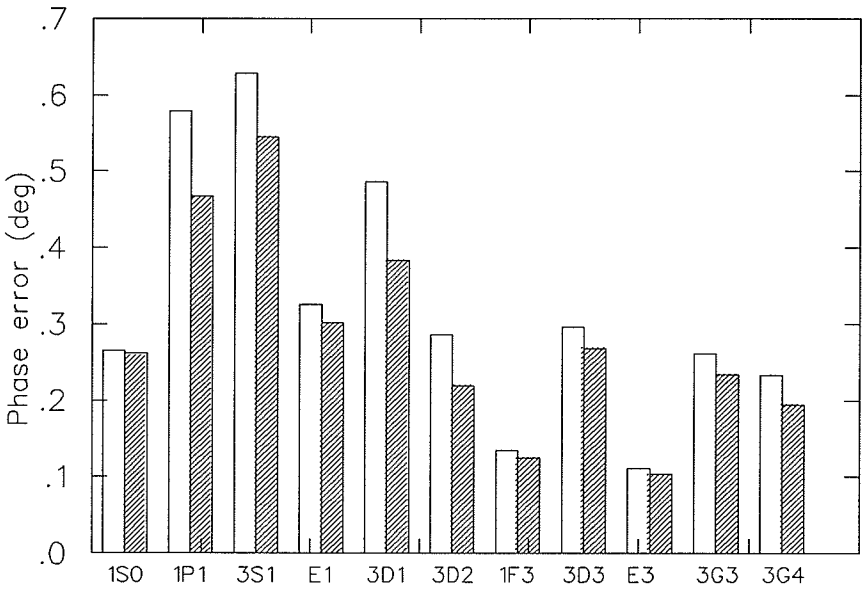


Figure 5.16: Phase errors at 425 MeV. The hatched part is after the inclusion of present data.

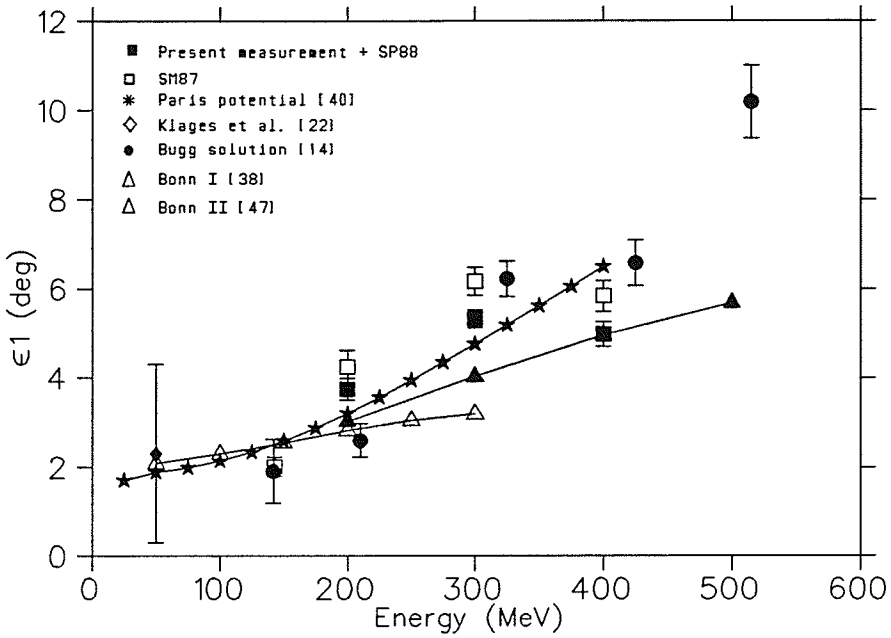


Figure 5.17: $\epsilon_1$ Phases, predicted values and the experimental data

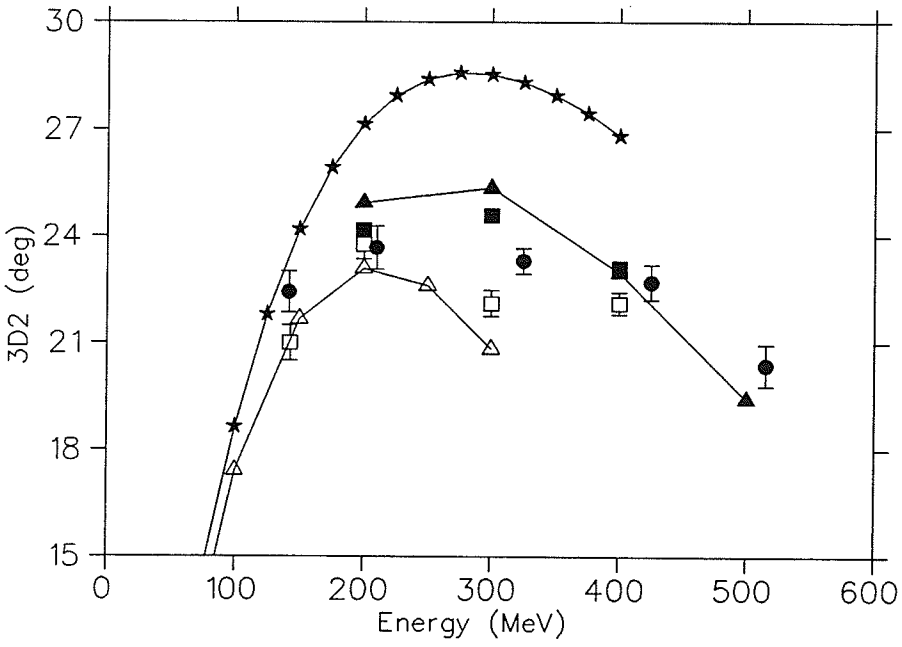


Figure 5.18: 3D2 Phases, predicted values and the experimental data. Symbols are defined in the previous figure.

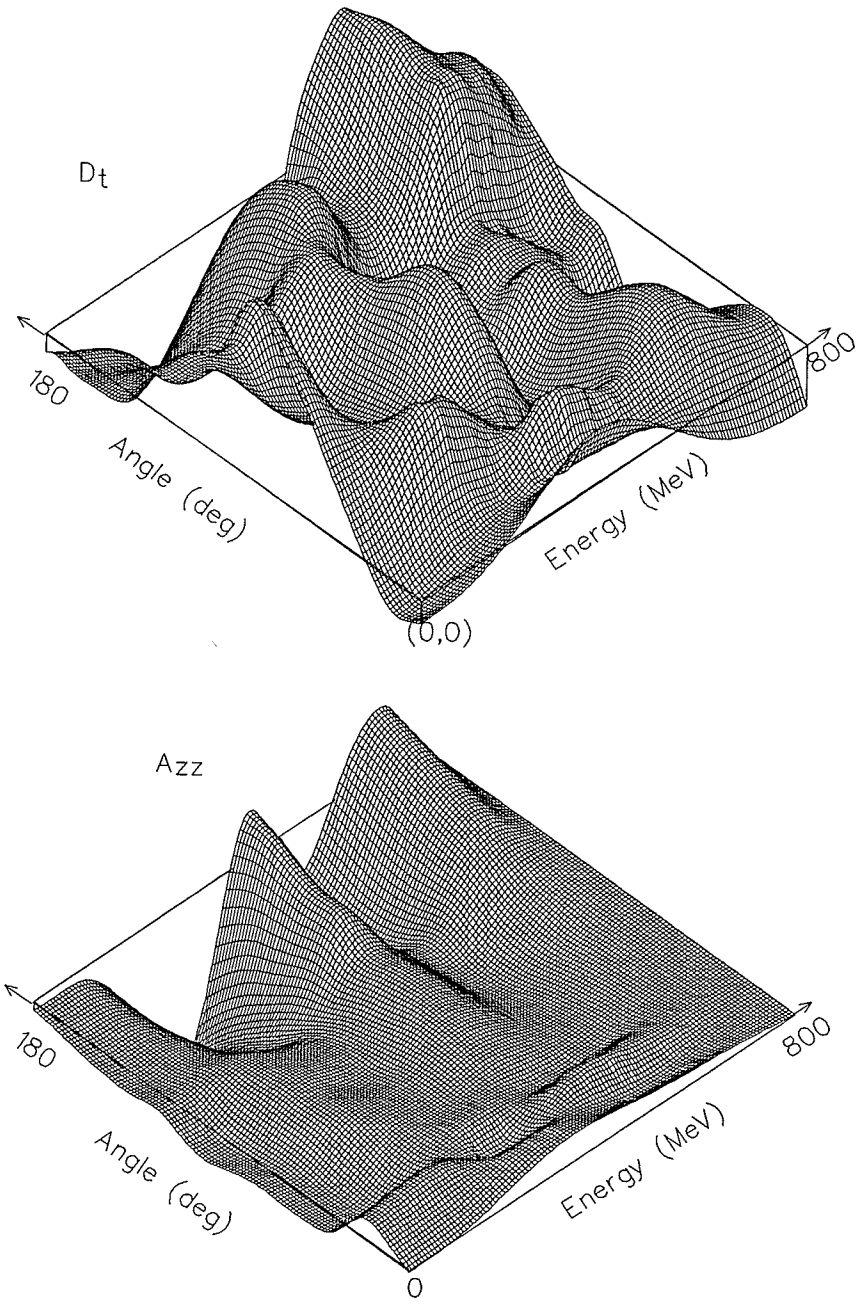


Figure 5.19: Angle-energy correlation of the difference in predictions of the Saclay-Geneva and SP88 version of Arndt's phase shift analyses. (a) Dt parameter. $(\delta D_t)_{max} = 0.265$, $(\delta D_t)_{min} = -0.228$ (b) Azz parameter. $(\delta A_{zz})_{max} = 0.4872$, $(\delta A_{zz})_{min} = -.160$

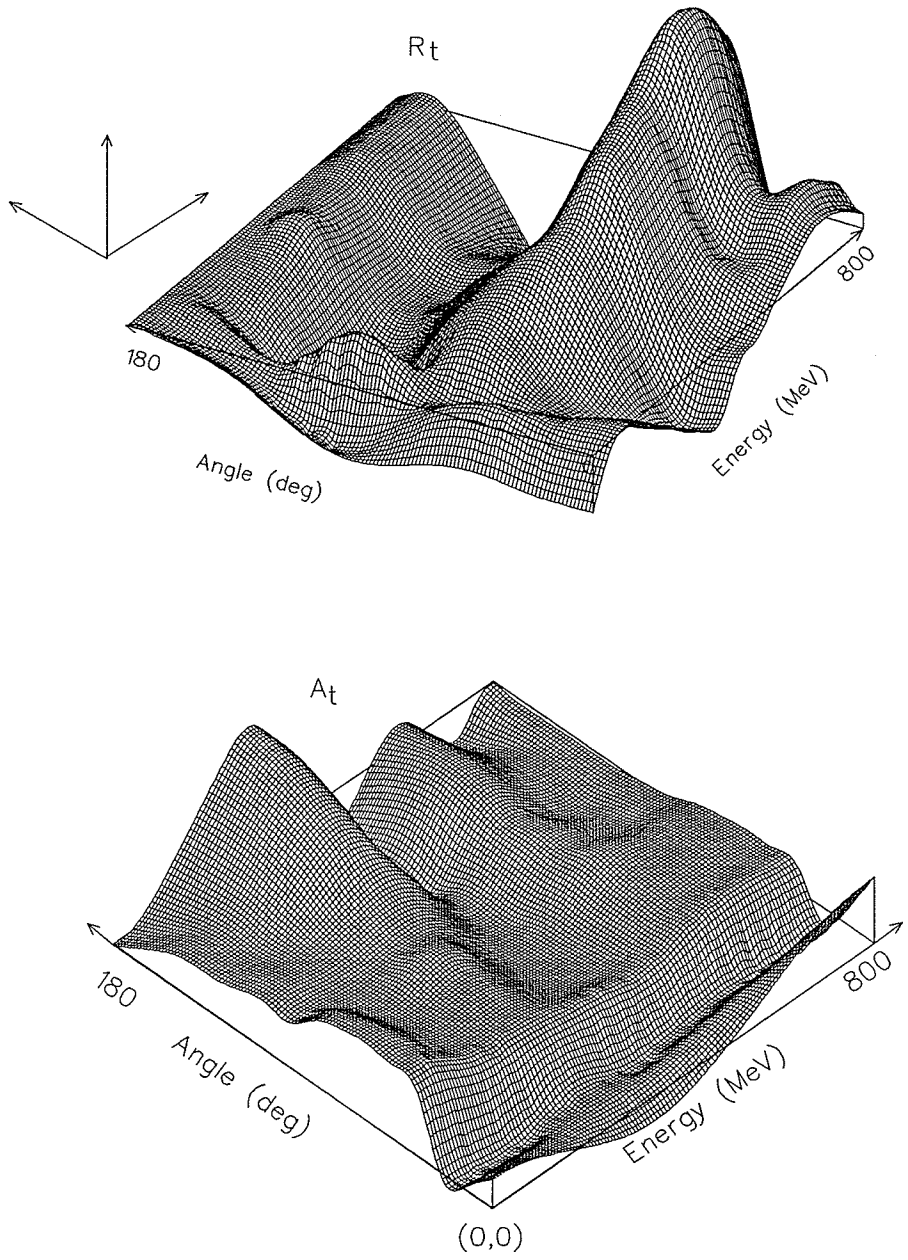


Figure 5.20: Difference in the predicted values of (a) $R_t$ and (b) $A_t$ parameter. The difference is between the Saclay-Geneva and Arndt's phase shift analyses. $(\delta R_t)_{max} = 0.344$, $(\delta R_t)_{min} = -0.319$, $(\delta A_t)_{max} = 0.236$, $(\delta A_t)_{min} = -0.611$

# Bibliography


[1] D. V. Bugg. *Ann. Rev. Nucl. Part. Sci.*, 35:295, 1985.

[2] M. Beyer and H. J. Weber. A nucleon-nucleon potential with quark degrees of freedom. TRIUMF preprint no. 86-1674, 1986.

[3] J.Bystricky et al. *J.Physique*, 48:199, 1987.

[4] R.Arndt et al. *Phys. Rev.*, D 28:199, 1983.

[5] C. Lechanoine-Leluc et al. *J.Physique*, 48:985, 1987.

[6] C.R.Newsom. *Free Neutron Proton Analyzing Power at Medium Energies.* PhD thesis, The University of Texas at Austin, 1980.

[7] A.S.Clough et al. *Phys. Rev.*, C 21:988, 1980.

[8] I.R.Afnan and J.M.Read. *Phys. Rev.*, C 12:293, 1975.

[9] H.Kummel et al. *Phys Reports*, 36:1, 1978.

[10] G.E.Brown and A.D.Jackson. *The Nucleon-Nucleon Interaction.* North-Holland Publishing Company, 1976.

[11] J. Bynstock and R. Bryan. *Phys. Rev.*, D 9:2528, 1974.

[12] G. S. Chulick et al. *Phys. Rev.*, C 37:1549, 1988.

[13] R.A.Arndt. SAID :an interactive dial-in program for scattering analysis. 1988.

[14] D.V.Bugg et al. *Phys Rev*, C 21:1004, 1980.

[15] W.T.H. van Oers. *Nucl. Phys*, A 463:517c, 1987.

[16] M. Schober et. al. *J. Phys G: Nucl. Phys.*, 10:L247, 1984.

[17] J.J.Malanify et al. *Phys. Rev. Lett.*, 17:481, 1966.

[18] G.Fink et al. Status of the neutron-proton scattering experiments and phase-shift analyses up to 50 MeV neutron energy. In *International Nuclear Physics Conference, Harrogate, U.K*, 1986.

[19] S.W.Johnsen et al. *Phys. Rev. Lett.*, 38:1123, 1977.

[20] D.H.Fitzgerald et al. *Phys. Rev.*, C 21:1190, 1980.

[21] P. Doll et al. n-p scattering experiments and n-$^3He$ experiments from 1 to 50 MeV. In *Proc. Intl. Workshop on few-body approaches to nuclear reactions in tandem and cyclotron energy regions.*, Tokyo, August 22-24,, 1986.

[22] H. O. Klages, 1988. Private communication.

[23] J.Sowinsky et al. *Physics Letters*, B199:317, 1987.

[24] T.S.Bhatia et al. The measurement of $A_{nn}$ for free n-p scattering. In *Proc 5th Int. symp. on Polarzation Phen*, 1981.

[25] P.La France and P.Winternitz. *J.Physique*, 41:1391, 1980.

[26] J.Bystricky et al. *J.Physique*, 39:1, 1978.

[27] C.R.Schumacher and H.A.Bethe. *Phys. Rev.*, 121:1534, 1961.

[28] L. Puzikov et al. *Soviet Physics - JETP*, 5(32):489, 1957.

[29] M.Jacob and G.C.Wick. *Ann. Phys. (N.Y.)*, 7:404, 1959.

[30] H. Spinka. *Phys. Rev.*, D 30:1461, 1984.

[31] *AIP conf. Proc. on Higher Energy Polarized Proton Beams*, Ann Arbor; 42,142, 1977.

[32] N. Hoshizaki. *Prog. Theor. Phys. (suppl.)*, 42:107, 1968.

[33] L. Wolfenstein. *Ann. Rev. Nucl. Sci.*, 6:43, 1956.

[34] M.H.MacGregor et al. *Ann. Rev. Nucl. Sci.*, 10:292, 1960.

[35] H.P.Stapp et al. *Phys. Rev.*, 105:721, 1957.

[36] R.A.Arndt and L.D.Roper. *Nucl. Phys.*, B50:285, 1972.

[37] M.H.McGregor et al. *Phys. Rev.*, 182:1714, 1969.

[38] R. Machleidt et al. *Phys. Rep.*, 149:1, May, 1987.

[39] R. Vinh Mau. Mesons in nuclei, v1, 1979.

[40] M.Lacombe et al. *Phys. Rev.*, D 12:1495, 1975.

[41] M.Lacombe et al. *Phys. Rev.*, C 21:861, 1980.

[42] J.J.de Swart et al. *Nucl. Phys.*, A416:299c, 1984.

[43] R.Machleidt. Nuclear forces within a consistent meson exchange model. In *Symposium on Quarks and Nuclear Structure*, Bad Honnef, W.Germany, 1983.

[44] W.Grein and P.Kroll. *Nucl. Phys.*, A 338:332, 1980.

[45] Ch. Elster et al. *Phys. Rev.*, C 37:1647, 1988.

[46] Ch. Elster, 1988. Private communication.

[47] R. Machleidt. *Adv. Nucl. Phys*, 19 (in press):1, 1988.

[48] R. Abegg et.al. *Nucl. Instr. & Meth.*, **A 234**:11, 1985.

[49] R. Abegg et.al. *Nucl. Instr. & Meth.*, **A 234**:20, 1985.

[50] C. Amsler et al. *Nucl. Instr. & Meth.*, **144**:401, 1977.

[51] R. Abegg and R. Schubank. TRIUMF Report , TRI-DN-87-17, unpublished, 1987.

[52] L.G.Greeniaus and J. Soukup. Polarimeter - Beam Energy Monitor. TRIUMF Internal Report , TRI-DN-81-1, 1981.

[53] R. Abegg et.al. *Phys. Rev. Lett.*, **56**:2571–2574, 1986.

[54] D. V. Bugg & C. Wilkin. *Nucl. Phys.*, **A467**:575, 1987,. Also D. V. Bugg private communication.

[55] D. V. Bugg, 1988. private communication.

[56] D. Hutcheon, 1988. TRIUMF expt. no. 466, The $np - \pi d$ cross section near threshold,.

[57] P.P.J.Delheij et al. *Nucl. Instr. & Meth.*, **A 264**:186, 1988.

[58] K. Chantziantoniou. Calibration of frozen spin polarized proton target. Master's thesis, University of Manitoba, 1988.

[59] A. Abragam and M Goldman. *Rep. Prog. Phys.*, **Vol. 41**:395, 1978.

[60] R. Abegg et.al. *Nucl. Instr. and Meth.*, **A 254**:469, 1987.

[61] E. Gatti et.al. *Nucl. Instr. and Meth.*, 163:83, 1979.

[62] W. T. Welford and R. Winston. *The Optics of Non Imaging Contractors - Light and Solar Energy.* Academic Press, New York, 1978.

[63] C. A. Davis:, 1987:. University of Manitoba internal note.

[64] D. Frekers, 1987. Private communication.

[65] L. G. Greeniaus, 1987. Private communication.

[66] P. Poffenberger. A pedestrian's giude to the CSB delay line chambers. TRIUMF Internal Report , TRI-DN-84-30, 1984.

[67] R. A. Abegg et al. Ratio of Spin Transfer Parameters $d_t/r_t$ in $d(\vec{p},\vec{n})pp$ Quasi-elastic Scattering, 1988. Submitted for publication in Phys. Rev. C.

# Appendix A

# Calibration of Target Polarization

The measurement of $A_{yy}$ to an absolute accuracy of $\pm 0.03$ required the target polarization to be known to an accuracy of $\pm 0.02$. The usual NMR technique employed to measure the target polarization is good to within 4% [60]. Thus an independent measurement of the target polarization using nuclear elastic scattering was essential. Each of two data taking runs was preceded and followed by target calibration runs. The experimental set up is shown in fig A.1. The details of the techniques involved in measuring and analyzing the data can be found in the M.Sc. thesis of K. Chantziantoniou [58]. Only a short summary will be presented here.

An unpolarized beam of 499 or 512 MeV protons was scattered from a liquid hydrogen ($LH_2$) or an extended graphite target which replaced the liquid deuterium target used for neutron production. The 'JANIS' solenoid and the 4AB2 bending magnet were turned off (fig A.1). The primary beam after the $LH_2$ target was stopped in a beam stop in the $0^0$ collimator port. The secondary proton beam produced in the $LH_2$ or graphite target was transported through the $9^0$ collimator and through a solenoid, 'SUPERMAN' (SUPER conducting magnet from MANitoba), placed at the exit of the collimator.

The beam stop was 1 m of graphite followed by steel shielding. The solenoid rotated the unwanted normal polarization arising from the scattering off the $LH_2$ or the graphite target into the horizontal plane. Two dipole magnets, 'CLYDE' and 'BONNIE' were energized up to a few Gauss magnetic field in order to correct for the deflection caused by slight misalignment of the 'SUPERMAN' and by the cyclotron fringe field.

In order to define the hit position of protons on the target two drift chambers upstream of the FST were used. The time of flight of the incident protons (secondary beam) was measured between a thin scintillator counter at the exit of the $9^0$ port and another scintillator placed 30 cm upstream of the FST. The scattered protons from the FST were detected in the two proton booms placed around $24^0$ on both sides of the incident beam direction. The boom angles were corrected for the deflection in the target holding field. The boom elements were the same as used for the $A_{yy}$ part of the experiment (chapter 2). The recoil protons were detected in coincidence in two symmetrically placed combination detector arms each consisting of a neutron array veto panel (center) and a 60 cm x 60 cm delay line wire chamber mounted in front of the array. The neutron array-DLC combinations were placed around $61^0$ (after correcting for the deflection) in the lab on both sides of the incident beam direction. The DLCs on the neutron arrays were mounted on rails so that the chambers could slide into place in front of the neutron array during FST calibration and slide out during $A_{yy}$ measurements. A veto scintillator with a hole was installed on each recoil arm 50 cm away from the target. This was used to define good events originating from the FST.

The analysis of the calibration events is carried out the same way as the analysis for the $A_{yy}$ part of the experiment. The track reconstructions for the scattered protons are done by the delay line wire chambers on the boom, the

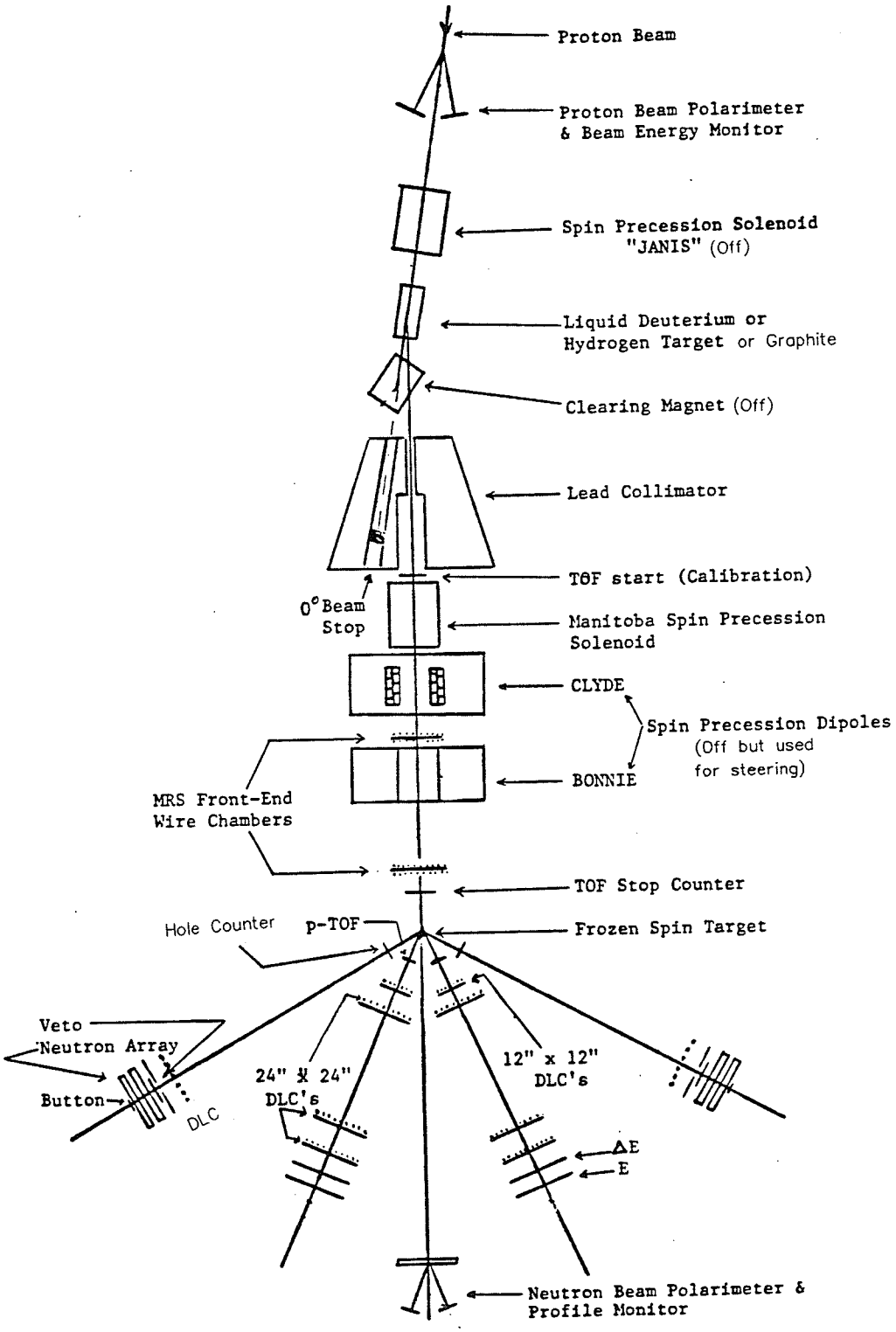


Figure A.1: FST calibration set up

energies being determined from the time-of-flight between the start counter and the E-counter. Since the position resolution in the wire chamber is better than that in the neutron array, the positions of the recoil protons are determined from the wire chamber hanging in front of the neutron array. The time-of-flight between the target center and the veto panel is determined with respect to the start time of the scattered particles. The p-p elastic scattering events are selected on the basis of cuts on the summed chisquare (eqn 4.21 in chapter 4). The background contamination is determined by using a method similar to the one used in the n-p analysis. The final events are corrected for background contamination and the variation of detector efficiencies.

## A.1 Scattering Asymmetry

The asymmetry is calculated from the observed count rates using the 'ratio' method.

$$\epsilon_r = \frac{(r-1)}{(r+1)} \tag{A.1}$$

where

$$r = \left(\frac{L_+ R_-}{L_- R_+}\right)^{1/2}$$

The statistical uncertainty in $\epsilon_r$ is

$$\delta\epsilon_r = \frac{r}{(r+1)^2}\left[\frac{1}{R_+} + \frac{1}{R_-} + \frac{1}{L_+} + \frac{1}{L_-}\right]^{1/2}$$

From the observed asymmetry the target polarization is calculated as

$$P_T = \epsilon_r / A_y \tag{A.2}$$

where $A_y$ is the analyzing power averaged over the target spin up and down runs. Similarly $P_T$ is also the spin averaged target polarization.

The p-p analyzing power $A_y$ is very precisely known from the phase shift analysis, the typical error is 1.0-1.5%. In the present experiment the nominal proton boom angle was $24^0$ and the average incident energies were 469 MeV and 499 MeV at the FST center for $LH_2$ and graphite target respectively. Furthermore, the detector spans about $\pm 5^0$ around the nominal angle. Thus over the entire detector acceptance, the average analyzing power is calculated from the expression,

$$A_y = \frac{\int A_y(\theta) w(\theta) d\theta}{\int w(\theta) d\theta}$$

where the weighting function $w(\theta)$ is determined from the data taken with target unpolarized. $A_y(\theta)$ is taken from the 1988 phase shift analysis of R. Arndt [13].

From the vertex reconstruction, the FST cell was divided into three bins, top, middle and bottom. The analyzing power and hence the target polarization are determined for each of these three bins. The average FST polarization is then calculated by taking the weighted average of these three bins. Assuming an exponential decay, the average NMR value of target polarization is determined from ,

$$\bar{P}_{NMR} = \frac{P_B - P_E}{ln(P_B/P_E)} \tag{A.3}$$

where $P_B$ and $P_E$ are the measured FST polarization at the beginning and end of calibration runs. Thus the NMR correction factor is defined as,

$$P_T(scatt.) = \mu \bar{P}_{NMR}$$

The factor $\mu$ is determined for 3 different cuts on the individual $\chi^2$, viz. $\chi_i^2 \leq$ 9,5,3. Since the factor $\mu$ does not vary significantly between $\chi_i^2 \leq 9$ and $\chi_i^2 \leq$ 3 the final value of $\mu$ is taken to be equal to $0.961 \pm 0.008(stat) \pm 0.015(sys)$ corresponding to $\chi_i^2 \leq 9$.

# Appendix B

# Different Methods of Extracting $A_{yy}$

There are several different ways one can combine left and right yields for runs with both beam and target simultaneously polarized to extract the spin correlation parameter, $A_{yy}$. Some of the methods are summarized in the following section. The comparison among different methods in light of cancellation of systematic errors will be discussed in Appendix C.

The observed countrates with polarized beam (first index) and polarized target(2nd index) are given by :

$$L_{\pm\pm} = \sigma_{1\pm}(1 \pm A(P_B + P_T) + P_B P_T A_{yy}) \quad \text{(B.1)}$$

$$R_{\pm\pm} = \sigma_{2\pm}(1 \mp A(P_B + P_T) + P_B P_T A_{yy}) \quad \text{(B.2)}$$

$$L_{\pm\mp} = \sigma_{3\pm}(1 \pm A(P_B - P_T) - P_B P_T A_{yy}) \quad \text{(B.3)}$$

$$R_{\pm\mp} = \sigma_{4\pm}(1 \mp A(P_B - P_T) - P_B P_T A_{yy}) \quad \text{(B.4)}$$

For the time being it is assumed that $\sigma_{1\pm} = \sigma_{2\pm} = \sigma_{3\pm} = \sigma_{4\pm} = \sigma_0$. Since there are two sets of detectors set at equal but opposite angles and since we have four different spin combinations the systematic errors arising from different detector efficiencies and beam normalizations cancel in first order.

Thus the above assumption does not make much difference in first order. $P_B$ and $P_T$ are the spin averaged beam and target polarizations.

**Method 1 :** Target spin is up, beam spin both up and down, both sets of detectors.

$$L_{++} = \sigma_0(1 + A(P_B + P_T) + P_B P_T A_{yy}) \quad \text{(B.5)}$$

$$R_{++} = \sigma_0(1 - A(P_B + P_T) + P_B P_T A_{yy}) \quad \text{(B.6)}$$

$$L_{-+} = \sigma_0(1 - A(P_B - P_T) - P_B P_T A_{yy}) \quad \text{(B.7)}$$

$$R_{-+} = \sigma_0(1 + A(P_B - P_T) - P_B P_T A_{yy}) \quad \text{(B.8)}$$

$$A_{yy,1} = \frac{1}{P_B P_T} \frac{L_{++} + R_{++} - L_{-+} - R_{-+}}{L_{++} + R_{++} + L_{-+} + R_{-+}} \quad \text{(B.9)}$$

$$= \frac{\epsilon}{P_B P_T} \quad \text{(B.10)}$$

**Method 2 :** Target spin is down, beam spin both up and down, left and right sets of detectors.

$$L_{--} = \sigma_0(1 - A(P_B + P_T) + P_B P_T A_{yy}) \quad \text{(B.11)}$$

$$R_{--} = \sigma_0(1 + A(P_B + P_T) + P_B P_T A_{yy}) \quad \text{(B.12)}$$

$$L_{+-} = \sigma_0(1 + A(P_B - P_T) - P_B P_T A_{yy}) \quad \text{(B.13)}$$

$$R_{+-} = \sigma_0(1 - A(P_B - P_T) - P_B P_T A_{yy}) \quad \text{(B.14)}$$

$$A_{yy,2} = \frac{1}{P_B P_T} \frac{L_{--} + R_{--} - L_{+-} - R_{+-}}{L_{--} + R_{--} + L_{+-} + R_{+-}} \quad \text{(B.15)}$$

$$= \frac{\epsilon}{P_B P_T} \quad \text{(B.16)}$$

The average of methods 1 and 2 is written as :

$$A_{yy,12} = \frac{(A_{yy,1} + A_{yy,2})}{2} \quad \text{(B.17)}$$

**Method 3 :** Left arm of the detectors , target and beam spins both up and down.

$$A_{yy,3} = \frac{1}{P_B P_T} \frac{L_{++} + L_{--} - L_{+-} - L_{-+}}{L_{++} + L_{--} + L_{+-} + L_{-+}} \quad \text{(B.18)}$$

$$= \frac{\epsilon}{P_B P_T} \quad \text{(B.19)}$$

**Method 4 :** Right arm of the detectors , target and beam spins both up and down.

$$A_{yy,4} = \frac{1}{P_B P_T} \frac{R_{++} + R_{--} - R_{+-} - R_{-+}}{R_{++} + R_{--} + R_{+-} + R_{-+}} \quad \text{(B.20)}$$

$$= \frac{\epsilon}{P_B P_T} \quad \text{(B.21)}$$

The average of methods 3 and 4 is written as :

$$A_{yy,34} = \frac{(A_{yy,3} + A_{yy,4})}{2} \quad \text{(B.22)}$$

**Method 5 :** Both arms of detectors, all four combinations of beam and target spins.

Define

$$X^2 = \frac{(L_{++} + R_{++})(L_{--} + R_{--})}{(L_{+-} + R_{+-})(L_{-+} + R_{-+})} \quad \text{(B.23)}$$

$$A_{yy,5} = \frac{1}{P_B P_T} \frac{(X-1)}{(X+1)} \quad \text{(B.24)}$$

**Method 6 :** Same as method 5 with different combinations of left and right counts.

Define

$$S^2 = \frac{(L_{++} + L_{--})(R_{++} + R_{--})}{(L_{+-} + L_{-+})(R_{+-} + R_{-+})} \quad \text{(B.25)}$$

$$A_{yy,6} = \frac{1}{P_B P_T} \frac{(S-1)}{(S+1)} \quad \text{(B.26)}$$

It can be shown that $A_{yy,34}$ and $A_{yy,6}$ are equivalent and so are $A_{yy,5}$ and $A_{yy,12}$. $A_{yy}$ obtained from these methods agree with each other as is evident

Table B.1: Comparison of different methods of determining $A_{yy}$

| Neutron array angle (lab) | Central bin angle (c.m.) | $A_{yy,12}$ | Stat. error | $A_{yy,34}$ | Stat. error | $A_{yy,5}$ | Stat. error | $A_{yy,6}$ | Stat. error |
|---|---|---|---|---|---|---|---|---|---|
| Neutron energy = 220 MeV | | | | | | | | | |
| 47 | 104.95 | 0.449 | 0.014 | 0.446 | 0.013 | 0.448 | 0.012 | 0.446 | 0.013 |
| | 100.90 | 0.445 | 0.014 | 0.443 | 0.013 | 0.445 | 0.013 | 0.443 | 0.013 |
| | 96.86 | 0.392 | 0.015 | 0.392 | 0.013 | 0.392 | 0.013 | 0.392 | 0.013 |
| | 92.83 | 0.418 | 0.016 | 0.417 | 0.014 | 0.418 | 0.014 | 0.417 | 0.014 |
| | 88.82 | 0.395 | 0.017 | 0.395 | 0.016 | 0.395 | 0.016 | 0.395 | 0.016 |
| Neutron energy = 325 MeV | | | | | | | | | |
| 67 | 145.92 | 0.237 | 0.020 | 0.233 | 0.020 | 0.237 | 0.020 | 0.233 | 0.020 |
| | 141.65 | 0.314 | 0.017 | 0.312 | 0.016 | 0.314 | 0.016 | 0.312 | 0.016 |
| | 137.39 | 0.319 | 0.015 | 0.318 | 0.014 | 0.319 | 0.014 | 0.318 | 0.014 |
| | 133.15 | 0.378 | 0.016 | 0.377 | 0.014 | 0.378 | 0.014 | 0.377 | 0.014 |
| | 128.93 | 0.370 | 0.016 | 0.370 | 0.015 | 0.370 | 0.015 | 0.370 | 0.015 |
| Neutron energy = 425 MeV | | | | | | | | | |
| 27 | 65.57 | 0.094 | 0.022 | 0.094 | 0.022 | 0.093 | 0.022 | 0.094 | 0.022 |
| | 61.73 | 0.115 | 0.022 | 0.116 | 0.022 | 0.115 | 0.022 | 0.116 | 0.022 |
| | 57.91 | 0.079 | 0.023 | 0.079 | 0.023 | 0.079 | 0.023 | 0.079 | 0.023 |
| | 54.12 | 0.114 | 0.025 | 0.117 | 0.024 | 0.115 | 0.025 | 0.118 | 0.024 |
| | 50.35 | 0.100 | 0.032 | 0.101 | 0.032 | 0.100 | 0.032 | 0.101 | 0.032 |

from the table -B.1 which summarizes the data at three representative angles viz., $\theta_n = 67^0, 47^0$ ,and $27^0$ with incident neutron energy = 325, 220, and 425 MeV respectively.

If one knows the analyzing power very accurately one can extract the spin correlation parameter in a slightly different way.

**Method 7:** Defining

$$r^2 = \frac{L_{++}R_{--}}{L_{--}R_{++}}, \qquad S = \frac{(r+1)}{(r-1)}$$

one gets :

$$A_{yy,7} = \frac{1}{P_B P_T}(A(P_B + P_T)S - 1) \tag{B.27}$$

# Appendix C

# Systematic Errors

Since the detectors were placed symmetrically around the incident beam direction and also because of the way the left and right yields are combined to extract $A_{yy}$ and $A_y$ most of the systematic errors vanish to first order. The effects of various systematic errors on the spin correlation parameter,$A_{yy}$, are discussed below. Throughout the present error calculation the following numerical values are used : the beam polarization,$P_b = 0.60$ ,the target polarization,$P_t = 0.80$, the analyzing power, $A_y = 0.5$, the spin correlation parameter, $A_{yy} = 0.5$. In Appendix B various methods of determining the spin correlation parameter have been discussed. In this chapter a comparison among three different methods (#5,6 and 7 of the previous chapter, redefined here as methods 2,1 and 3 respectively) on the basis of systematic errors will be made.

## C.1 Spin Correlation parameter

The spin correlation parameter $A_{yy}$ as determined in method 1 (method 6 in the previous chapter) is :

$$A_{yy} = \frac{1}{P_b P_t} \frac{(S-1)}{(S+1)} \tag{C.1}$$

with

$$\begin{aligned} S^2 &= \frac{(L_{++}+L_{--})(R_{++}+R_{--})}{(L_{+-}+L_{-+})(R_{+-}+R_{-+})} \\ &= \frac{(1+P_t P_b A_{yy})^2}{(1-P_t P_b A_{yy})^2} \end{aligned}$$

Thus the error in $S$ is related to the error in $A_{yy}$ by:

$$\frac{\delta A_{yy}}{A_{yy}} = \frac{2\delta S}{(S^2-1)} \tag{C.2}$$

Thus $\delta A_{yy} = 0.60\ \delta S$ or the error in $A_{yy}$ is only 60% of the error in S.

**Method 2 (previously method 5) :**

$$A_{yy} = \frac{1}{P_b P_t} \frac{(X-1)}{(X+1)}$$

where

$$X^2 = \frac{(L_{++}+R_{++})(L_{--}+R_{--})}{(L_{+-}+R_{+-})(L_{-+}+R_{-+})}$$

The error in $A_{yy}$ is $\delta A_{yy} = 0.60 \delta X$.

**Method 3 (method 7 in the previous chapter) :**

$$A_{yy} = \frac{1}{P_b P_t}(A_y(P_b+P_t)R-1)$$

where

$$R = \frac{r+1}{r-1} \quad ,$$

with

$$\begin{aligned} r^2 &= \frac{L_{++}R_{--}}{L_{--}R_{++}} \\ &= \frac{(1+A_y(P_b+P_t)+P_bP_tA_{yy})^2}{(1-A_y(P_b+P_t)+P_bP_tA_{yy})^2} \end{aligned}$$

Thus

$$\delta A_{yy} = \frac{A_y(P_b+P_t)}{P_bP_t}\,\delta R = 1.4583\,\delta R$$

where

$$|\delta R| = \frac{2}{(r-1)^2}\,\delta r = 0.30\,\delta r$$

### C.1.1 Different beam polarizations:

There is always a difference in average beam and target polarizations between target spin up and down runs (see table 4.8). Suppose for example, the beam polarization for target spin up is $P_{b+} = P_b(1+\delta)$ and the corresponding quantity for target spin down is $P_{b-} = P_b(1-\delta)$ where $P_b$ is the beam polarization averaged over the two target spin states. The count rates become :

$$\begin{aligned} L_{\pm\pm} &= \sigma_0(1 \pm A_y(P_b(1\pm\delta)+P_t)+P_b(1\pm\delta)P_tA_{yy}) \\ R_{\pm\pm} &= \sigma_0(1 \mp A_y(P_b(1\pm\delta)+P_t)+P_b(1\pm\delta)P_tA_{yy}) \\ L_{\pm\mp} &= \sigma_0(1 \pm A_y(P_b(1\mp\delta)-P_t)-P_b(1\mp\delta)P_tA_{yy}) \\ R_{\pm\mp} &= \sigma_0(1 \mp A_y(P_b(1\mp\delta)-P_t)-P_b(1\mp\delta)P_tA_{yy}) \end{aligned}$$

Substituting the actual left-right yields in the above equation one gets :

$$S^2 = \frac{(1+P_tP_bA_{yy})^2-(\delta A_yP_b)^2}{(1-P_tP_bA_{yy})^2-(\delta A_yP_b)^2} \qquad \text{(C.3)}$$

with $\delta_{max} = 0.028$ (table 4.8) one gets $(\delta A_yP_b)^2 = 0.0002$ which is negligibly small compared to the first terms in both the numerator and denominator.

### C.1.2 Different target polarizations:

One writes for target spin up, $P_t^+ = P_t(1+\delta)$ and for target spin down $P_t^- = P_t(1-\delta)$. Substitution in the equation (5) gives :

$$S^2 = \frac{(1+P_tP_bA_{yy})^2 - (\delta A_yP_t)^2}{(1-P_tP_bA_{yy})^2 - (\delta A_yP_t)^2} \tag{C.4}$$

With $\delta_{max} = 0.05$ one gets $(\delta A_yP_t)^2 = 0.000361$ which is again negligible.

For the other two methods one can show that the systematic errors arising from different beam and target polarization are also negligible.

### C.1.3 Misalignment of the apparatus

Suppose that because of a purely geometrical error or because of wrong correction for deflection in holding field, there is a mismatch of left and right angles. For two states of the target spin, let the actual angle for the left boom be $\theta_\pm = \theta_0 \pm \delta$. For the right boom it is the same but with the sign of $\delta$ reversed. Because of this angle mismatch, $A_y$ and $A_{yy}$ for left and right detectors will be different. One then writes the count rates as :

$$L_{\pm\pm} = \sigma_0(1 \pm A_y(\theta \pm d\theta)(P_b + P_t) + P_bP_tA_{yy}(\theta \pm d\theta)) \tag{C.5}$$

$$R_{\pm\pm} = \sigma_0(1 \mp A_y(\theta \mp d\theta)(P_b + P_t) + P_bP_tA_{yy}(\theta \mp d\theta)) \tag{C.6}$$

$$L_{\pm\mp} = \sigma_0(1 \pm A_y(\theta \mp d\theta)(P_b - P_t) - P_bP_tA_{yy}(\theta \mp d\theta)) \tag{C.7}$$

$$R_{\pm\mp} = \sigma_0(1 \mp A_y(\theta \pm d\theta)(P_b - P_t) - P_bP_tA_{yy}(\theta \pm d\theta)) \tag{C.8}$$

**Method 1 :** $S^2$ becomes :

$$S^2 = \left(\frac{1+\epsilon_1}{1-\epsilon_2}\right)^2 S_0^2$$

and **Method 2**

$$X^2 = \left(\frac{1+\epsilon_1}{1-\epsilon_2}\right)^2 X_0^2$$

where

$$\begin{aligned} S_0^2, X_0^2 &= \frac{(1+P_tP_bA_{yy})^2}{(1-P_tP_bA_{yy})^2} \\ \epsilon_1 &= \frac{(P_b+P_t)d\theta(\frac{dA_y}{d\theta})}{1+P_bP_tA_{yy}} \\ \epsilon_2 &= \frac{(P_b-P_t)d\theta(\frac{dA_y}{d\theta})}{1-P_bP_tA_{yy}} \end{aligned}$$

With $d\theta = 0.1^0$ (anticipated error in proton boom positioning), and $\frac{dA_y}{d\theta} = 0.03/deg$, then: $\frac{\delta A_{yy}}{A_{yy}} = 0.5\%$ for both methods 1 and 2.

**Method 3**

$$r = r_0 \frac{(1+x_1)}{(1+x_2)} \tag{C.9}$$

with

$$\begin{aligned} x_1 &= \frac{d\theta(\frac{dA_y}{d\theta})(P_b+P_t) + d\theta(\frac{dA_{yy})}{d\theta}P_bP_t}{1+A_y(P_b+P_t)+A_{yy}P_bP_t} \\ x_2 &= \frac{d\theta\frac{dA_y}{d\theta}(P_b+P_t) - d\theta\frac{dA_{yy}}{d\theta}P_bP_t}{1-A_y(P_b+P_t)+A_{yy}P_bP_t} \end{aligned}$$

Substituting various values one gets : $\frac{\delta A_{yy}}{A_{yy}} = 0.3\%$.

Now if the error in the boom angles is not correlated with the target spin then we can write $\theta_L = \theta_0 + \delta$ and $\theta_R = \theta_0 - \delta$. Thus,

$$L_{\pm\pm} = \sigma_0(1 \pm A_y(\theta+d\theta)(P_b+P_t) + P_bP_tA_{yy}(\theta+d\theta)) \tag{C.10}$$

$$R_{\pm\pm} = \sigma_0(1 \mp A_y(\theta-d\theta)(P_b+P_t) + P_bP_tA_{yy}(\theta-d\theta)) \tag{C.11}$$

$$L_{\pm\mp} = \sigma_0(1 \pm A_y(\theta+d\theta)(P_b-P_t) - P_bP_tA_{yy}(\theta+d\theta)) \tag{C.12}$$

$$R_{\pm\mp} = \sigma_0(1 \mp A_y(\theta-d\theta)(P_b-P_t) - P_bP_tA_{yy}(\theta-d\theta)) \tag{C.13}$$

In this case one then gets:

**Method 1**

$$S^2 = S_0^2\frac{(1-f_1^2)}{(1-f_2^2)} \tag{C.14}$$

with

$$f_1 = \frac{P_b P_t d\theta(\frac{dA_{yy}}{d\theta})}{1 + P_b P_t A_{yy}}, \quad f_2 = \frac{P_b P_t d\theta(\frac{dA_{yy}}{d\theta})}{1 - P_b P_t A_{yy}}$$

Assuming $d\theta = 0.1^0, (dA_{yy}/d\theta) = 0.03/deg$, the error, $\delta A_{yy} \simeq 0$.

**Method 2**

$$X^2 = X_0^2 \frac{(1-\epsilon_1^2)}{(1-\epsilon_2^2)} \tag{C.15}$$

the $\epsilon$'s are given above. $\delta A_{yy}$ is also vanishingly small in this case.

**Method 3**

$$r^2 = r_0^2 \frac{(1-x_1^2)}{(1-x_2^2)} \tag{C.16}$$

with $x_1$ and $x_2$ defined above. In this case $\delta A_{yy} \simeq 0$.

### C.1.4 Efficiency Change

Suppose that the efficiencies of the left and right detectors change between two target spin runs. Since the beam spin reverses much more frequently than the target spins, the variation of efficiencies with the beam spin is neglected. The count rates are (dropping out the common factors):

$$L_{\pm\pm} = \epsilon_{L\pm}(1 \pm A_y(P_b + P_t) + P_b P_t A_{yy}) \tag{C.17}$$

$$R_{\pm\pm} = \epsilon_{R\pm}(1 \mp A_y(P_b + P_t) + P_b P_t A_{yy}) \tag{C.18}$$

$$L_{\pm\mp} = \epsilon_{L\mp}(1 \pm A_y(P_b - P_t) - P_b P_t A_{yy}) \tag{C.19}$$

$$R_{\pm\mp} = \epsilon_{R\mp}(1 \mp A_y(P_b - P_t) - P_b P_t A_{yy}) \tag{C.20}$$

$S^2$ then becomes :

$$S^2 \simeq S_0^2 \left[1 - \frac{A_y P_b (P_t^2 A_{yy} - 1)}{(1 - P_b^2 P_t^2 A_{yy}^2)} \left(\frac{\epsilon_{R+}}{\epsilon_{R-}} - \frac{\epsilon_{L+}}{\epsilon_{L-}}\right)\right] \tag{C.21}$$

$X^2$ becomes :

$$X^2 \simeq X_0^2 \left[1 - \frac{A_y P_b (P_t^2 A_{yy} - 1)}{(1 - P_b^2 P_t^2 A_{yy}^2)} \left(\frac{\epsilon_{L-}}{\epsilon_{R-}} - \frac{\epsilon_{L+}}{\epsilon_{R+}}\right)\right] \tag{C.22}$$

and $r^2$ becomes :

$$r^2 = r_0^2(\frac{\epsilon_{L-}\epsilon_{R+}}{\epsilon_{L+}\epsilon_{R-}}) \tag{C.23}$$

If the relative change in efficiency for both left and right detectors is the same, then the second term in above equation vanishes and thus $S = S_0$ and $X = X_0$. If the efficiency change is not correlated with the target spin i.e. if $\epsilon_{L+} = \epsilon_{L-}$ and $\epsilon_{R+} = \epsilon_{R-}$ then even if the left and right efficiencies are different, they do not contribute any error to $A_{yy}$ in first order. Let us assume that

$$\epsilon_{R+} = \epsilon_R(1+\delta_1), \quad \epsilon_{R-} = \epsilon_R(1-\delta_1) \tag{C.24}$$

$$\epsilon_{L+} = \epsilon_L(1+\delta_2), \quad \epsilon_{L-} = \epsilon_R(1-\delta_2) \tag{C.25}$$

where

$$\delta_1 = \frac{\epsilon_{R+} - \epsilon_{R-}}{\epsilon_R}, \quad \delta_2 = \frac{\epsilon_{L+} - \epsilon_{L-}}{\epsilon_L}$$

Thus one gets :

$$S^2 = S_0^2\left[1 + 0.2165\left(\frac{1+\delta_1}{1-\delta_1} - \frac{1+\delta_2}{1-\delta_2}\right)\right] \tag{C.26}$$

$$X^2 = X_0^2\left[1 + 0.2165\left(\frac{\epsilon_L}{\epsilon_R}\right)\left(\frac{1-\delta_2}{1-\delta_1} - \frac{1+\delta_2}{1+\delta_1}\right)\right] \tag{C.27}$$

$$r^2 = r_0^2\left[\frac{(1-\delta_2)(1+\delta_1)}{(1+\delta_2)(1-\delta_1)}\right] \tag{C.28}$$

If one assumes that $\delta_1 = 10\%$ and $\delta_2 = 5\%$ and the spin averaged efficiencies for the left and right detectors are the same i.e., $\epsilon_L = \epsilon_R$ then ,

**Method 1:** $\delta A_{yy} = 0.0075$, or $\frac{\delta A_{yy}}{A_{yy}} = 1.5\%$

**Method 2:** $\delta A_{yy} = 0.0065$, or $\frac{\delta A_{yy}}{A_{yy}} = 1.3\%$

**Method 3:** $\delta A_{yy} = 0.0230$, or $\frac{\delta A_{yy}}{A_{yy}} = 4.6\%$

Thus it is clear that the $A_{yy}$ values obtained from method 3 is three times more sensitive to the same relative change of spin dependent efficiencies compared to the other two methods.

### C.1.5 Background subtraction

If $f$ is the fraction of events due to the background material then one can write,

$$L_{\pm\pm} = \sigma_0(1 \pm A_y(P_b + P_t) + P_b P_t A_{yy}) + f\sigma_b(1 \pm P_b a_b) \quad \text{(C.29)}$$

$$R_{\pm\pm} = \sigma_0(1 \mp A_y(P_b + P_t) + P_b P_t A_{yy} + f\sigma_b(1 \mp P_b a_b)) \quad \text{(C.30)}$$

$$L_{\pm\mp} = \sigma_0(1 \pm A_y(P_b - P_t) - P_b P_t A_{yy} + f\sigma_b(1 \pm P_b a_b)) \quad \text{(C.31)}$$

$$R_{\pm\mp} = \sigma_0(1 \mp A_y(P_b - P_t) - P_b P_t A_{yy}) + f\sigma_b(1 \mp P_b a_b) \quad \text{(C.32)}$$

Where $a_b$ is the background analyzing power. Since the background nuclei are not polarized they do not give rise to any spin correlation term. Then for **Method 1 :**

$$S = S_0 \frac{(1 + F_1)}{(1 + F_2)} \quad \text{(C.33)}$$

where

$$F_1 = \frac{f\sigma_b}{\sigma_0(1 + P_b P_t A_{yy})}$$

$$F_2 = \frac{f\sigma_b}{\sigma_0(1 - P_b P_t A_{yy})}$$

With $\frac{f\sigma_b}{\sigma_0} = 0.05$ one gets: $S = 0.976\ S_0$, $\frac{\delta A_{yy}}{A_{yy}} = 2.8\%$. Thus for 5% background subtraction the error in $A_{yy}$ is only 2.8%.

**Method 2 :** Error in $A_{yy}$ is the same as in method 1.

**Method 3 :**

$$r^2 = r_0^2 \left[\frac{1 + \eta_1}{1 + \eta_2}\right]^2$$

where

$$\eta_1 = \left(\frac{f\sigma_b}{\sigma_0}\right) \frac{1 + P_b a_b}{1 + A_y(P_b + P_t) + P_b P_t A_{yy}}$$

$$\eta_2 = \left(\frac{f\sigma_b}{\sigma_0}\right) \frac{1 - P_b a_b}{1 - A_y(P_b + P_t) + P_b P_t A_{yy}}$$

The analyzing power for the background nuclei is not known. If the term containing $a_b$ is neglected then one gets : $\frac{\delta A_{yy}}{A_{yy}} = 7.1\%$. Again this method is less suitable for determining $A_{yy}$ compared to the other two methods.

### C.1.6 Presence of extra vertical component of beam polarization

The neutrons produced in the $LD_2$ target acquire a small ($\simeq 0.1$) component of polarization in the vertical direction. The two dipole magnets, 'CLYDE' and 'BONNIE' precess this spin into the incident neutron beam direction. However, if the magnets are not set properly the precession angle can be different from the ideal value and thus the neutron beam gets an additional vertical component besides the usual vertical component obtained through the spin transfer. Suppose this component of polarization is denoted by 'p'. Then

$$\begin{aligned}
L_{\pm\pm} &= \sigma_0(1 \pm A_y(P_b + P_t) + pA_y + P_bP_tA_{yy} \pm pP_tA_{yy}) \\
R_{\pm\pm} &= \sigma_0(1 \mp A_y(P_b + P_t) - pA_y + P_bP_tA_{yy} \pm pP_tA_{yy}) \\
L_{\pm\mp} &= \sigma_0(1 \pm A_y(P_b - P_t) + pA_y - P_bP_tA_{yy} \mp pP_tA_{yy}) \\
R_{\pm\mp} &= \sigma_0(1 \mp A_y(P_b - P_t) - pA_y - P_bP_tA_{yy}) \mp pP_tA_{yy})
\end{aligned}$$

Thus for **Method 1 :**

$$\begin{aligned}
S^2 &= \frac{(1 + P_bP_tA_{yy} + pA_y)(1 + P_bP_tA_{yy} - pA_y)}{(1 - P_bP_tA_{yy} + pA_y)(1 - P_bP_tA_{yy} - pA_y)} \\
&= S_0^2 \frac{(1 - F_1^2)}{(1 - F_2^2)}
\end{aligned}$$

with

$$F_1 = \frac{pA_y}{1 + P_bP_tA_{yy}}, \quad F_2 = \frac{pA_y}{1 - P_bP_tA_{yy}}$$

The maximum error in the precession angle is $6^0$. Then $p = 0.1 \sin 6^0 = 0.0105$. Substituting various values one gets $S = 1.00006\, S_0$ or $S \simeq S_0$. Thus the error in $A_{yy}$ because of this component of spin is negligible for fixed p.

**Method 2**

$$X^2 = X_0^2 \left( \frac{1 - \xi_1^2}{1 - \xi_2^2} \right)$$

where

$$\begin{aligned} \xi_1 &= \frac{pP_tA_{yy}}{1 + P_bP_tA_{yy} +} \\ \xi_2 &= \frac{pP_tA_{yy}}{1 - P_bP_tA_{yy} +} \end{aligned}$$

Substituting various values one gets $\delta A_{yy} \simeq 0$.

**Method 3 :**

$$r^2 = r_0^2 \left( \frac{1 - \nu_1^2}{1 - \nu_2^2} \right)$$

where

$$\nu_1 = \frac{pA_y + pP_tA_{yy}}{1 + A_y(P_b + P_t) + P_bP_tA_{yy}} \tag{C.34}$$

$$\nu_2 = \frac{pA_y - pP_tA_{yy}}{1 - A_y(P_b + P_t) + P_bP_tA_{yy}} \tag{C.35}$$

Substitution gives : $\delta A_{yy} \simeq 0$.

Now, however, if this component of polarization changes sign with beam spin flip then,

$$\begin{aligned} L_{\pm\pm} &= \sigma_0(1 \pm A_y(P_b + P_t) \pm pA_y + P_bP_tA_{yy} + pP_tA_{yy}) \\ R_{\pm\pm} &= \sigma_0(1 \mp A_y(P_b + P_t) \mp pA_y + P_bP_tA_{yy} + pP_tA_{yy}) \\ L_{\pm\mp} &= \sigma_0(1 \pm A_y(P_b - P_t) \pm pA_y - P_bP_tA_{yy} - pP_tA_{yy}) \\ R_{\pm\mp} &= \sigma_0(1 \mp A_y(P_b - P_t) \mp pA_y - P_bP_tA_{yy}) - pP_tA_{yy}) \end{aligned}$$

**Method 1 :**

$$S = S_0 \left( \frac{F_1}{F_2} \right)$$

with

$$F_1 = 1 + \frac{pP_tA_{yy}}{1 + P_bP_tA_{yy}}$$
$$F_2 = 1 - \frac{pP_tA_{yy}}{1 - P_bP_tA_{yy}}$$

Substitution of various values gives : $S = 0.9964S_0$, $\frac{\delta A_{yy}}{A_{yy}} = 0.4\%$.

**Method 2 :** Error in $A_{yy}$ is the same as in method 1.

**Method 3 :**

$$r = r_0\left(\frac{1+\nu_1}{1-\nu_2}\right)$$

where $\nu_1$ and $\nu_2$ are defined in eqn (3.). Thus $\frac{\delta A_{yy}}{A_{yy}} = 0.6\%$.

### C.1.7 Misalignment of target and beam spins

Suppose the beam and target spins are not exactly vertical but tilted sideways and front-back by a certain angle, $\theta$. Then one can write :

$$\begin{aligned}
L_{\pm\pm} &= \sigma_0(1 \pm A_y(P_b^y + P_t^y) + P_b^yP_t^yA_{yy} + P_b^xP_t^xA_{xx} \\
&\quad + P_b^zP_t^zA_{zz} + (P_b^xP_t^z + P_b^zP_t^x)A_{zx}) \\
R_{\pm\pm} &= \sigma_0(1 \mp A_y(P_b^y + P_t^y) + P_b^yP_t^yA_{yy} + P_b^xP_t^xA_{xx} \\
&\quad + P_b^zP_t^zA_{zz} - (P_b^xP_t^z + P_b^zP_t^x)A_{zx}) \\
L_{\pm\mp} &= \sigma_0(1 \pm A_y(P_b^y - P_t^y) - P_b^yP_t^yA_{yy} - P_b^xP_t^xA_{xx} \\
&\quad - P_b^zP_t^zA_{zz} - (P_b^xP_t^z + P_b^zP_t^x)A_{zx}) \\
R_{\pm\mp} &= \sigma_0(1 \mp A_y(P_b^y - P_t^y) - P_b^yP_t^yA_{yy} - P_b^xP_t^xA_{xx} \\
&\quad - P_b^zP_t^zA_{zz} + (P_b^xP_t^z + P_b^zP_t^x)A_{zx})
\end{aligned}$$

Thus in **Method 1 :**

$$S^2 = S_0^2\,\frac{(1+f_1)(1+f_2)}{(1-f_3)(1-f_4)} \qquad \text{(C.36)}$$

with

$$
\begin{aligned}
f_1 &= \frac{P_b^x P_t^x A_{xx} + P_b^z P_t^z A_{zz} + (P_b^x P_t^z + P_b^z P_t^x) A_{zx}}{1 + P_b^y P_t^y A_{yy}} \\
f_2 &= \frac{P_b^x P_t^x A_{xx} + P_b^z P_t^z A_{zz} - (P_b^x P_t^z + P_b^z P_t^x) A_{zx}}{1 + P_b^y P_t^y A_{yy}} \\
f_3 &= \frac{P_b^x P_t^x A_{xx} + P_b^z P_t^z A_{zz} + (P_b^x P_t^z + P_b^z P_t^x) A_{zx}}{1 - P_b^y P_t^y A_{yy}} \\
f_4 &= \frac{P_b^x P_t^x A_{xx} + P_b^z P_t^z A_{zz} - (P_b^x P_t^z + P_b^z P_t^x) A_{zx}}{1 - P_b^y P_t^y A_{yy}}
\end{aligned}
$$

**Method 2 :**

$$X = X_0 \left( \frac{\eta_1}{\eta_2} \right)$$

where

$$
\begin{aligned}
\eta_1 &= 1 + \frac{P_b^x P_t^x A_{xx} + P_b^z P_t^z A_{zz}}{1 + P_b^y P_t^y A_{yy}} \\
\eta_2 &= 1 - \frac{P_b^x P_t^x A_{xx} + P_b^z P_t^z A_{zz}}{1 - P_b^y P_t^y A_{yy}}
\end{aligned}
$$

**Method 3 :**

$$r^2 = r_0^2 \frac{(1 + \zeta_1)(1 + \zeta_2)}{(1 + \zeta_3)(1 + \zeta_4)}$$

where

$$
\begin{aligned}
\zeta_1 &= \frac{P_b^x P_t^x A_{xx} + P_b^z P_t^z A_{zz} + (P_b^x P_t^z + P_b^z P_t^x) A_{zx}}{1 + A_y (P_b^y + P_t^y) + P_b^y P_t^y A_{yy}} \\
\zeta_2 &= \frac{P_b^x P_t^x A_{xx} + P_b^z P_t^z A_{zz} - (P_b^x P_t^z + P_b^z P_t^x) A_{zx}}{1 + A_y (P_b^y + P_t^y) + P_b^y P_t^y A_{yy}} \\
\zeta_3 &= \frac{P_b^x P_t^x A_{xx} + P_b^z P_t^z A_{zz} + (P_b^x P_t^z + P_b^z P_t^x) A_{zx}}{1 - A_y (P_b^y + P_t^y) + P_b^y P_t^y A_{yy}} \\
\zeta_4 &= \frac{P_b^x P_t^x A_{xx} + P_b^z P_t^z A_{zz} - (P_b^x P_t^z + P_b^z P_t^x) A_{zx}}{1 - A_y (P_b^y + P_t^y) + P_b^y P_t^y A_{yy}}
\end{aligned}
$$

Suppose that the tilt angle $\theta = 10^0$. Thus, $P_b^x = P_b^z = P_b \sin 10^0 = 0.104$, $P_t^x = P_t^z = P_t \sin 10^0 = 0.139$, $A_{xx} = -0.5$, $A_{zz} = 0.8$, $A_{zx} = 0.3$.

Substituting these values one gets for

**Method 1 :** $\frac{\delta A_{yy}}{A_{yy}} = 0.2\%$, **Method 2 :** $\frac{\delta A_{yy}}{A_{yy}} = 1.2\%$., **Method 3 :** $\frac{\delta A_{yy}}{A_{yy}} = 0.6\%$.

Thus the total systematic errors in $A_{yy}$ for different methods are : **Method 1 :** $\delta A_{yy} = 0.015$ or $\frac{\delta A_{yy}}{A_{yy}} = 3.0\%$, **Method 2 :** $\delta A_{yy} = 0.016$ or $\frac{\delta A_{yy}}{A_{yy}} = 3.2\%$., **Method 3 :** $\delta A_{yy} = 0.043$ or $\frac{\delta A_{yy}}{A_{yy}} = 8.6\%$

The cancellation of systematic errors in $A_{yy}$ is the best for method 1 compared to the other two methods.

## C.2 Analyzing power :

Most of the systematic errors appearing in the analyzing power obtained from beam and target polarization are of the same order of magnitude as in the spin correlation parameter. Thus the comparison of two methods of obtaining the analyzing power ($A_y^b$ and $A_y^t$) will only be discussed in terms of the systematic errors arising from different efficiency and residual background in the data because, as is found earlier, these two types of systematic errors have the largest effect on $A_{yy}$. As defined in chapter 5,

$$A_y^b = \frac{1}{P_b}\left(\frac{S_b - 1}{S_b + 1}\right) \tag{C.37}$$

$$S_b^2 = \frac{(L_{++} + L_{+-})(R_{-+} + R_{--})}{(R_{++} + R_{+-})(L_{-+} + L_{--})} \tag{C.38}$$

$$= \frac{(1 + P_b A_y)^2}{(1 - P_b A_y)^2} \tag{C.39}$$

and

$$A_y^t = \frac{1}{P_t}\left(\frac{S_t - 1}{S_t + 1}\right) \tag{C.40}$$

$$S_t^2 = \frac{(L_{++} + L_{-+})(R_{+-} + R_{--})}{(R_{++} + R_{-+})(L_{++} + L_{--})} \tag{C.41}$$

The error in analyzing power is

$$\delta A_y = \frac{2}{P_b}\frac{\delta S}{(S+1)^2} = 0.41\ \delta S$$

.

### C.2.1 Efficiency Change

If the efficiencies change for the left and right detectors then the count rates are given in eqns. 5-8. $S_b^2$ then becomes :

$$\begin{aligned} S_b^2 &\simeq S_{b0}^2\left[1 - \frac{P_t P_b(A_y^2 - A_{yy})}{(1 - P_b^2 P_t^2 A_y^2)}\left(\frac{\epsilon_{R+}}{\epsilon_{R-}} - \frac{\epsilon_{L+}}{\epsilon_{L-}}\right)\right] \\ &= S_{b0}^2\left[1 + 0.1319\left(\frac{1+\delta_1}{1-\delta_1} - \frac{1+\delta_2}{1-\delta_2}\right)\right] \end{aligned}$$

where $\delta_1$, $\delta_2$ are defined earlier in eqns 8-10. The error $\frac{\delta A_y^b}{A_y^b} = 1.0\%$. However, $S_t^2$, on the other hand becomes,

$$\begin{aligned} S_t^2 &= S_{t0}^2\left(\frac{\epsilon_{L-}\epsilon_{R+}}{\epsilon_{L+}\epsilon_{R-}}\right) \\ &= S_{t0}^2\left[\frac{(1-\delta_2)(1+\delta_1)}{(1+\delta_2)(1-\delta_1)}\right] \end{aligned}$$

Substituting one gets $\frac{\delta A_y^b}{A_y^b} = 4.1\%$. Thus the second method of determining the analyzing power from the target polarization is more susceptible to systematic errors arising from the change in efficiency correlated with the target spin. Furthermore, if the solid angle acceptances of left and right detectors change between target up and down runs, either because of wrong positioning of the detectors or some other reasons, it can be shown that the error in $A_y^t$ is considerably larger than that in $A_y^b$.

### C.2.2 Background Subtraction

In presence of background one gets :

$$S_b = S_{b0}\frac{(1+\epsilon_1)}{(1+\epsilon_2)} \tag{C.42}$$

where

$$\begin{aligned}\epsilon_1 &= \frac{\frac{f\sigma_b}{\sigma_0}(1+a_bP_b)}{(1+A_yP_b)}\\ \epsilon_2 &= \frac{\frac{f\sigma_b}{\sigma_0}(1+a_bP_b)}{(1-A_yP_b)}\end{aligned}$$

The background analyzing power is assumed to be equal to 1.0. With $A_y = 0.5, P_b = 0.6$, and 5% background one gets $\frac{\delta A_y^b}{A_y^b} = 2.6\%$.

In case of analyzing power one gets from target polarization,

$$S_t = S_{t0}\frac{(1+\kappa_1)}{(1+\kappa_2)} \tag{C.43}$$

where

$$\begin{aligned}\kappa_1 &= \frac{\frac{f\sigma_b}{\sigma_0}}{(1+A_yP_b)}\\ \kappa_2 &= \frac{\frac{f\sigma_b}{\sigma_0}}{(1-A_yP_b)}\end{aligned}$$

Note that in the above equations the background analyzing power does not appear because the background nuclei are not polarized. The error : $\frac{\delta A_y^b}{A_y^b} = 3.6\%$. This method is more sensitive to the background correction than the one using beam polarization.